

Dissertation zur Erlangung des Doktorgrades
der Fakultät für Chemie und Pharmazie
der Ludwig-Maximilians-Universität München

**Electron microscopy investigations of the coccoliths
of the calcareous algae *Emiliana huxleyi* and
*Calcidiscus leptoporus***

von
Ramona Hoffmann
aus
Halle (Saale)

2014

Erklärung:

Diese Dissertation wurde im Sinne von §7 der Promotionsordnung vom 28. November 2011 von Frau Prof. Dr. Scheu von der Fakultät für Chemie und Pharmazie betreut.

Eidesstattliche Versicherung:

Diese Dissertation wurde eigenständig und ohne unerlaubte Hilfe erarbeitet.

München,

.....
(Unterschrift des Autors)

Dissertation eingereicht am: 13.11.2014

1. Gutachterin: Prof. Dr. Christina Scheu
2. Gutachter: Prof. Dr. Wolfgang W. Schmahl

Mündliche Prüfung am: 17.12.2014

Contents

1	Introduction	1
1.1	Aim	3
1.2	Bibliography	4
2	Theoretical background	9
2.1	Biom mineralization	9
2.2	Mesocrystals	10
2.3	Calcium carbonate	11
2.4	Coccolithophores	13
2.4.1	<i>Emiliana huxleyi</i>	14
2.4.2	<i>Calcidiscus leptoporus</i>	15
2.5	Ocean acidification	16
2.6	Bibliography	17
3	Materials and preparation methods	23
3.1	Iceland spar	23
3.2	Coccolithophores	23
3.2.1	<i>Emiliana huxleyi</i>	23
3.2.2	<i>Calcidiscus leptoporus</i>	25
3.3	TEM Sample preparation methods	26
3.3.1	Sample pretreatment	27
3.3.2	Plan-view sample preparation	28
3.3.3	Cross-section sample preparation	28
3.4	Bibliography	29
4	Characterisation methods	31
4.1	Electron microscopy	31
4.2	Scanning electron microscopy	31
4.3	Focused ion beam microscopy	33
4.4	Transmission electron microscopy	34
4.4.1	Bright field and high resolution imaging	35
4.4.2	Electron diffraction	35
4.4.3	Electron energy low loss spectroscopy	36

4.5	Bibliography	37
5	Experimental details	39
5.1	Instrumentation	39
5.2	Chemicals and substrates	40
6	Nanoprobe crystallographic orientation studies of isolated shield elements of the coccolithophore species <i>Emiliana huxleyi</i>	41
6.1	Introduction	41
6.2	Materials and methods	42
6.2.1	Samples and preparation	42
6.2.2	Instrumentation	43
6.3	Results	43
6.4	Discussion	51
6.5	Conclusion	53
6.6	Bibliography	53
7	TEM preparation methods and their influence on radiation damage on the beam sensitive CaCO₃ shell of <i>Emiliana huxleyi</i>	57
7.1	Introduction	57
7.2	Materials and methods	59
7.2.1	Samples	59
7.2.2	Instrumentation	59
7.3	Results	60
7.3.1	Preparation methods	60
7.3.2	Material transformation	61
7.4	Discussion	68
7.5	Conclusion	70
7.6	Bibliography	71
8	Insight in <i>Emiliana huxleyi</i> coccospheres by focused ion beam sectioning	75
8.1	Introduction	75
8.2	Materials and methods	76
8.2.1	Samples	76
8.2.2	Serial sectioning and imaging	77
8.2.3	Carbon quota and density estimates	77
8.3	Results	78
8.4	Discussion	84
8.5	Conclusion	87
8.6	Bibliography	87

9 Influence of CO₂ on growth and crystallographic assembly of <i>Emiliana huxleyi</i> and <i>Calcidiscus leptoporus</i> coccospheres	93
9.1 Introduction	93
9.2 Materials and methods	94
9.2.1 Samples	94
9.2.2 Instrumentation	95
9.3 Results	95
9.4 Discussion	98
9.5 Conclusion	99
9.6 Bibliography	99
10 Summary	101
11 Curriculum Vitae	103
12 List of scientific contributions	105
12.1 Publications	105
12.2 Oral presentations	106
12.3 Poster presentations	107

List of Figures

2.1	Schematic drawing that illustrates the nonclassical crystallization pathway which forms mesocrystals.	10
2.2	Schematic drawing showing the primitive cell of calcite.	12
2.3	Schematic drawing showing the primitive cell of aragonite.	12
2.4	SEM micrographs showing <i>E. huxleyi</i>	14
2.5	Schematic drawing to illustrate the crystallographic assembly of an <i>E. huxleyi</i> coccolith.	15
2.6	SEM micrographs showing a complete coccosphere and a single coccolith of the coccolithophore species <i>C. leptoporus</i>	15
2.7	Schematic drawing to illustrate the crystallographic assembly of a <i>C. leptoporus</i> coccolith.	16
3.1	Iceland spar crystal that was used to prepare TEM samples.	23
3.2	Comparison between samples with and without dialysis.	27
3.3	Comparison between samples with and without centrifugation.	27
3.4	Four selected steps of the FIB lamellae preparation process of the coccolithophore species <i>E. huxleyi</i>	29
4.1	Interaction between primary electron beam and the bulk material	31
4.2	Schematic drawing indicating the main components of a SEM	32
4.3	Schematic drawing indicating the main components of a FIB microscope	33
4.4	Schematic drawing indicating the main components of a TEM	35
4.5	Schematic drawing of an EEL spectrum	36
6.1	Calcite skeleton of the marine algae <i>E. huxleyi</i>	44
6.2	V/R unit of <i>E. huxleyi</i> coccolith shield elements	45
6.3	Three dimensional structure of <i>E. huxleyi</i> segments	46
6.4	Nano probe diffraction within the distal shield element of <i>E. huxleyi</i>	47
6.5	Nano probe diffraction of the distal- and the proximal shield element of <i>E. huxleyi</i>	48
6.6	Diffraction experiments to determine the angle between different segments of <i>E. huxleyi</i>	49
6.7	High resolution image of <i>E. huxleyi</i>	50
7.1	SEM image of a complete coccosphere of <i>E. huxleyi</i>	60

7.2	TEM investigations of a representative plan-view sample recording the beam sensitivity of the material at an acceleration voltage of 300 kV	63
7.3	The analysis of a cross-section coccolith sample recording the beam sensitivity of the material by TEM	64
7.4	The beam sensitivity of the Iceland spar plan-view sample investigated by TEM at an acceleration voltage of 300 kV	65
7.5	TEM investigations of the Iceland spar cross-section samples done at an acceleration voltage of 300 kV	66
7.6	EELS measurements acquired in diffraction mode of plan-view coccolith samples	67
7.7	EELS measurements taken in diffraction mode on the Iceland spar plan-view samples	67
8.1	SEM-FIB sectioning sequence of the coccolithophore species <i>E. huxleyi</i>	79
8.2	Six exemplary SE images of cross sections through the coccolithophore species <i>E. huxleyi</i>	80
8.3	The correlation between inner and outer coccosphere diameter of <i>E. huxleyi</i> coccolithophores is illustrated in this figure.	82
8.4	In this figure the relationship between coccosphere thickness and the number of coccolith layers is shown.	82
8.5	SEM images of a coccosphere cross-section gained by two different imaging techniques.	83
8.6	The calculated PIC/POC ratio as a function of (a) maximum layer of coccoliths and (b) number of coccoliths is given in this Figure.	85
8.7	The overall cell density and the sinking velocity as function of the PIC/POC ratio is illustrated.	87
9.1	Representative SEM images of the <i>C. leptoporus</i> culture grown at five different CO ₂ levels.	96
9.2	Two different morphologies of <i>C.leptoporus</i> coccoliths occur at a CO ₂ level of 1200 microatm.	97

List of Tables

5.1	Overview of the equipment used during this work.	39
5.2	Overview of the chemicals and substrates used during this work.	40

List of Acronyms and Symbols

Å	Ångstrom
Ar	argon
BF	bright field
bi dH ₂ O	bi-distilled water
BSE	back-scattered electrons
C	carbon
Ca	calcium
CaCO ₃	calcium carbonate
CaO	calcium oxide
CCD	charge-coupled device
<i>C. leptoporus</i>	<i>Calcidiscus leptoporus</i>
CO ₂	carbon dioxide
<i>C. pelagicus</i>	<i>Coccolithus pelagicus</i>
dH ₂ O	distilled water
DMS	dimethyl-sulfide
EBID	electron beam induced deposition
EBS	electron back-scattered diffraction
EDS	energy dispersive x-ray spectroscopy
EEL	electron energy-loss
EELS	electron energy-loss spectroscopy
<i>E. huxleyi</i>	<i>Emiliana huxleyi</i>
ELNES	energy loss near edge structure

List of Acronyms and Symbols

e/nm^2	electrons per square nanometer
eV	electron volt ($1,60 \cdot 10^{-19} \text{ kgm}^2\text{s}^{-2}$)
FIB	focused ion beam
FWHM	full width at half maximum
g	gramm
Ga	gallium
GIS	gas injection system
GPa	Giga Pascal
h	hours
HCl	hydrochloric acid
hkl	Miller indices
H ₂ O	water
HR	high resolution
IBID	ion beam induced deposition
keV	kilo electron volt
kg	kilo gramm
kV	kilo volt
L	liter
LMIS	liquid metal ion source
m	meter
M	mol
MeV	mega electron volt
min	minutes
ml	milliliter
mm	millimeter (10^{-3} m)
μm	micrometer (10^{-6} m)

μmol	micromol
mrاد	millirad
nA	nanoampere
nm	nanometer (10^{-9} m)
nmol	nanomol
rpm	revolutions per minute
O	oxygen
pA	picoampere
pg	picogramm
PETM	Paleocene-Eocene Thermal Maximum
PIC	particulate inorganic carbon
POC	particulate organic carbon
ppm	parts per million
s	seconds
SAED	selected area electron diffraction
SD	standard deviation
SE	secondary electrons
SEM	scanning electron microscopy
Si	silicon
TEM	transmission electron microscopy
V	volume
ZLP	zero loss peak

1 Introduction

Living organisms produce skeletons, teeth and shells, that show extraordinary properties [1, 2, 3, 4] compared to mineralogical formed crystals. The teeth of sea urchins for instance stand out due to their self sharpening mechanism [5], the mother-of-pearl is characterized by an unusual high toughness [6] and it was shown that the spicules of glass sponges have remarkable fibre-optical properties [7]. These examples show the highly advanced material properties of biologically produced hard tissues. Therefore, biomaterials are of high interest in material sciences and become a source of inspiration for material synthesis [8]. The aim is to understand how these inorganic minerals form into precise functional architectures and to use this knowledge for artificial architecture [8]. Tough, durable and adaptive polymer-ceramic can be obtained by an organized assembly of calcium phosphate or calcium carbonate [8]. For the fabrication of magnetic, gravity and storage devices a similar construction is used [9]. If biological archetypes could be used in a synthetic context, inorganic mineral based nano- and microscale material and composite production would be possible [8].

Regardless of whether biological hard tissues are carbonate-, phosphate- or silica-based, the material properties will be achieved by the hierarchical organization of an inorganic and an organic phase [7, 10, 11]. These hybrid composite materials are a mixture of biopolymer and mineral components, which are nano-, micro- and macro-structurally combined [4, 12, 13]. Besides the extraordinary material properties these materials show an enormous biodiversity. Their structures are perfectly adapted to the function within the organism and/ or the requirements of the habitat. Therefore, the hard tissues are of high interest for paleoclimatic research. Since these materials are much more stable than soft tissues, they are used for biostratigraphic dating as well [14].

One of the most common mineral compounds on earth, that is formed by classical crystallization and as well by organisms, is calcium carbonate (CaCO_3). This chemical compound mainly occurs in the modifications calcite and aragonite but also as vaterite, that is basically build as small crystals from supersaturated solutions. Calcite and aragonite are the principle rock forming minerals of several sedimentary rocks like limestone and chalk [15]. In addition these minerals can be produced by terrestrial species like snails and by marine organisms like foraminifera. Since it is possible to gain information on the genetic specificity of different species, e.g. to determine the composition of the organic matrix templates or any protein components associated with the biomineral, carbonate biominerals are the target of many research groups [16, 17]. Besides this biological questions the analysis of the biomineral for trace, minor and major element composition, the evaluation of carbon and oxygen isotopic signatures and the

combination of these data with global geological and geographical information is a valuable help for the investigation of earth science problems [18, 19, 4, 20, 21].

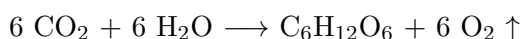
Coccolithophores are the most famous and magnificent example of unicellular marine organism groups that build an exoskeleton of CaCO_3 [19]. These small marine alga first occurred during the Triassic around 250 million years ago. In earth history they formed big rock massives like the White Cliffs of Dover [14]. Recent coccolithophore species are the most important ingredient of the calcareous deep sea sediments [22]. Their skeletons show the typical hierarchical architecture of biologically formed materials. They build a micrometer sized sphere, that shelters the living cell inside. This coccosphere is composed of small CaCO_3 platelets, the coccoliths, which possess extraordinary structures. These elements consist of two even smaller crystal units, the R- and V- units, which alternate in their crystallographic c-axis orientation [23]. While the c-axis of the R-units are oriented parallel to the coccolith plane, the V-units c-axis are perpendicular to the coccolith plane oriented [23]. So far, it is assumed that each of these units behave as a single calcite crystal [24]. This differs from other marine calcifiers like molluscs that seemed to be single-crystalline, but were found to consist of small crystals with almost the same orientation, the so called mesocrystals [25]. Therefore a detailed investigation of the coccolith crystal structure is a fascinating challenge.

Coccolithophores influence the global carbon cycle of the oceans since the calcification, the process that produces the coccoliths and the photosynthesis are symbiotic processes [26]. The carbon dioxide (CO_2), that is produced during the calcification can be used as educt for the photosynthesis [26]:

calcification:



photosynthesis:



It is important to mention that the global oceans absorb a significant amount of the atmospheric CO_2 including one-third of the anthropogenic CO_2 [27]. For the last two centuries human activities like the use of fossil fuel and deforestation have increased the atmospheric CO_2 concentration by approximately 31 % [28, 29]. This trend is predicted to continue, and CO_2 levels might exceed 800 ppm by the end of the century [30]. The increase in atmospheric CO_2 concentration due to the anthropogenic emissions might cause a change in the global climate. The CO_2 absorption of the ocean has its consequences as it lowers the pH value of the ocean water body and leads to alterations in fundamental chemical balances, known as ocean acidification [31]. The influence of the ocean acidification on marine organisms with a CaCO_3 shell, like coccospheres, is important to study [31]. In laboratory experiments it was shown that calcifying species reduce calcification and growth rates under high- CO_2 conditions [31] but the potential of marine organisms to adapt to the increasing CO_2 level is not well known todate [31, 32]. Since

coccolithophores have great potential e.g. for CO₂ fixation, it is important to investigate their behavior under high-CO₂ conditions in the laboratory.

There are two species that allow laboratory experiments concerning the CO₂ level, *Emiliania huxleyi* (*E. huxleyi*) and *Calcidiscus leptoporus* (*C. leptoporus*). Both species are cosmopolitan and can be found in the world wide oceans [26]. They tolerate large temperature ranges and *E. huxleyi* is in the group of coccosphere species that tolerate the highest temperature ranges (between 1 °C and 30 °C) [26]. This species can also live with different light rates, it can grow in eutrophic as well as in oligotrophic water masses and in different water depths [26]. Therefore, it is very well suited for laboratory experiments. Both species are relatively large and the coccospheres of *C. leptoporus* belong, with an average size of 17 μm, to the biggest coccolithophore species [26].

1.1 Aim

The first goal of this thesis was the determination of the precise and reliable hierarchical structure of coccoliths at the nanoscale using electron microscopy and electron diffraction techniques. Pioneer work in this field done by many different groups proposed that the small crystal units that build up the coccoliths consist of single-crystalline calcite [33, 34, 23, 35]. The abundant coccolithophore species *E. huxleyi* was chosen for this part of the thesis because it is the most common and best investigated species. One aim was to study the crystallographic orientation of the *c*-axis of the R- and V- unit. The latter is challenging since in fully grown *E. huxleyi* coccoliths the R- and V-unit possess sizes under 100 nm and the V-unit is overgrown by the R-unit [23]. So far the description of the crystallographic orientation of the V-unit of *E. huxleyi* was only based on analogy to other coccoliths. An other aim was to determine whether the individual coccoliths are mesocrystalline or single-crystalline, since many marine calcifiers show single-crystalline behavior, but consist of many nano crystals with almost the same orientation instead.

The obstacle in this attempt is the artifact free target preparation of the coccoliths and their elements. Therefore, the second goal of this thesis was the development and optimization of preparation techniques for coccolith plan-view and cross-section samples. In addition, optimal parameters for the transmission electron microscopy (TEM) measurements needed to be found. Here *E. huxleyi* coccoliths were used and the results compared to those of Iceland spar (single-crystalline calcite crystals) samples.

The third goal of this thesis was the determination of the reaction of this micro organisms to environmental conditions with respect to ocean acidification. The main aim was to investigate the influence of a rising CO₂ concentration on the morphology and crystal structure of the coccolith R- and V- units. Therefore, laboratory experiments were performed. Here two different coccolith species, *E. huxleyi* grown in three different CO₂ levels and *C. leptoporus* grown in five different CO₂ levels, were used. To discover changes in the morphology of the calcite crystals scanning electron microscopy (SEM) imaging was used.

In this regard this thesis provides an important contribution in the following research fields:

1. Mineralization of biocarbonates, with the main focus on calcite.
2. Crystallographic assembly of calcite shells of marine organisms, especially of coccolithophores.
3. Preparation and parameters for high resolution electron microscopy methods for beam sensitive biological materials.
4. Influence of environmental parameters such as temperature, pH-value or salinity on marine biocarbonates.
5. Knowledge concerning the role of the coccolithophore species *E. huxleyi* and *C. leptoporus* with respect to the global carbon cycle.

1.2 Bibliography

- [1] MAYER, G., AND SARIKAYA, M. Rigid biological composite materials: Structural examples for biomimetic design. *Experimental Mechanics* **42**, 4 (2002), 395–403.
- [2] AIZENBERG, J., WEAVER, J. C., THANAWALA, M. S., SUNDAR, V. C., MORSE, D. E., AND FRATZL, P. Skeleton of *Euplectella sp.*: structural hierarchy from the nanoscale to the macroscale. *Science* **309** (2005), 275–278.
- [3] MAYER, G. Rigid biological systems as models for synthetic composites. *Science* **310** (2005), 1144–1147.
- [4] SCHMAHL, W. W., GRIESSHABER, E., MERKEL, C., KELM, K., DEUSCHLE, J., NEUSER, R. D., GÖTZ, A. J., SEHRBROCK, A., AND MADER, W. Hierarchical fibre composite structure and micromechanical properties of phosphatic and calcitic brachiopod shell biomaterials An overview. *Mineralogical Magazine* **72**, 2 (2008), 541–562.
- [5] KILLIAN, C. E., METZLER, R. A., GONG, Y., CHURCHILL, T. H., OLSON, I. C., TRUBETSKOY, V., CHRISTENSEN, M. B., FOURNELLE, J. H., DE CARLO, F., COHEN, S., MAHAMID, J., SCHOLL, A., YOUNG, A., DORAN, A., WILT, F. H., COPPERSMITH, S. N., AND GILBERT, P. U. P. A. Self-sharpening mechanism of the sea urchin tooth. *Advanced Functional Materials* **21** (2011), 682–690.
- [6] CURREY, J. D. Mechanical properties of mother of pearl in tension. *The Royal Society of London Series B, Biological Sciences* **196**, 1125 (1977), 443–463.
- [7] AIZENBERG, J., MULLER, D. A., GRAZUL, J. L., AND HAMANN, D. R. Direct fabrication of large micropatterned single crystals. *Science* **299** (2003), 1205–1208.

-
- [8] MANN, S. Molecular tectonics in biomineralization and biomimetic materials chemistry. *Nature* **365** (1993), 499–505.
- [9] MANN, S. Biomineralization: the hard part of bioinorganic chemistry! *Journal of the Chemical Society, Dalton Transactions* **1** (1993), 1–9.
- [10] GILBERT, P., ALBRECHT, M., AND FRAZER, B. The organic mineral interface in biominerals. *Reviews in Mineralogy and Geochemistry* **59** (2005), 157–185.
- [11] GAO, H. Application of fracture mechanics concepts to hierarchical biomechanics of bone and bone-like materials. *International Journal of Fractures* **18** (2006), 101–137.
- [12] SCHMAHL, W., KELM, K., GRIESSHABER, E., GOETZ, A., JORDAN, G., XU, D., MERKEL, C., BRAND, U., AND LOGAN, A. The hierarchical organization in biomaterials: from nanoparticles via mesocrystals to functionality. *Seminario Society Espaniol Mineralogical* **7** (2010), 5–21.
- [13] DUNLOP, J., AND FRATZL, P. Biological composites. *Annual Review of Materials Research* **40** (2010), 1–24.
- [14] STANLEY, S. M. *Earth system history*. W.H. Freeman and Company, New York, 1999.
- [15] JONES, A. *Collins Wild guide. Rocks & minerals*. HaperCollinsPublisher, London, 2000.
- [16] GROSSMAN, E. L. Stable isotopes in modern benthic foraminifera: a study of vital effect. *Journal of Foraminiferal Research* **17**, 1 (1987), 48–61.
- [17] GAST, R. J., AND CARON, D. A. Molecular phylogeny of symbiotic dinoflagellates from planktonic foraminifera and radiolaria. *Molecular Biology and Evolution* **13**, 9 (1996), 1192–1197.
- [18] ADDADI, L., MORADIAN, J., SHAY, E., MAROUDAS, N. G., AND WEINER, S. A chemical model for the cooperation of sulfates and carboxylates in calcite crystal nucleation: Relevance to biomineralization. *Proceedings of the National Academy of Sciences of the United States of America* **84**, 9 (1987), 2732–2736.
- [19] SKINNER, H. C. W. Biominerals. *Mineralogical Magazine* **69**, 5 (2005), 621–641.
- [20] MERKEL, C., DEUSCHLE, J., GRIESSHABER, E., ENDERS, S., STEINHAUSER, E., HOCHLEITNER, R., BRAND, U., AND SCHMAHL, W. W. Mechanical properties of modern calcite- (*Mergerlia truncata*) and phosphate-shelled brachiopods (*Discradisca stella* and *Lingula anatina*) determined by nanoindentation. *Journal of Structural Biology* **168**, 3 (2009), 396–408.
- [21] SETO, J., MA, Y., DAVIS, S. A., MELDRUM, F., GOURRIER, A., KIM, Y.-Y., SCHILDE, U., SZTUCKI, M., BRUGHAMMER, M., MALTSEV, S., JÄGER, C., AND CÖLFEN, M.

- Structure-property relationships of a biological mesocrystal in the adult sea urchin spine. *Proceedings of the National Academy of Sciences* **109**, 18 (2012), 7126–7126.
- [22] RILEY, J., CHESTER, J. P., AND CHESTER, R., Eds. *Treatise on chemical oceanography*. Academic Press, London, 1976.
- [23] YOUNG, J. R., DIDYMUS, J. M., BOWN, P. R., PRINS, B., AND MANN, S. Crystal assembly and phylogenetic evolution in heterococcoliths. *Nature* **356** (1992), 516–518.
- [24] WILBUR, K. M., AND WATABE, N. Experimental studies on calcification in molluscs and the alga *Cocolithus huxleyi*. *Annals of the New York Academy of Sciences* **109** (1963), 82–112.
- [25] SONG, R.-Q., AND CÖLFEN, H. Mesocrystals–ordered nanoparticle superstructures. *Advanced Materials* **21** (2010), 1–30.
- [26] WINTER, A., AND SIESSER, G. W., Eds. *Coccolithophores*. University Press, Cambridge, 1994.
- [27] SABINE, C. L., AND FEELY, R. A. The oceanic sink for carbon dioxide. In *Greenhouse Gas Sinks*, D. Reay, N. Hewitt, J. Grace, and K. Smith, Eds. CABI Publishing, Oxfordshire, UK, 2007, pp. 31–49.
- [28] SOLOMON, S., QIN, D., MANNING, M., CHEN, Z., MARQUIS, M., AVERYT, K. B., TIGNOR, M., AND MILLER, H. L., Eds. *Climate change 2007: The physical science basis: Contribution of working group I to the fourth assessment report of the intergovernmental panel on climate change*. Cambridge University Press, Cambridge, United Kingdom and New York, 2007.
- [29] LÜTHI, D., LE FLOCH, M., BEREITER, B., BLUNIER, T., J.-M., B., SIEGENTHALER, U., RAYNAUD, D., JOUZEL, J., FISCHER, H., KAWAMURA, K., AND STOCKER, T. High-resolution carbon dioxide concentration record 650,000–800,000 years before present. *Nature* **453** (2008), 379–382.
- [30] RAUPACH, M. R., MARLAND, G., CIAIS, P., LE QUÉRÉ, C., CANADELL, J. G., KLEPPER, G., AND FIELD, C. B. Global and regional drivers of accelerating CO₂ emissions. *Proceedings of the National Academy of Sciences of the United States of America* **104**, 24 (2007), 10288–10293.
- [31] DONEY, S. C., FABRY, V. J., FEELY, R. A., AND KLEYPAS, J. A. Ocean acidification: the other CO₂ problem. *Annual Review of Marine Science* **1** (2009), 169–192.
- [32] BOYD, P. W., DONEY, S. C., STRZEPEK, R., DUSENBERRY, J., LINDSAY, K., AND FUNG, I. Climate-mediated changes to mixed-layer properties in the Southern Ocean: assessing the phytoplankton response. *Biogeosciences* **5** (2008), 847–864.

- [33] WATABE, N. Crystallographic analysis of the coccolith of *Coccolithus huxleyi*. *Calcified Tissue Research* **1** (1967), 114–21.
- [34] MANN, S., AND SPARKS, N. H. C. Single crystalline nature of coccolith elements of the marine alga *Emiliana huxleyi* as determined by electron diffraction and high-resolution Transmission. *Proceedings of the Royal Society B: Biological Sciences* **234** (1988), 441–453.
- [35] SARUWATARI, K., OZAKI, N., NAGASAWA, H., AND KOGURE, T. Comparison of crystallographic orientations between living (*Emiliana huxleyi* and *Gephyrocapsa oceanica*) and fossil (*Watznaueria barnesiae*) coccoliths using electron microscopes. *American Mineralogist* **93** (2008), 1670–1677.

2 Theoretical background

2.1 Biomineralization

The ability of organisms to form mineralized hard tissues started million of years ago during the Proterozoic when first prokaryotes and then eukaryotes developed this mechanism [1]. During the beginning of the Cambrian around 540 million years ago organisms from many different phyla evolved the ability to form minerals. Most of these first mineralized tissues were in composition comparable to the 64 different minerals known by now [2].

The term biomineralization summarizes all processes by which organisms form minerals [1] and has its roots in the late 17th century with the advent of the light microscope [3]. The study of mineralized tissues began with the investigations of van Leeuwenhoek, who identified the osteons common in many bones using a magnification of about 400 times [4] and Havers, who found lamellae, that have a size of about 3 μm [5]. In 1924 a first book on biomineralization was published [6]. Since that time biomineralization studies have become more and more interesting for scientists. This research field combines biological, chemical, and earth sciences disciplines [1]. With the advances in the development of suitable tools for structural studies, which were in the beginning optical microscopy, then polarized light microscopy and X-ray diffraction and nowadays SEM and TEM, the understanding of biomineralization processes has made much progress [3].

The term biomineral refers not only to a mineral produced by organisms, it also describes that almost all of these materials are composites, combining a mineral and an organic compound [1]. Since these materials form under controlled conditions, they often reveal properties such as shape, size, crystallinity, isotopic and trace element compositions that are different from the properties of the inorganically formed counterparts [3]. All this complexity is represented by the terms biomineral and biomineralization [3].

The classification of biominerals is based on composition of the inorganic constituents and there can be found representatives in many of the 78 mineral classes [7]. The greatest number of biominerals can be allocated to the classes of sulfides, sulfates, carbonates and phosphates [7]. Carbonate biomineralized forms like molluscs, clams, oysters, gastropods, or corals are present in the earth crust due to their appearance in limestones or marble deposits. The listed organisms are multi-cellular with several organs that can employ separate mechanism for the carbonate deposition [8]. In multi-cellular organisms biomineralized tissues are adapted for specific functions [7]. Echinoids for example use their spines for protection and although these spines can break they are able to regenerate them by using the same biomineral, calcite while

maintaining the original pattern of the macro-structure [9].

Biom mineralization as research field is interested in understanding the ultrastructure and the mineral phase, the macromolecules that make up the framework in which the minerals form and the interphase that links the two [7].

2.2 Mesocrystals

During the last years the alignment of nanoparticle building blocks into ordered superstructures, the so called mesocrystals, gain more and more attention of chemists, material scientists and physicists [10, 11]. Due to the mesoscopic structure of these materials new opportunities for material design are provided [11]. In this research field much can be learned from biomineralization, which produces organic-inorganic hybrid materials with outstanding properties, complex morphologies and a hierarchical order [1].

The term mesocrystal is used for ordered superstructures of co-oriented crystallites in the mesoscopic size range (1-1000 nm) [11]. They are often in almost perfect three dimensional mutual order and show the same scattering pattern and behavior in polarized light like single-crystals [11].

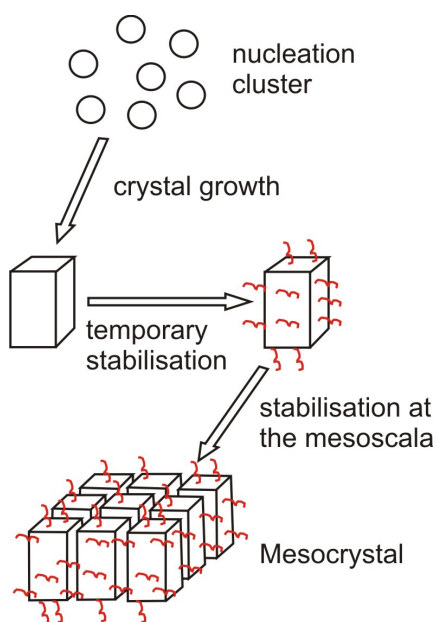


Figure 2.1 Schematic drawing that illustrates the nonclassical crystallization pathway to form mesocrystals. Drawing modified from [12]. Primary nanoparticles get covered by a biopolymer or other additives, that stabilizes them at the mesoscale [12]. The resulting mesocrystals look like a brick wall.

The formation of a single-crystal is described by the classical crystallization model. Here crystal growth is characterized as an amplification process, where stable nuclei are enlarged by unit cell replication [13]. For the formation of mesocrystals several mechanisms can be

employed, as described in [11]. The first possibility to form a mesocrystal is aligning nanoparticles using an oriented organic matrix as illustrated in figure 2.1. An alternative way is the alignment of the nanoparticles by magnetic or electric fields or mutual alignment of identical crystal faces. A third method is employing a mineral bridge to connect two nanoparticles during epitaxial growth. Nanoparticle alignment can be also achieved by spatial constraints. During the growth of anisotropic nanoparticles in a constrained environment, the particles can be connected by outgrowth under consideration of the space limitation. These mechanisms can also occur simultaneously [11]. It is also worth to mention that mesocrystals can form pure inorganic nanoparticles [12]. Amorphous particles can be formed, that may transform before or after their assembly to complicated morphologies into crystalline ones [12].

The term mesocrystal has been used in literature to describe mutual three-dimensional translational order of various nanocrystals [10]. The porous internal structure of BaSO_4 was one of the first systems to be reported as mesocrystalline [14]. A further indication of mesocrystals was found in 1988 during a synthetic study on various Ce^{IV} compounds in absence of organic additives [15]. Due to the improved analytical methods and the establishment of mesocrystal and mesoscale organization concepts an increasing number of mesocrystal systems have been reported recently [10, 16].

2.3 Calcium carbonate

Calcium carbonate is one of the most common compounds found in sedimentary rocks. These include limestones and chalk, which build up whole mountains like the alps [17]. In history they were used as building material and many famous historical monuments like the Cheops pyramids are built from limestone [18]. But calcium carbonate can also be found in metamorphic rocks like marble, which is used for several famous artworks [18]. This chemical compound occurs in three mineral modifications: calcite, aragonite and the less common vaterite.

Calcite is a colorless mineral that can be found in igneous, sedimentary and as well metamorphic rocks [19]. This mineral crystallizes trigonal in the space group $R\bar{3}c$ (space group number: 167) with the lattice parameters $a, b = 4.99 \text{ \AA}$ and $c = 17.06 \text{ \AA}$; $\alpha, \beta = 90^\circ$ and $\gamma = 120^\circ$ [20] (Fig. 2.2). It builds prismatic crystals of several varieties, that are commonly twinned, but also occur nodular, granular, stalatitic compact and earthy [19]. Calcite can be formed organically or inorganically and may contain a variety of impurities including iron, magnesium, manganese, lead and strontium [19]. Particularly well formed crystal varieties of calcite are the so called Dog tooth spar and Iceland spar [19].

Aragonite is the white yellowish or grey high-pressure form (polymorph) of calcite that is found in sedimentary and hydrothermal depositions [19]. It can occur with sedimentary gypsum deposits and can be formed by biomineralization as well [19]. Aragonite crystallizes orthorhombic in the space group $Pmcn$ (space group number: 62) with the lattice parameters $a = 4.96 \text{ \AA}$; $b = 7.97 \text{ \AA}$; $c = 5.74 \text{ \AA}$ and $\alpha, \beta, \gamma = 90^\circ$ [20] (Fig. 2.3). This mineral occurs as sharp pointed prismatic crystals that are often twinned but have a different shape compared to calcite [19].

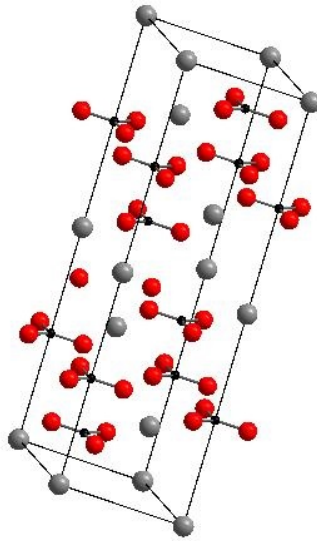


Figure 2.2 Schematic drawing showing the primitive cell of calcite. This figure was constructed with the program Diamond. Ca^{+2} is represented by the grey, C^{+4} by the black and O^{-2} by the red balls.

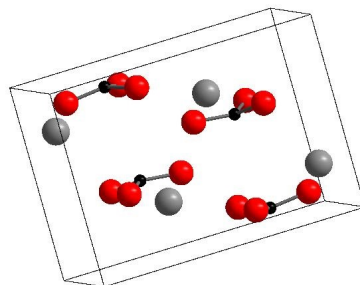


Figure 2.3 Schematic drawing showing the primitive cell of aragonite. This figure was constructed with the program Diamond. Ca^{+2} is represented by the grey, C^{+4} by the black and O^{-2} by the red balls.

Aragonite crystals can also occur as radiating acicular needles, corals, stalactites and encrusting forms [19].

The structure of the rare hexagonal modification vaterite, that is grown as small crystals from supersaturated solutions, is not fully clarified [21]. Referring to Wang and Becker 2009 this mineral crystallizes in the space group $P6_522$ (space group number: 179) with the lattice parameters $a = 7.290 \text{ \AA}$; $b = 7.290 \text{ \AA}$; $c = 25.302 \text{ \AA}$; $\alpha, \beta = 90^\circ$ and $\gamma = 120^\circ$ [22].

2.4 Coccolithophores

Not only humans use calcium carbonate to build houses, also many creatures use this material to make nails, spines, bones or skeletons in order to protect themselves or for adaption to the living environment [23]. Since calcium is not very well soluble in freshwater, the oceans, which absorb much higher calcium rates are a great environment for calcifiers [18]. Therefore many marine microorganisms like algae, mollusks, corals or plankton are specialized to use the calcium and the carbon content of the seawater to produce soft tissues [18]. One marine organism group that builds its shells of calcium carbonate are the coccolithophores.

Coccolithophores are marine living algae, which belong to the division Haptophyta. The surface of these single cell organisms is covered by small calcium carbonate platelets, which are called coccoliths [24]. Coccolithophores utilize photosynthesis and therefore live in the light-flooded surface region between 0 and 200 m water depth, called euphotic zone [25]. Their distribution in the oceans is affected by the latitude, the ocean current and the characteristics of the water masses like the amount of nutrients, the salinity, the temperature (usually between 12 and 27 °C) and the amount of trace elements and vitamins [26]. They have a high significance for the carbon cycle in the global oceans. On one hand on the organic carbon pump through the photosynthesis and the emission of dimethyl-sulfide (DMS) [27] and on the other hand on the inorganic carbon pump through the coccolith formation [28]. Modern coccoliths produce the main part of the calcareous deep sea sediments [29] and since 230 million years they are the main component of the fine grained pelagic deep sea sediments [30].

Today there live about 280 different coccolithophore species [31], which are characterized by the form of the coccosphere, the morphology of the flagellate, the form of the coccoliths and the coccosphere assembly [32]. These structures can only be realized by directly controlled biomineralization [31]. For that the protoplasm of the single cell contains besides the chloroplasts, which are important for the photosynthesis, also the typical cell organelles specific vesicles where the coccoliths are formed [33]. The mineralization starts by the transportation of calcium and carbonate ions into the vesicles, where a preformed organic base plate is formed [34]. Since the nucleation takes place on the distal rim of the base plate the ions are delivered specifically there [34]. A complete closed ring of small crystallites develops during the calcite nucleation about the rim [34]. These so called proto coccolith ring consist of small crystals with an alternating orientation of the crystallographic c-axis [34]. The crystallographic c-axis of the R-unit crystals is pointing parallel to the coccolith plane, while the c-axis of the V-unit crystals is perpendicular to the coccolith plane oriented [35]. The grown coccoliths are transported from the inner cell to the cell surface by the vesicles [33], where they build up the shell.

The function of the coccosphere is still discussed. Some species like *Rhabdosphaera clavigera* seem to enlarge their outer diameter by needle like coccoliths. That might be a protection against filter feeders, which select their food by the size [26]. For other species like *Umbellosphaera tenuis* the coccosphere serves as a buffer zone between the sensitive cell and the environment [26]. An other hypothesis is that the size and morphology of the coccosphere is part of the locomotion of

the coccolithophores that have no flagella [26].

2.4.1 *Emiliana huxleyi*

The coccolithophore *E. huxleyi* is the most common species within the around 200 recent species [24]. The surface of the coccosphere is covered by overlapping coccoliths (Fig. 2.4a). The cells of *E. huxleyi* coccolithophores are relative small compared to their large coccoliths [26]. Therefore they produce only one coccolith at a time and new coccoliths will not be produced until the mature coccolith is released [26]. The coccolith production in *E. huxleyi* is a light dependent process and in actively growing cultures one coccolith is growing every two hours [36]. The coccoliths of this species belong to the group of placoliths and have an average diameter of around $2.5 \mu\text{m}$ and a weight of approximately $1.8 \cdot 10^{-12} \text{ g}$ [37]. The shape of the coccoliths can be compared to that of a cable reel consisting of a central tube that connects the lower proximal shield and the upper distal shield and encloses the central area (Fig. 2.4b) [33]. With this morphology the coccoliths can interlock closely on the coccosphere and therefore form a robust structure [33].

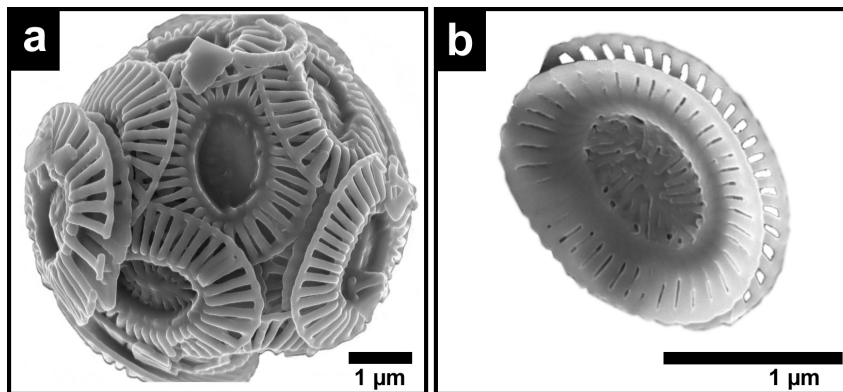


Figure 2.4 SEM micrographs showing a complete coccosphere and a single coccolith of the coccolithophore species *E. huxleyi*.

- a) A complete coccosphere is shown.
- b) A single coccolith is given.

The model of Young *et al.* [35] assumes that the coccoliths of this species consist of two crystal units with differently oriented crystallographic c-axis. The radial R-unit is built up of crystals with the c-axis oriented parallel to the coccolith plane and the c-axis of the vertical V-unit is pointing perpendicular to the coccolith plane (Fig. 2.5) [35]. In the case of *E. huxleyi* the biomineralization starts with the formation of a proto coccolith ring with alternating sequences of R- and V-units [35]. The species specific morphology forms during crystal growth, where the V-unit crystals will be overgrown by the crystals of the R-unit (Fig. 2.5) [35].

Besides the common coccolith bearing cells, the so called C-cells, other cell types can be found in *E. huxleyi* culture samples, like naked cells called N-cells, flagellate cells with organic body scales but without coccoliths called S-cells and amoeboid cells, which are rare [26]. All these

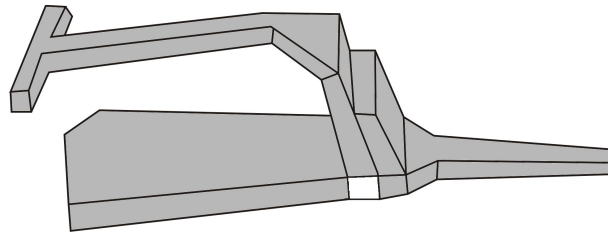


Figure 2.5 Schematic drawing to illustrate the crystallographic assembly of an *E. huxleyi* coccolith. The area given in light grey is the R-unit with the c-axis parallel to the coccolith plane and the smaller white area corresponds to the overgrown V-unit, where the c-axis is oriented perpendicular to the coccolith plane. This figure was modified from [38].

cell types represent different life cycle stages of *E. huxleyi* [39]. For this species it was shown that the life cycle is always an alternation between a non-motile stage and one or more motile stages [40].

2.4.2 *Calcidiscus leptoporus*

With an average coccosphere size of around $17\ \mu\text{m}$ *C. leptoporus* belongs to the biggest coccosphere species (Fig. 2.6a). The cell is surrounded by around 15 - 30 coccolith plates [41]. Based on the morphology of the coccoliths this species belongs as well as *E. huxleyi* to the placoliths [41]. The coccoliths have an average size of $5\text{-}8\ \mu\text{m}$ and consist of flat, overlapping elements with curved radial edges (Fig. 2.6b) [33].

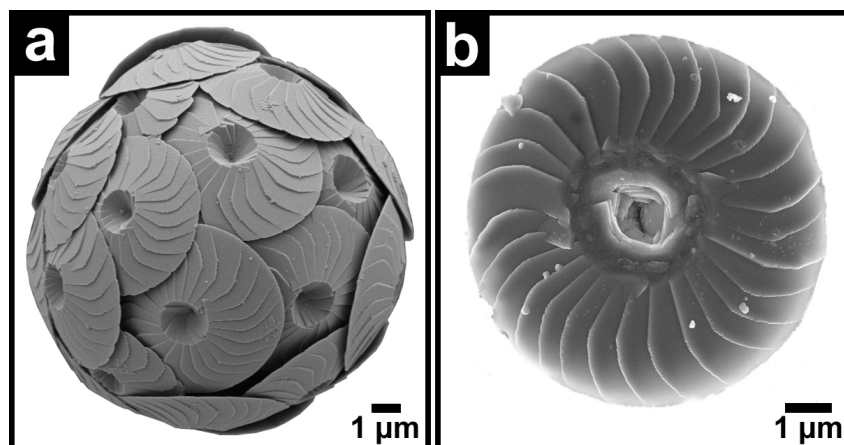


Figure 2.6 SEM micrographs showing a complete coccosphere and a single coccolith of the coccolithophore species *C. leptoporus*.

- a) SEM image showing a complete coccosphere of *C. leptoporus* (courtesy of Gerald Langer).
- b) A single coccolith of this species is given in this SEM image.

The V-unit of this species builds the distal shield and the tube element, and is extended to the proximal surface, whereas the R-unit forms the proximal shield element (Fig. 2.7) [41].

The proto coccolith ring of *C. leptoporus* becomes embedded within the structure of the grown coccolith [41]. The ring is only visible if the proximal shield element has broken off, which is happening frequently since the connection between the proximal and the distal shield element is weak (Fig. 2.7) [41].

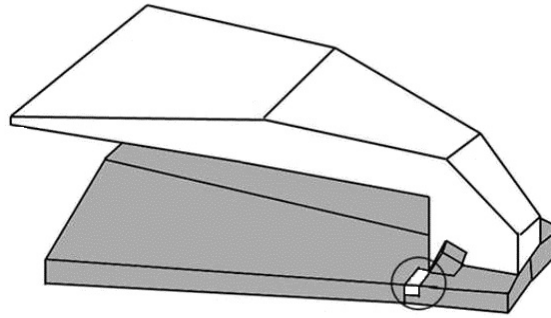


Figure 2.7 Schematic drawing to illustrate the crystallographic assembly of a *C. leptoporus* coccolith. The area given in light grey is the R-unit, where the c-axis is oriented parallel to the coccolith plane and the white area corresponds to the V-unit, with the c-axis pointing perpendicular to the coccolith plane. The encircled area mark the position of the proto coccolith ring. This figure was modified from [35].

Within the life cycle of *C. leptoporus* two biomineralization phases occur [33]. A diploid phase, that is characterized by heterococcoliths that show a radial symmetry and are formed of a limited number of calcite crystals with complex, strongly modified shapes [33]. This live stage form is termed as *C. leptoporus*. In contrast there is also a haploid phase in *C. leptoporus*, that is characterized by holococcoliths, which are formed of numerous tiny (around $0.1 \mu\text{m}$) calcite crystallites [33]. This life form was first described and named as separate species and is therefore called *Syracolithus quadriperforatus*[42].

2.5 Ocean acidification

Within the last 150 years the average global temperature has increased from $13.7 \text{ }^\circ\text{C}$ in 1850 to $14.5 \text{ }^\circ\text{C}$ in the year 2000 and this trend is predicted to continue until in 2100 the average temperature will increase further by about 1.1 to $6.4 \text{ }^\circ\text{C}$ [43]. This phenomena is caused by the increased atmospheric CO_2 concentration, which is mainly produced by the human activities within the last two centuries like the use of fossil fuel and the deforestation [43, 44]. This so called global warming has large-scale consequences such as rising sea-levels, melting glaciers, drifting vegetation zones and hence the destruction of living environments [43]. In comparison with the terrestrial vegetation that is not able to bind the rising CO_2 , the rising CO_2 level is slowed down by the global oceans, which absorb a significant amount of the CO_2 including one-third of the anthropogenic CO_2 [45].

Besides the CO_2 concentration density differences of the ocean water, which are the main pa-

parameter that defines ocean stratification, water masses and deep water thermohaline circulation are interesting for climate studies [46]. The density differences are caused by oscillations in salinity and temperature of the water, which also have a main influence on the climate system [46]. Therefore the detailed knowledge of the ocean salinity and temperature is of high significance to understand mechanisms that affect the climate system [46]. The morphological variability of marine organisms have great potential for these studies [47, 48, 49].

The calcium carbonate production of marine organisms is an important factor in the global carbon circle. Feely *et al.* [50] for example calculated a yearly calcium carbonate sequestration by marine sediments of 0.23-0.31 petagramms carbon. Since the main part of the calcium carbonate produced by marine organisms will dissolve during the sinking process and at water depths below the carbonate compensations depth, this value corresponds to only around 30 % of the biologically formed calcium carbonate [50].

But the absorption of the rising CO₂ by the oceans has its consequences, it causes a decrease in ocean pH, an effect referred to as ocean acidification. The consequence of the ocean acidification is a change in the ocean carbonate system and thus in the distribution pattern and diversity of carbonate shelled organisms that at present occur in the oceans [45]. Marine organisms with CaCO₃ shells like corals, mollusks, echinoderms and foraminifera will be directly influenced by ocean acidification [51]. The potential of these marine organisms to adapt to the increasing CO₂ level under natural long term conditions is not well known yet [52, 51]. Therefore laboratory experiments under defined CO₂ concentrations can help to gain knowledge about the adaptability of marine calcifiers.

2.6 Bibliography

- [1] WEINER, S., AND DOVE, P. M. An Overview of Biomineralization Processes and the Problem of the Vital Effect. *Reviews in Mineralogy and Geochemistry* **54** (2003), 1–29.
- [2] KNOLL, A. Biomineralization and evolutionary history. *Reviews in Mineralogy and Geochemistry* **54**, 1 (2003), 329–356.
- [3] WEINER, S. Biomineralization: a structural perspective. *Journal of Structural Biology* **163** (2008), 229–34.
- [4] VAN LEEUWENHOEK, A. *An extract of a letter from Mr. Anth. Van. Leeuwenhoek, containing several observations on the texture of the bones of animals compared with that of wood: on the bark of trees: on the little scales found on the cuticula, etc.* J. R. Soc., 1663.
- [5] HAVERS, C. *Osteologia nova*. Samuel Smith, London, 1691.
- [6] SCHMIDT, W. J. *Die Bausteine des Tierkörpers in Polarisiertem Lichte*. F. Cohen Verlag, Bonn, 1924.
- [7] SKINNER, H. C. W. Biominerals. *Mineralogical Magazine* **69**, 5 (2005), 621–641.

- [8] MANN, S. *Biomineralization: Principles and concepts in bioinorganic materials chemistry*. Oxford University Press, 2001.
- [9] POLITI, Y., ARAD, T., KLEIN, E., WEINER, S., AND ADDADI, L. Sea urchin spine calcite forms via a transient amorphous calcium carbonate phase. *Science* **306** (2004), 1161–4.
- [10] CÖLFEN, H., AND ANTONIETTI, M. Mesocrystals: inorganic superstructures made by highly parallel crystallization and controlled alignment. *Angewandte Chemie (International ed. in English)* **44** (2005), 5576–91.
- [11] SONG, R.-Q., AND CÖLFEN, H. Mesocrystals—ordered nanoparticle superstructures. *Advanced Materials* **21** (2010), 1–30.
- [12] MELDRUM, F. C., AND CÖLFEN, H. Controlling mineral morphologies and structures in biological and synthetic systems. *Chemical Reviews* **108**, 11 (2008), 4332–4432.
- [13] CÖLFEN, H., AND MANN, S. Higher-order organization by mesoscale self-assembly and transformation of hybrid nanostructures. *Angewandte Chemie (International ed. in English)* **42**, 21 (2003), 2350–65.
- [14] PETERS, J., DEŽELIČ, G., AND TEŽAK, B. Monodisperse sols of barium sulfate. III. Electron-microscopic study of internal structure of particles. *Croatica Chemica Acta* **40** (1969), 183186.
- [15] HSU, W. P., RÖNNQUIST, L., AND MATIJEVIĆ, E. Preparation and properties of monodispersed colloidal particles of lanthanide compounds. 2. cerium(iv). *Langmuir* **4**, 1 (1988), 31–37.
- [16] CÖLFEN, H., AND ANTONIETTI, M. *Mesocrystals and nonclassical crystallization*. John Wiley & Sons, New York, 2008.
- [17] SELLEY, R. C. *Applied sedimentology*. No. 2nd. ed. Academic Press, San Diego, San Francisco, New York, Boston, London, Sydney, Tokyo, 2000.
- [18] SCHMIDT, W. J. *Calcit, Baustein des Lebens*. Münchner Mineralientage Fachmesse, München, 1990.
- [19] JONES, A. *Collins Wild guide. Rocks & minerals*. HaperCollinsPublisher, London, 2000.
- [20] STRUNZ, H., AND NICKEL, E. H. *Strunz mineralogical tables*, 9 ed. Schweizerbart’sche Verlagsbuchhandlung (Nägele u. Obermiller), Stuttgart, 2001.
- [21] OKRUSCH, M., AND MATTHES, S. *Mineralogie: Eine Einführung in die spezielle Mineralogie, Petrologie und Lagerstttenkunde*, 7. ed. Springer-Verlag, Berlin, Heidelberg, New York, 2005.

-
- [22] WANG, J., AND BECKER, U. Structure and carbonate orientation of vaterite (CaCO₃). *American Mineralogist* **94** (2009), 380–386.
- [23] ANTAO, S. M. The crystal structure of a biogenic aragonite from the nacre of an ammonite shell. *RSC Advances* **2** (2012), 526–530.
- [24] MARSH, M. E. Regulation of CaCO₃ formation in coccolithophores. *Comparative Biochemistry and Physiology Part B: Biochemistry and Molecular Biology* **136** (2003), 743–754.
- [25] PARIENTE, V. Coccolithophores at home in the Gulf of Mexico. *Quarterdeck* **5**, 2 (1997), 1–12.
- [26] WINTER, A., AND SIESSER, G. W., Eds. *Coccolithophores*. University Press, Cambridge, 1994.
- [27] BROWN, C. W., AND YODER, J. A. Coccolithophorid blooms in the global ocean. *Journal of Geophysical Research* **99**, C4 (1994), 7467–7482.
- [28] WESTBROEK, P., BROWN, C. W., VAN BLEIJSWIJK, J., BROWNLEE, C., BRUMMER, G. J., CONTE, M., EGGE, J., FERNANDEZ, E., JORDAN, R., KNAPPERTSBUSCH, M., STEFELS, J., VELDHUIS, M., VAN DER WAL, P., AND YOUNG, J. R. A model system approach to biological climate forcing. The example of *Emiliana huxleyi*. *Global and Planetary Change* **8** (1993), 27–46.
- [29] RILEY, J., CHESTER, J. P., AND CHESTER, R., Eds. *Treatise on chemical oceanography*. Academic Press, London, 1976.
- [30] STANLEY, S. M. *Earth system history*. W.H. Freeman and Company, New York, 1999.
- [31] YOUNG, J. R., BERGEN, J. A., BOWN, P. R., BURNETT, J. A., FIORENTINO, A., JORDAN, R. W., KLEIJNE, A., VAN NIEL, B. E., ROMEIN, A. J. T., AND VON SALTS, K. Guidelines for coccolith and calcareous nannofossil terminology. *Palaeontology* **40**, 4 (1997), 875–912.
- [32] MCINTYRE, A. Coccoliths as paleoclimatic indicators of Pleistocene glaciation. *Science* **158** (1967), 1314–1317.
- [33] YOUNG, J. R., AND HENRIKSEN, K. Biomineralization within vesicles: The calcite of coccoliths. *Reviews in Mineralogy and Geochemistry* **54** (2003), 189–215.
- [34] MARSH, M. E. Biomineralization in coccolithophores. *Gravitational and Space Biology Bulletin* **12**, 2 (1999), 5–14.
- [35] YOUNG, J. R., DIDYMUS, J. M., BOWN, P. R., PRINS, B., AND MANN, S. Crystal assembly and phylogenetic evolution in heterococcoliths. *Nature* **356** (1992), 516–518.

- [36] WESTBROEK, P., YOUNG, J. R., AND LINSCHOOTEN, K. Coccolith production (biomineralization) in the marine alga *Emiliana huxleyi*. *Journal of Protozoology* **36**, 4 (1989), 368–373.
- [37] FAGERBAKKE, K. M., HELDAL, M., NORLAND, S., HEIMDAL, B. R., AND BATVIK, H. *Emiliana huxleyi* - chemical-composition and size of coccoliths from enclosure experiments and a Norwegian fjord. *Sarsia* **79**, 4 (1994), 349–355.
- [38] DIDYMUS, J. M., YOUNG, J. R., AND MANN, S. Construction and morphogenesis of the chiral ultrastructure of coccoliths from the marine alga *Emiliana huxleyi*. *Proceedings of the Royal Society London B: Biological Sciences* **258** (1994), 237–245.
- [39] WILBUR, K. M., AND WATABE, N. Experimental studies on calcification in molluscs and the alga *Coccolithus huxleyi*. *Annals of the New York Academy of Sciences* **109** (1963), 82–112.
- [40] KLAVENESS, D., AND PAASCHE, E. *Physiology of coccolithophorids. In: Biochemistry and physiology of Protozoa, Vol. 1.* Academic Press, London, 1979.
- [41] YOUNG, J. R., GEISEN, M., CROS, L., KLEIJNE, A., SPRENGEL, C., PROBERT, I., AND ÖSTERGAARD, J. A guide to extant coccolithophore taxonomy. *Journal of Nannoplankton Research. Special Issue* **1** (2003), 1–132.
- [42] GEISEN, M., BILLARD, C., BROERSE, A. T. C., CROS, L., IAN, P., AND YOUNG, J. R. Life-cycle associations involving pairs of holococcolithophorid species: intraspecific variation or cryptic speciation? *European Journal of Phycology* **37** (2002), 531–550.
- [43] SOLOMON, S., QIN, D., MANNING, M., CHEN, Z., MARQUIS, M., AVERYT, K. B., TIGNOR, M., AND MILLER, H. L., Eds. *Climate change 2007: The physical science basis: Contribution of working group I to the fourth assessment report of the intergovernmental panel on climate change.* Cambridge University Press, Cambridge, United Kingdom and New York, 2007.
- [44] LÜTHI, D., LE FLOCH, M., BEREITER, B., BLUNIER, T., J.-M., B., SIEGENTHALER, U., RAYNAUD, D., JOUZEL, J., FISCHER, H., KAWAMURA, K., AND STOCKER, T. High-resolution carbon dioxide concentration record 650,000-800,000 years before present. *Nature* **453** (2008), 379–382.
- [45] SABINE, C. L., AND FEELY, R. A. The oceanic sink for carbon dioxide. In *Greenhouse Gas Sinks*, D. Reay, N. Hewitt, J. Grace, and K. Smith, Eds. CABI Publishing, Oxfordshire, UK, 2007, pp. 31–49.
- [46] BOLLMANN, J., HERRLE, J. O., CORTÉS, M. Y., AND FIELDING, S. R. The effect of sea water salinity on the morphology of *Emiliana huxleyi* in plankton and sediment samples. *Earth and Planetary Science Letters* **284** (2009), 320–328.

- [47] BOLLMANN, J., AND HENDERIKS, J. Global calibration of *Gephyrocapsa* coccolith abundance in Holocene sediments for paleotemperature assessment. *Paleoceanography* **17**, 3 (2002), 7–1–7–9.
- [48] SCHMIDT, D. N., RENAUD, S., AND BOLLMANN, J. Response of planktic foraminiferal size to late Quaternary climate change. *Paleoceanography* **18**, 2 (2003), 17–1–17–12.
- [49] BOLLMANN, J., AND HERRLE, J. O. Morphological variation of *Emiliania huxleyi* and sea surface salinity. *Earth and Planetary Science Letters* **255** (2007), 273–288.
- [50] FEELY, R., SABINE, C., LEE, K., BERELSON, W., KLEYPAS, J., FABRY, V., AND MILLERO, F. Impact of anthropogenic CO₂ on the CaCO₃ system in the oceans. *Science* **305** (2004), 362–366.
- [51] DONEY, S. C., FABRY, V. J., FEELY, R. A., AND KLEYPAS, J. A. Ocean acidification: the other CO₂ problem. *Annual Review of Marine Science* **1** (2009), 169–192.
- [52] BOYD, P. W., DONEY, S. C., STRZEPEK, R., DUSENBERRY, J., LINDSAY, K., AND FUNG, I. Climate-mediated changes to mixed-layer properties in the Southern Ocean: assessing the phytoplankton response. *Biogeosciences* **5** (2008), 847–864.

3 Materials and preparation methods

3.1 Iceland spar

In this thesis mineralogical single-crystalline calcite samples were used for comparison with biologically formed calcite. Iceland spar crystals were bought from the company “Stein-depot”. These crystals were colourless and had a size of about 5 to 30 mm (Fig. 3.1).



Figure 3.1 Iceland spar crystal that was used to prepare TEM samples.

3.2 Coccolithophores

Within this work two different coccolithophore species *E. huxleyi* and *C. leptoporus* were studied. Six different sample series were used, which will be described in more detail in the following chapter.

3.2.1 *Emiliana huxleyi*

To investigate the ultrastructure and the influence of the habitat on the morphology and the crystallographic assembly of *E. huxleyi* five different samples were used.

The first sample series (POS 334 stat.4 MSN K7) was provided by Dr. Hartmut Schulz (Eberhard Karls University Tübingen). This sample contained North Atlantic material from 0-100 m, 100-200 m, 200-300 m, 300-500 m and 500-700 m water depth. After the sample taking the water samples were preserved with formalin and hexamine to avoid bacterial growth and to buffer the carbonate system. The samples were provided in 250 ml bottles containing seawater and plankton particles with sizes smaller than 100 μm .

A second sample series from the South Atlantic (PMT 18, CTD 89) was provided by Dr. Jeremy Young (Earth Sciences, University College London, UK). This series likewise contains samples from three different water depths, 0 m, 48 m and 96 m. As described above the samples were treated with formalin and hexamine. Afterwards the samples were sieved so only particles smaller than 20 μm were left. The sieved sample material was then dispersed onto a Millipore filter using a Vacuum pump.

Dr. Hartmut Schulz also provided the third sample series stemming from the Arabian Sea (Met 31/1 stat.113 MSN 971). The sample derives from 0-100 m water depth. Like the other samples it was treated with formalin and hexamine and provided in a 250 ml bottle seawater and particles with sizes smaller than 100 μm .

The fourth sample series were cultured specimens provided by Dr. Gerald Langer (University of Cambridge, UK). The sample was filtered directly after the collection with a vacuum pump onto an Omnipore polycarbonate membrane filter (diameter: 47 mm, pore size: 0.45 μm) and dried at 60 °C. The growth parameters are listed below:

1. Strain: RCC1238 from the Roscoff Culture Collection (www.sb-roscoff.fr/Phyto/RCC)
2. Nutrients:
 - 100 $\mu\text{mol L}^{-1}$ nitrate
 - 6.25 $\mu\text{mol L}^{-1}$ phosphate
 - trace metals and vitamins according to f/2 [1]
 - aged, sterile-filtered (0.2 μm pore-size cellulose-acetate filters) North Sea seawater
3. Light concentration: 400 $\mu\text{mol/m}^{-2}\text{s}^{-1}$
4. Temperature: 20 °C
5. Salt concentration: 35

A fifth sample series grown under different CO_2 values was provided by Dr. L. Miersch (Geomar, Kiel). The samples were provided as triplicates in approximately 100 ml bottles containing the culture in seawater. formaldehyde was used to avoid bacterial growth and to conserve the sample. The growth parameters are listed below:

1. average CO_2 (microatm):
 - 400
 - 1100
 - 2200
2. Strain: #62
3. Nutrients:

- 64 $\mu\text{mol kg}^{-1}$ nitrate
 - 4 $\mu\text{mol kg}^{-1}$ phosphate
 - trace metals and vitamins according to f/8
 - 10 nmol kg^{-1} selenium
 - 2 ml kg^{-1} sterile filtered North Sea water
4. Light concentration: 150 $\mu\text{mol photons m}^{-2}\text{s}^{-1}$
 5. Temperature: 15 °C
 6. Salt concentration: 35
 7. Cell concentration: 40 000 - 120 000 cell/ml
 8. formaldehyde concentration: 2.7 %

3.2.2 *Calcidiscus leptoporus*

The *C. leptoporus* sample series were cultured specimens provided by Dr. Gerald Langer (University of Cambridge, UK). The samples were provided as triplicates in approximately 200 ml bottles containing the culture in seawater. To avoid bacterial growth and to conserve the sample formaldehyde was used. The growth parameters are listed below:

1. average CO_2 (microatm):
 - 200
 - 477
 - 834
 - 1082
 - 1530
2. Strain: RCC1130 from the Roscoff Culture Collection (www.sb-roscoff.fr/Phyto/RCC)
3. Nutrients:
 - 100 $\mu\text{mol kg}^{-1}$ nitrate
 - 14 $\mu\text{mol kg}^{-1}$ phosphate
 - trace metals and vitamins according to f/2 [1]
 - aged, sterile-filtered (0.2 μm pore-size cellulose-acetate filters) North Sea seawater
4. Light concentration: 300 $\mu\text{mol/m}^{-2}\text{s}^{-1}$
5. Temperature: 20 °C

6. Salt concentration: 35
7. Cell concentration: 3 000 - 4 000 cell/ml
8. formaldehyde concentration: 2.7 %

3.3 TEM Sample preparation methods

For TEM measurements a sample thickness of around 20 to 100 nm is required. This can be achieved using different preparation techniques. The preparation of suitable TEM coccolith samples is challenging due to their small size (between 2 and 3 μm). In addition, the distinction of the different species is important. Different methods to obtain cross-section and plan-view TEM samples were tested:

1. Cross-section preparation

- Embedding of the sample in electron stable glue (LR-White) and glueing it into a metal tube, slicing the tube, grinding and dimpling the discs, and ion-milling them in the end.
- Dropping of the sample onto a silicon (Si)-Wafer and glueing into a metal tube followed again by slicing, grinding, dimpling and ion-milling in the end.
- Dropping of the sample onto a very thin glass plate and embedding of the glass plate into a metal tube followed by the procedure described above.

The obtained metal tubes were prepared following the procedure described by [2]. In order to protect the organic content temperatures above 40 °C were prevented.

2. Plan-view preparation

- Dropping the sample onto a copper TEM grid with a holey carbon film.
- Ultrasonicate the sample for two minutes and dropping it onto a copper TEM grid with a holey carbon film.
- Dropping the sample onto a copper TEM grid with a holey carbon film and etching it afterward with hydrochloric acid (HCl) for a few seconds.

The listed preparation methods were not successful. However during this work it was possible to develop and improve preparation methods for TEM cross-section and for plan-view samples. They will be described in the chapters 3.3.2, 3.3.3, 6.2.1, 7.3.1, 8.2 and 9.2 in more detail.

3.3.1 Sample pretreatment

The *E. huxleyi* samples from the North Atlantic and the Arabian Sea were sieved using a sprinkler and sieves with a mesh size of 50 and 20 μm to leave only particles smaller than 20 μm in the sample. To reduce the water volume of these samples, they were left static for four days. After that time the particles sank to the ground and the remaining water could be removed using a pipette.

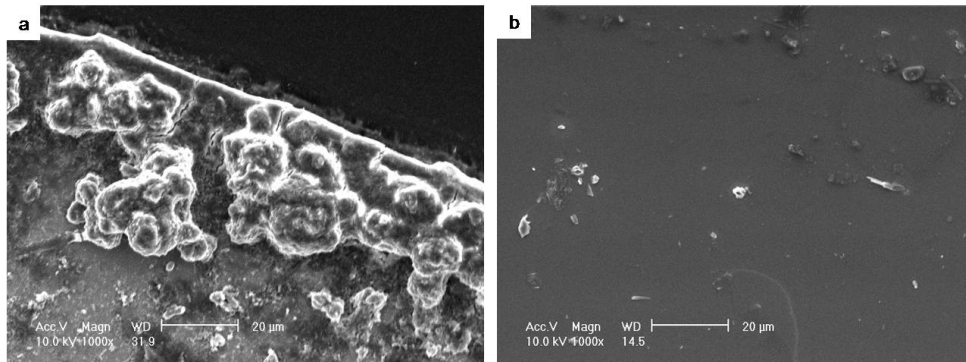


Figure 3.2 Comparison between samples with and without dialysis.

- a) SEM image before dialysis with a clearly visible salt crust.
- b) SEM image after dialysis. The salt crust is strongly reduced.

The samples which were not provided as filter samples contained a high amount of salt. When the sample is dropped onto a substrate the salt will crystallize and form a massive crust (Fig. 3.2a). To avoid this process two different methods to lower the salt concentration were developed. Either the samples were dialyzed for around 140 hours using distilled water (dH_2O) (Fig. 3.2b) or the samples were filtered using a Nuclepore polycarbonate membrane filter (diameter: 47 mm, pore size: 0.8 μm). After the filter dried, the sample was removed with a spatula and dissolved in ethanol, dH_2O or bi-distilled water (bi dH_2O).

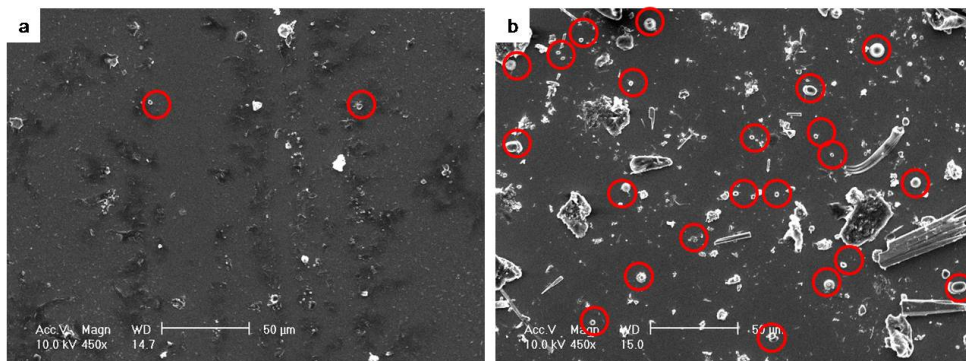


Figure 3.3 Comparison between samples with and without centrifugation.

- a) SEM image before centrifugation with a low coccolith concentration.
- b) SEM image after centrifugation. It can be seen that the coccolith concentration was enhanced.

An additional problem concerning the samples from the North Atlantic and the Arabian Sea was the low coccolith concentration (Fig. 3.3a). A centrifugation of 5 min at 3000 rpm was gentle enough to preserve the fine coccolith structure and to enhance the concentration (Fig. 3.3b).

3.3.2 Plan-view sample preparation

In general, plan-view samples can be prepared easily by dropping the sample which is dispersed in a liquid, onto a TEM copper grid with a holey carbon film. It is important to note that an appropriate concentration of the sample has to be found, and that the particles are not thicker than 100 nm.

For the coccolith plan-view preparation copper finder grids with a holey carbon film were used. These grids are marked with letters and numbers, which allow using the same specimen for several analyses in the SEM and the TEM. Furthermore, the species of interest can be selected. The coccoliths have a thickness of around 500 nm at the thickest area. So for the TEM measurements they have to be thinned. This was performed by etching the samples. CaCO_3 is very sensitive to acid. Therefore the finder grid was kept in dH_2O for 2 h to remove the salt crust, which appears despite dialysis, and dried afterwards in air. Depending on the species the samples were put in dH_2O again. *E. huxleyi* was kept in dH_2O for 36 h or for 5 h in bi dH_2O and *C. leptoporus* for 16 h in bi dH_2O until the coccoliths were thin enough for analyses using the TEM. This method is very gentle and the fine coccolith structure is preserved. More details are given in chapter 7.

For comparison Iceland spar samples were prepared in a similar way but the crystals were pulverized first using a mortar. The received powder was kept in bi dH_2O for 26 h before it was dropped on a TEM copper grid with a lacey carbon film. These samples were air dried at room temperature and could be used immediately without further etching. To avoid contamination these samples were plasma cleaned for 20 s directly before the TEM investigations.

3.3.3 Cross-section sample preparation

The coccolith cross-section samples were prepared using the focused ion beam (FIB) microscope. The samples used in this work were prepared in cooperation with Sonja Matich (Walter Schottky Institut, TUM, Garching).

Before the FIB sectioning starts a thin carbon layer is deposited on the coccolith using electron beam induced deposition (EBID) at 2.5 keV and ion beam induced deposition (IBID) with a beam current of 300 pA at 30 keV to avoid radiation damage under gallium ion bombardment [3]. The resulting layer has a thickness of about 1 μm and will protect the coccolith from radiation damage during the lamellae cutting process. Afterwards two trapezes before and behind the coccolith are cut into the substrate e.g. filter paper or Si-Wafer (Fig. 3.4a). This is done under an angle of 54° with a beam current of 6.5 nA at 30 keV. Then the edges except of one will be cut using a beam current of 700 pA at 30 keV and a manipulator needle is fixed with amorphous carbon at the lamellae surface at 0° tilt (Fig. 3.4b). The remaining edge will be cut free and

the lamellae can be transferred to a TEM lamellae grid, where it will be fixed using amorphous carbon (Fig. 3.4c). After that the manipulator needle is cut off using a beam current of 700 pA at 30 keV. Now the lamellae is thinned and polished from both sides under an angle of 54° and 54.8° using a beam current of 300 and 80 pA at 30 keV for thinning and of 40 pA at 30 keV for polishing. In the end the lamellae has a thickness of around 70 to 100 nm (Fig. 3.4d). More details are given in chapter 7.

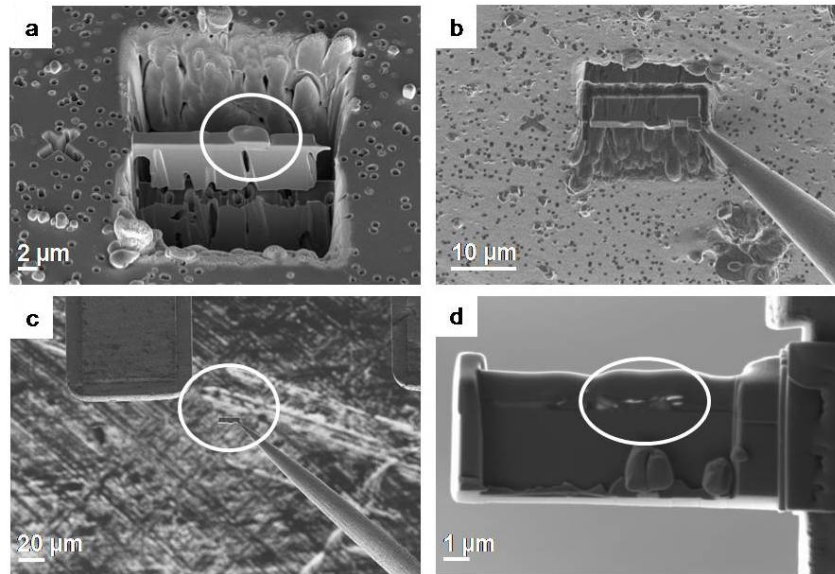


Figure 3.4 Four selected steps of the FIB lamellae preparation process of the coccolithophore species *E. huxleyi*.

- a) Cutting out a TEM lamellae of *E. huxleyi* (marked by white circle).
- b) Fixing the lamellae to the tip of the preparation nozzle with amorphous carbon.
- c) Transferring the lamellae (marked by white circle) onto the TEM grid.
- d) Prepared TEM lamellae of *E. huxleyi* (marked with a circle) with a final thickness of around 70 nm.

To study the influence of the FIB cutting process, samples of the Iceland spar crystals were prepared in a similar way. At the beginning the crystals were pulverized and then dissolved in approximately 1 ml ethanol. The sample was dropped on a Si-Wafer and dried at room temperature. The Si-Wafer was glued with a carbon sticker to a SEM holder and finally a thin carbon film was deposited on the samples with a BAL-TEC coating system. The Iceland spar samples were then FIB sectioned as described above for the coccoliths.

3.4 Bibliography

- [1] GUILLARD, R. R. L., AND RYTHER, J. H. Studies of marine planktonic diatoms, I, *Cyclotella nanna* (Hustedt) and *Detonula convolvacea* (Cleve). *Canadian Journal of Microbiology* **8**, 2 (1962), 229–239.

- [2] STRECKER, A., SALZBERGER, U., AND MAYER, J. Probenpräparation für Transmissionselektronenmikroskopie: Verlässliche Methode für Querschnitte und brüchige Materialien. Specimen preparation for transmission electron microscopy: Reliable method for cross-sections and brittle materials. *Praktische Metallographie* **30**, 10 (1993), 482–495.
- [3] MAYER, J., GIANNUZZI, L. A., KAMINO, T., AND MICHAEL, J. TEM sample preparation and FIB-induced damage. *MRS Bulletin* **32** (2007), 400–407.

4 Characterisation methods

4.1 Electron microscopy

To investigate the nanostructure and the crystallographic assembly of small organisms like coccolithospheres optical microscopes become more and more replaced by high resolution electron microscopes. These microscopes use electrons to irradiate the sample and to produce a magnified image [1, 2]. Since the wavelength of electrons is about 100,000 times shorter than visible light, this method allows a resolution of about 0.1 Å [1, 2]. In comparison the resolution of conventional light microscopes is limited by diffraction to approximately 200 nm [1, 2]. The electron microscope types and the corresponding analytical methods used in this thesis are described in more detail in the following chapters.

4.2 Scanning electron microscopy

A SEM is mainly used to study surface and near surface structures of bulk and nanostructured materials. It employs a beam of electrons, which is generated either by a tungsten filament (thermionic emission) or by a LaB₆-crystal (field emission) and is focused on the sample [1]. Electrons are usually accelerated to an energy between 1 and 30 keV in the SEM [1]. The inter-

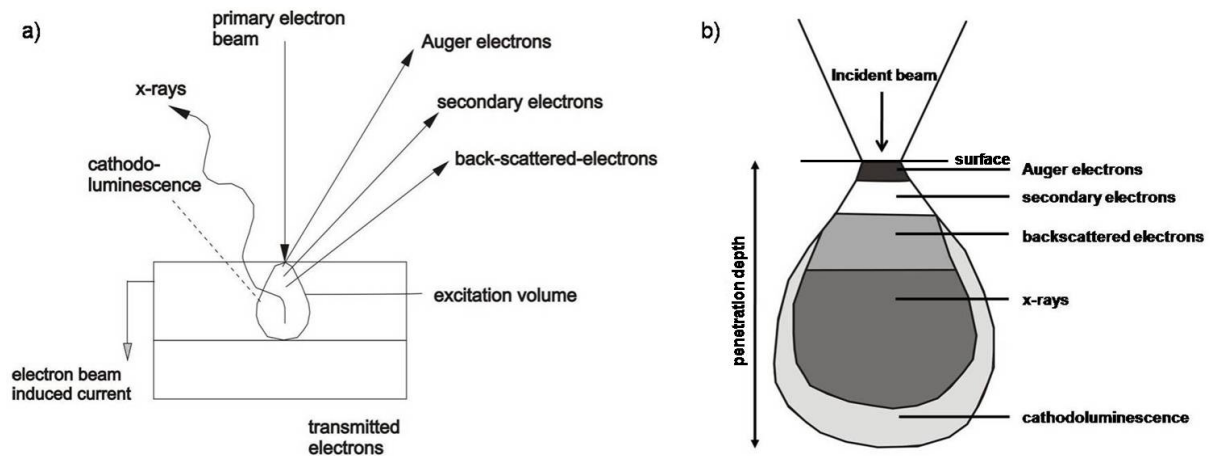


Figure 4.1 Interaction between primary electron beam and the bulk material.

a) Signals which can occur in the SEM. Figure modified from [1].

b) Interaction volume modified from [1] with the escape depth of the signals used in the SEM marked.

action between the primary electron beam and the sample generates several signals (Fig. 4.1a),

which can be used for imaging or for analytical purposes. These signals will be generated within the interaction volume, but can only escape from different sample depths [1] (Fig. 4.1b).

The condenser and objective lenses bundles the electron beam, so that it has a diameter of around 2 to 10 nm when it hits the sample [1]. This fine electron beam is scanned over the sample by the scanning coils [1]. For the image generation mostly secondary electrons (SE) are used. These electrons have an energy between 0 and 50 eV and are generated by inelastic scattering between the primary electron and the specimen [1]. They are emitted from a sample depth of a view tens of nanometers and therefore give information about the surface [1]. The higher energetic back-scattered electrons (BSE), which are emitted from a large depth and hence have a lower spatial resolution, can also be used for the image generation [1]. The laterally fixed Everhardt-Thornley detector counts the number of SE emitted from each point of the sample surface [1]. The signal is amplified by a photomultiplier and transformed into grey scale value information [1]. The main components of a SEM are given in figure 4.2. The three-dimensional

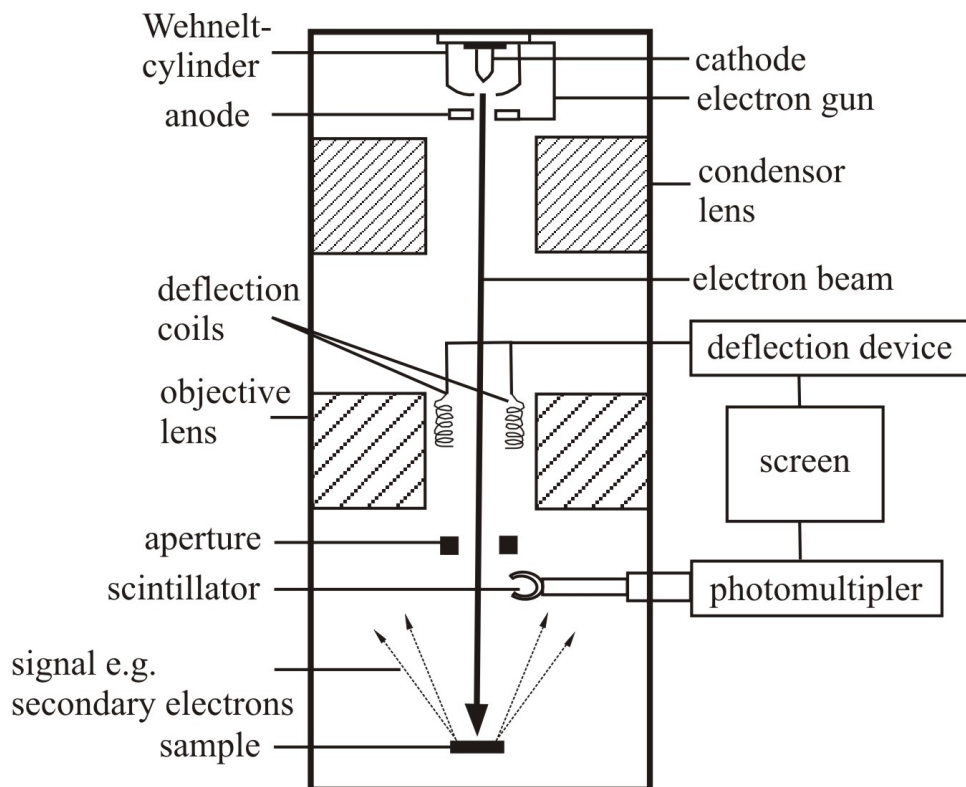


Figure 4.2 Schematic drawing indicating the main components of a SEM modified from [3].

appearance of objects in the SEM is caused by so called edge effects (a large number of electrons can escape) and by shadowing effects [4]. The detector is laterally fixed in the microscope, so electrons which are emitted from a detector abandoned side can not reach it and this side appears dark, while areas facing the detector appear brighter [4]. Therefore, all objects look like they are illuminated from one side [4]. This effect correlates with the rate of light and shadow in the classical light optics [4].

4.3 Focused ion beam microscopy

The FIB is mainly used for surface analytics and surface modification. FIB microscopes allow a controlled erosion of surface material and sputtering [5]. Instead of electrons ions are used (mainly Gallium and Helium). Hence this instrument is not really an electron microscope but nevertheless it has many structural features in common with a SEM [6].

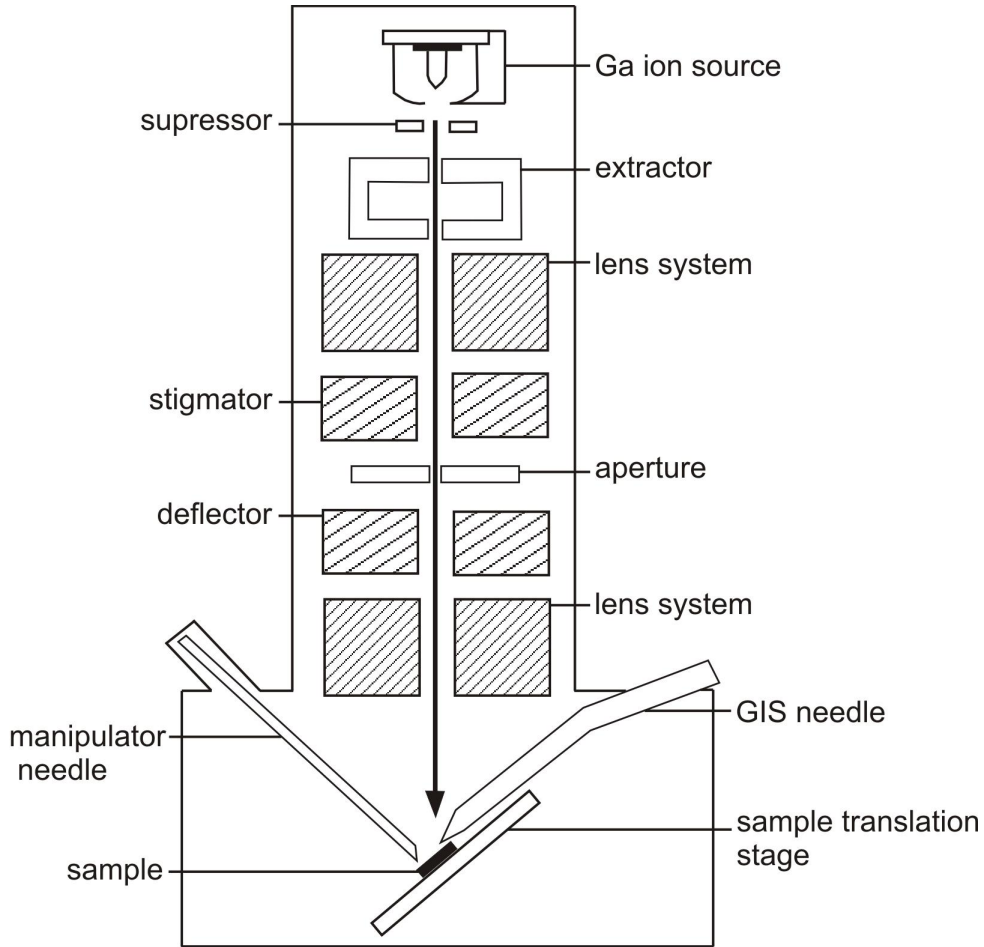


Figure 4.3 Schematic drawing indicating the main components of a FIB microscope modified from [6].

In figure 4.3 the general assembly of a FIB microscope is illustrated. The ions are generated in a liquid metal ion source (LMIS) that operates by field evaporation of liquid metal at a tungsten tip which is maintained at a high positive potential [5]. A big difference between an electron microscope and a FIB microscope is the design of the microscope column. Due to the large mass of the ions electrostatic lenses instead of electromagnetic are used to focus the beam [6]. A sequence of beam-blanking plates with both variable and fixed apertures is used to minimize the sputtering damage [6]. The eucentric stage permits tilting along all three coordinate axes and a full Cartesian, x , y and z , control of the sample position with respect to the optical axis of the ion beam [6]. It is also ensured that the axes of specimen tilt remain perpendicular to, and

pass through, the optical axis [6]. For FIB microscopes many accessories are available like gas injection system (GIS) for chemical-assisted etching of the surface or for deposition of thin films in selected areas [5]. Another useful tool are nano-manipulator needles consisting of a sharp tungsten needle mounted at the end of a piezoelectric drive [5].

In material science microscopes that include both ion beam and electron beam are often used. These machines are often referred to as dual beam instruments. The SEM column is usually mounted vertically above the sample, while the ion beam source and column are mounted at an inclined angle to the sample chamber [6]. With this instrument it is possible to monitor the progress of the ion-beam milling or deposition by the electron beam and the two types of secondary images achieved from either the ion- or the electron-probe provide microstructural information [6].

4.4 Transmission electron microscopy

A TEM is mainly used to analyze inorganic samples (like investigations of the microstructure or grain boundaries of metals, ceramics etc.) [1]. But it is also a helpful tool to study biological samples. It allows investigating the hard tissues like shells or bones as well as the soft tissues like cells or organic membranes [7].

The assembly of a TEM is related to a light microscope but instead of light, electrons are used and electromagnetic coils are employed instead of glass lenses. To avoid interactions between the electron beam and gas particles a high vacuum of around 10^{-6} Torr is necessary [2]. Figure 4.4 shows the general assembly of a TEM with the main components. The electron beam is generated either by thermionic emission or by cold or thermal field emission. For thermal field emission guns the term Schottky emitter is used as well. The wavelength of the generated electron beam depends on the acceleration voltage [2]. In this thesis an acceleration voltage of either 300 or 80 keV was used. With the condenser lens system, which is located below the electron gun, the electron beam is bundled [2].

Below the condenser lens system the sample is located. Since the electrons will pass through the specimen the samples have to be electron transparent (between 100 and 10 nm thickness) [2]. The sample is located between the objective lenses which are used to obtain the first image. This image is further magnified by the projector lenses in the conventional TEM [2]. The magnified image is detected by a charge-coupled device (CCD) camera or will be projected on a fluorescence screen. The image is generated by using the scattering effects of electrons at the sample atoms [2]. This can be elastic scattering without energy loss, Rutherford scattering or inelastic scattering where kinetic energy is lost [2]. These different scattering processes have different scattering angles. They lead to different contrast in the image.

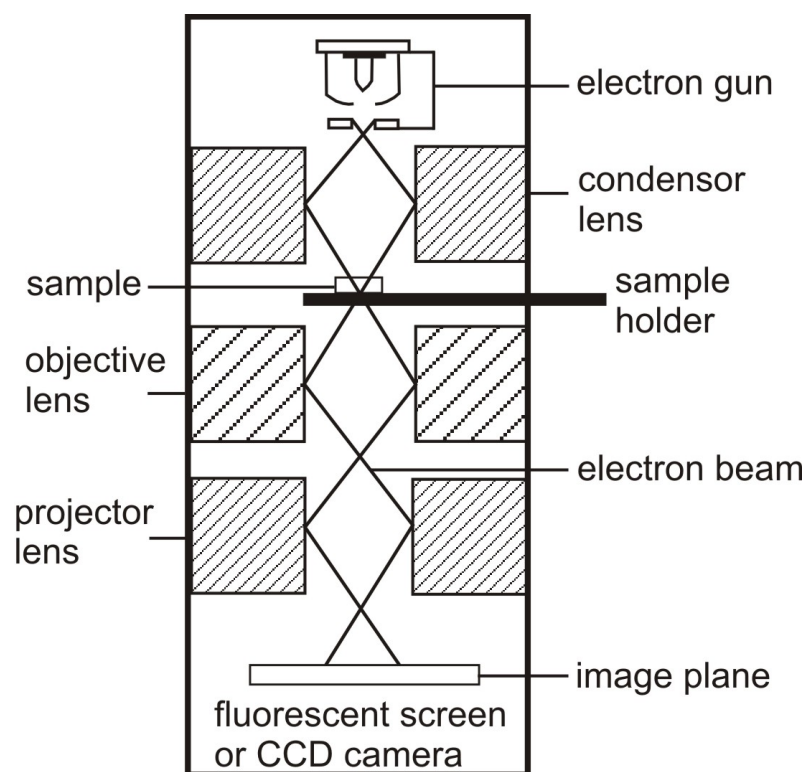


Figure 4.4 Schematic drawing of the main components of a TEM modified from [6].

4.4.1 Bright field and high resolution imaging

The most common imaging mode in the conventional TEM is bright field (BF) imaging. Here the contrast is due to mass-thickness and diffraction effects and is enhanced by the use of the objective aperture [2]. Thicker regions, crystals in a specific zone axis or regions with higher atomic numbers will appear dark while regions with no sample appear bright [2].

By using high resolution (HR)TEM imaging it is possible to display the periodicity of the crystallographic structure of crystalline materials and is therefore a common tool to investigate the nanostructure of samples [8]. Modern microscopes equipped with chromatic and spherical aberration correctors can resolve details ~ 0.1 nm [2]. For this imaging technique very thin samples are necessary (10-50 nm) [2]. For the imaging elastic, coherent electron waves scattered on lattice atoms are used. By interference of the transmitted and diffracted electron waves in the image plane the contrast is formed [8]. The phase contrast diffracted image contains information about the atomic structure [8].

4.4.2 Electron diffraction

Electron diffraction in TEM is often used for structure analysis of solids [8]. When electrons pass through a thin sample they behave wave like rather than particle like [2]. The crystal acts as a periodic structure and electrons are diffracted into different directions [2]. Constructive

interference is observed for diffraction angles Θ , which fulfill the Bragg condition (Eq. 4.1) [2].

$$n\lambda = 2d \cdot \sin \Theta \quad (4.1)$$

In this equation n is an integer that gives the order of the scattering, λ is the wavelength of the incident beam, d is the spacing between the planes in the crystal lattice and Θ is the angle between the incident beam and the scattering planes. As a result diffraction pattern are a series of spots. They can be observed if the projector lens is differently excited [2]. Each of these spots corresponds to a specific plane of the samples crystal structure [2]. By tilting the sample, the crystal will stay under illumination but different diffraction conditions will be achieved [2].

4.4.3 Electron energy low loss spectroscopy

Since the interest in the characterization of organic and inorganic materials at the nano scale is increasing, electron energy-loss spectroscopy (EELS) has become an established analysis method [9]. This technique allows the chemical and electronic characterization of different materials. It is based on measuring the transmitted electrons as function of their energy loss [2]. As figure 4.5 indicates an electron energy-loss (EEL) spectrum can be divided into three parts.

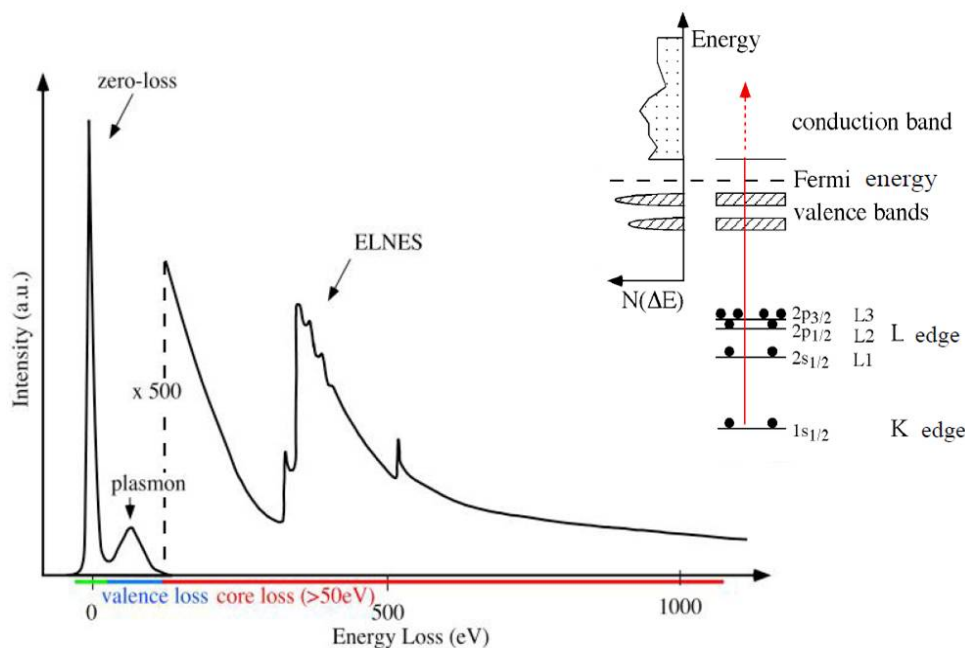


Figure 4.5 Schematic drawing of an EEL spectrum modified from [9].

The first part of the spectrum is the zero loss region, which contains the unscattered or elastically scattered electrons (0 eV). The zero loss peak is used to determine the experimental energy resolution and it allows together with the low loss region to determine the thickness of the sample [9].

It is followed by the low loss region that contains energy losses up to 50 eV. This region is

dominated by the plasmon peak which is caused by the collective oscillations of valence electrons, but it also contains interband transitions (excitations of valence electrons to unoccupied states above the Fermi level) [9]. This feature of the spectra can be used for thickness determination, thickness deconvolution of the core-loss region and phase identification via the position of the plasmon peak [9].

The third region is the core loss region that contains energy losses above 50 eV. By excitations of inner shell electrons to unoccupied states above the Fermi level the element-specific ionization edges will occur [9]. The element specific ionization edges are used for phase identification, determination of chemical composition and the analysis of electronic structure, e.g. bonding behavior or oxidation state [9].

4.5 Bibliography

- [1] GOODHEW, P. J., HUMPHREYS, J. F., AND BEANLAND, R. *Electron microscopy and analysis*, 3 ed. Taylor and Francis, London, New York, 2001.
- [2] WILLIAMS, D. R., AND CARTER, B. C. *Transmission electron microscopy a textbook for material sciences*, 2 ed. Springer-Verlag, New York, 2009.
- [3] GOODHEW, P. J., AND HUMPHREYS, J. F. *Elektronenmikroskopie: Grundlagen und Anwendung*, 2 ed. McGraw-Hill Book Company (UK), Maidenhead, 1991.
- [4] GOLSTEIN, J., NEWBURY, D., JOY, D., LYMAN, C., ECHLIN, P., LIFSHIN, E., SAWYER, L., AND MICHAEL, J. *Scanning electron microscopy and X-ray microanalysis*, 3 ed. Springer-Verlag, Berlin, Heidelberg, New York, 2003.
- [5] REYNTJENS, S., AND PUERS, R. A review of focused ion beam applications in microsystem technology. *Journal of Micromechanics and Microengineering* **11**, 4 (2001), 287.
- [6] BRANDON, D. G., AND KAPLAN, W. D. *Microstructural characterization of materials*, 2 ed. WileyVCH Verlag, Weinheim, 2008.
- [7] BENIASH, E., DEY, A., AND SOMMERDIJK, N. A. J. M. Transmission electron microscopy in biomineralization research. Advances and challenges. In *Biomineralization Sourcebook. Characterization of Biominerals and Biomimetic Materials*, L. B. Gower, Ed. CRC Press, 2014, p. 209231.
- [8] FULTZ, B., AND HOWE, J. M. *Transmission electron microscopy and diffractometry of materials*, 3 ed. Springer-Verlag, Berlin, Heidelberg, New York, 2008.
- [9] BRYDSON, R. *Electron energy loss spectroscopy*. Taylor & Francis, 2008.

5 Experimental details

The following chapter gives a short overview about the used equipment and about chemicals and substrates used during this work.

5.1 Instrumentation

The equipment used during this work is listed in table 5.1.

Instrument	Model	Producer
Precision diamond wire saw	3242	Well
Disc grinder	623	Gatan
Dimple grinder	656	Gatan
Precision ion polishing system (PIPS)	691	Gatan
Carbon coating system		BAL TEC
Enviromental SEM	XL40	FEI
SEM	NSVision40	Zeiss
SEM	JSM-6500F	JEOL
EDX detector	<i>INCA ENERGY</i>	Oxford Instruments
SEM	Leo Modell 1450	Zeiss
Field emissision SEM	UltraPlus	Zeiss
EDX detector	<i>INCA ENERGY</i>	Oxford Instruments
Dual FIB and SEM Manipulator	NSVision40	Zeiss Kleindiek
Dual FIB and SEM	Auriga	Zeiss
Conventional TEM 200 keV	2010	JEOL
Field emission S/TEM 80-300 keV	Titan	FEI
EDX detector		EDAX
Tridiem Electron EELS detector		Gatan
HAADF detector	3000	<i>FISCHIONE INSTRUMENTS</i>

Table 5.1 Overview of the equipment used during this work. The instrument, the model and the producer are listed.

5.2 Chemicals and substrates

In table 5.2 the chemicals and substrates used during this work are listed.

Chemicals/ Substrates	Supplier
Ethanol 99,9%	Merck
Si-Wafer	
Millipore polycarbonate membrane filter diameter: 47 mm, pore size: 0.45 μm	Millipore
Omnipore polycarbonate membrane filter diameter: 47 mm, pore size: 0.45 μm	Whatman
Dialysis membrane	Zellu Trans ROTH
copper finder grid with holey carbon film	Plano

Table 5.2 Overview of the chemicals and substrates used during this work.

6 Nanoprobe crystallographic orientation studies of isolated shield elements of the coccolithophore species *Emiliana huxleyi*

This chapter is based on the following publication:

Hoffmann R., Wochnik A. S., Heinzl C., Betzler S. B., Matich S., Griesshaber E., Schulz H., Kučera M., Young J., Scheu C. and Schmahl W. W. (2014): *European Journal of Mineralogy*, **26** (4) 473-483

6.1 Introduction

Coccolithophorids are one of the most important groups of primary producers in the oceans [1]. They live in almost all marine habitats and are present from arctic to tropical waters [2, 3, 4]. They contribute about 15 % to the global ocean phytoplankton biomass and their calcite exoskeletons are one of the major components of deep sea sediments [5]. Due to their high abundance in sedimentary rocks [6] coccolithophorids are of high interest for biostratigraphic dating and paleoclimate studies [7, 8].

Typical coccoliths are formed inside the cell and show a radial structure. The segment of these coccolith rings are characteristically formed by two alternating types of crystal units with sub-vertical crystallographic *c*-axes (V-units) and sub-radial *c*-axes (R-units), respectively [9, 10, 11]. The R-unit of *E. huxleyi* consists of distal- and proximal shield elements and a central area element connected through the inner- and outer tube elements (Fig. 6.1) [12]. Transmission electron microscopy and scanning electron microscopy investigations showed that in the earliest growth stage of *E. huxleyi* coccoliths, the proto-coccolith ring is an elliptical ring of alternating larger and smaller calcite crystals, which were predicted to also alternate in crystallographic orientation [9, 12, 10]. However, only one of these sets of elements develops during growth of the coccolith, so they constitute almost the entire mature coccolith (Fig. 6.1d). These units have radial *c*-axes and so are R-units hence the alternate units of the proto-coccolith ring were inferred to be V-units. Although these putative V-units have been imaged by electron microscopy in proto-coccolith rings [9], their crystallographic orientation has never been determined directly but only inferred by analogy from other coccoliths. Recent studies used the SEM based electron back-scattered diffraction (EBSD) method [13, 14] and Kikuchi pattern orientation in TEM

[15] for a more accurate determination of crystal orientations of the R- units of several coccolithophore species [13, 14, 15]. Even though the orientation of the crystal units were investigated to some degree in *E. huxleyi* [16, 17, 18, 9, 11, 14] the exact nature of their nanostructure and nanoscale architecture is not fully understood. This includes the crystallographic orientation of the V-unit element.

Many carbonate-sequestering marine shelled organisms such as sea urchins, corals and mollusks have skeletons that show a mosaic like crystal assembly [19, 20, 21, 22, 23, 24, 25, 26, 27, 28, 29] where the biocarbonate crystals in their shells are constituted of co-oriented crystallites in the mesoscopic size range (1-1000 nm) [30]. These mesoscale units are often in very good three dimensional orientational register and show a scattering pattern and behavior in polarized light comparable to that observed in single-crystals [30]. Thus, a further focus of our study was to determine whether the segments of *E. huxleyi* consist of calcite crystals with a mosaic like assembly or of conventional single-crystals. To obtain the required spatial resolution information, we applied TEM and associated analytical techniques including selected area and nano probe diffraction experiments, BF- and HR TEM imaging. To facilitate analysis in cross-section, FIB sample preparation was used. We used coccolithophore specimens collected from oceanographic samples.

6.2 Materials and methods

6.2.1 Samples and preparation

Plankton samples from the North- and the South Atlantic Ocean were investigated. The North Atlantic sample (POS 334, stat. 4 MSN K7) material derives from 0-100 m, 100-200 m, 200-300 m, 300-500 m and 500-700 m water depth and the South Atlantic sample (AMT 18, CTD 89) consists of three samples from 0 m, 48 m and 96 m water depth. Both sample series were preserved with formalin and hexamine after collection to avoid bacterial growth and to buffer the carbonate system.

The target prepared TEM samples were obtained by FIB sectioning. Radiation damage under ion bombardment can easily occur [31]. In order to protect and preserve the structure of the coccolith, a thin (50 nm) carbon layer was deposited by EBID at 3 kV. A further, thicker protection layer was deposited with IBID with a beam current of 300 pA at 30 kV. Here carbon was used as well. The resulting layer thickness of around 1.0 μm was found to be thick enough to protect *E. huxleyi* from radiation damage during the following lamella cutting process. Additional plan-view samples of *E. huxleyi* were prepared from the North Atlantic sample series. The sample was dropped on a copper TEM grid with a holey carbon film. Afterwards the samples were thinned according to the procedure developed by Wilbur and Watabe and Watabe [16, 17]. Instead of using HCl we performed thinning with dH_2O for several h. This has the advantage of being gentler than the HCl treatment, so the fine structure and the full assembly of the coccolith stay intact.

6.2.2 Instrumentation

For SEM imaging and FIB sectioning a Zeiss NVision40 FIB microscope was used, which combines the technologies of a GEMINI electron column, with a focused ion beam (zeta FIB column - operated at 30 kV) and single-injector multi-channel GIS. Secondary electron images were acquired at a low acceleration voltage of 2.5 kV. For TEM investigations we used a FEI Titan 80-300 kV field emission scanning (S)/TEM equipped with an energy-dispersive X-ray spectrometer and a Gatan imaging filter. The measurements were performed at 80 kV. The crystallographic orientations within the coccolith were investigated by BF imaging, selected area electron diffraction (SAED), nano probe diffraction and HR imaging. For the selected area electron diffraction an aperture of approximately 150 nm was used and for the nano probe experiments a beam diameter of around 6 nm was applied.

6.3 Results

A secondary electron image of a complete coccosphere of *E. huxleyi* is given in figure 6.1a. To obtain crystallographic information of the R- and V-unit [9] (model given in Fig. 6.1d) cross-section samples are required. The V-unit can only be seen in the cross-section view as the R-unit overgrows the V-unit during the crystal growth phase of the coccolith formation [9]. The FIB sectioning allowed us to analyze the specimen in the SEM mode and to get a cross-section of the area of interest. Figure 6.1b shows a secondary electron image of a cross-section through a complete coccosphere, where several (minimum 4) concentric layers of coccoliths can be observed. The coccoliths are relatively densely packed. The cell cavity, where the living cell resides, has a diameter of around 4 μm and is clearly visible. The concentric coccolith skeleton has a thickness of about 2.5 μm .

For the TEM investigations we used 6 different cross-section lamellae through single coccoliths. The BF TEM image of figure 6.1c shows exemplary one of those cross-sections. The 0-100 m and 100-200 m sample from the North Atlantic and the three samples from the South Atlantic series (0 m, 48 m, 96 m) were used for this preparation method. We found the optimal thickness of the TEM lamellae to be between 70 nm and 90 nm. With thicker lamellae problems due to double diffraction during electron diffraction experiments occurred, while thinner samples were easily damaged by the electron beam bombardment.

First TEM measurements were performed at 300 kV and a low electron dose, meaning that a low number of electrons hit the sample per m^2 . Our experiments using these parameters indicate that the calcite shell of the coccoliths is very sensitive to beam bombardment, especially during HR imaging and SAED experiments. After a few s of 300 kV electron bombardment the calcite transformed to a poly-crystalline material with d-spacings indicating the formation of calcium oxide (CaO). Since the kind of beam damage differs between 80 kV and 300 kV [32], the parameters for the TEM measurements were changed to an acceleration voltage of 80 kV and a low dose. All experiments shown were performed under these conditions. These

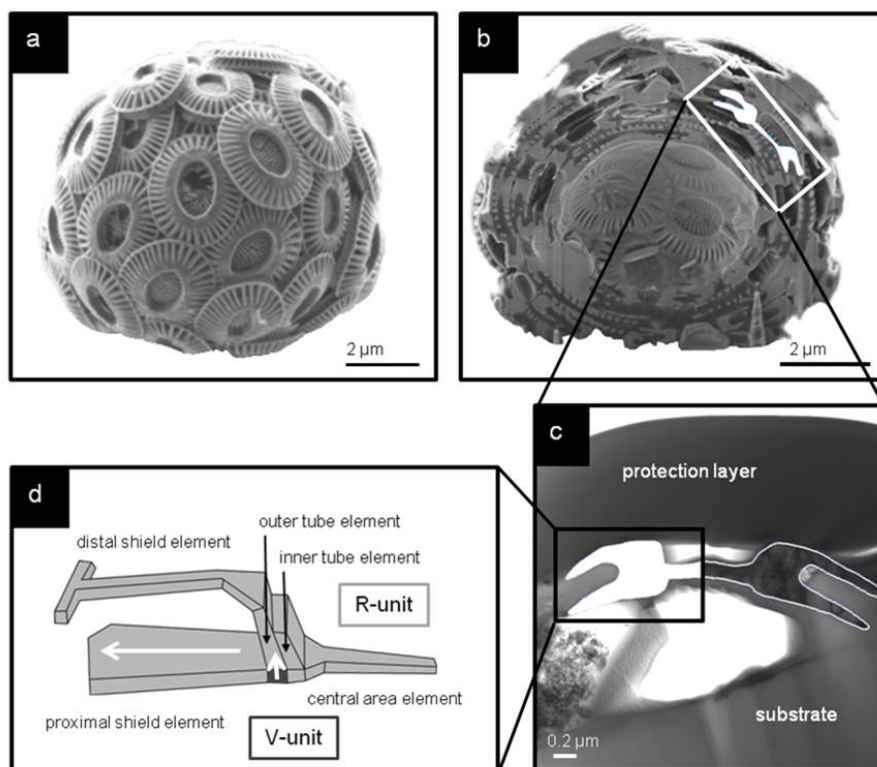


Figure 6.1 Calcite skeleton of the marine alga *E. huxleyi*.

- a) SE image of a complete coccosphere of *E. huxleyi*.
- b) Cross-section obtained by FIB ion-milling through the coccosphere shown in a. The cross-section of a single coccolith is colored white and highlighted by the white frame.
- c) TEM BF image of a cross-section of a single *E. huxleyi* coccolith prepared by FIB sectioning. The coccolith is outlined by a white line. The fully white colored left side of the coccolith cross-section is directly comparable with the schematic model in d).
- d) Simplified schematic drawing modified from [12] of one coccolith segment of *E. huxleyi* to visualize the model of [9]. The R-unit is given in light grey. The longer white arrow pointing parallel to the coccolith plane is indicating the direction of the crystallographic *c*-axis in the R-unit. The V-unit is marked dark grey, with the *c*-axis oriented perpendicular to the coccolith plane (shorter white arrow).

conditions allowed HR imaging and electron diffraction measurements, while the sample stayed intact. However, even under these conditions electron bombardment for more than three min transformed the calcite to CaO.

At 80 kV and a low dose, diffraction patterns of different areas of the cross-section of coccolith segments of *E. huxleyi* were taken from 6 different TEM lamellae. The achieved diffraction patterns were indexed, the lattice orientation was calculated and the *c*-axis was projected into the corresponding BF image (Fig. 6.2). The rotation between image and diffraction pattern is compensated in the used FEI Titan TEM. Our experiments showed that the *c*-axes of the different elements (proximal-, distal- and central area element) within the R-unit of *E. huxleyi*

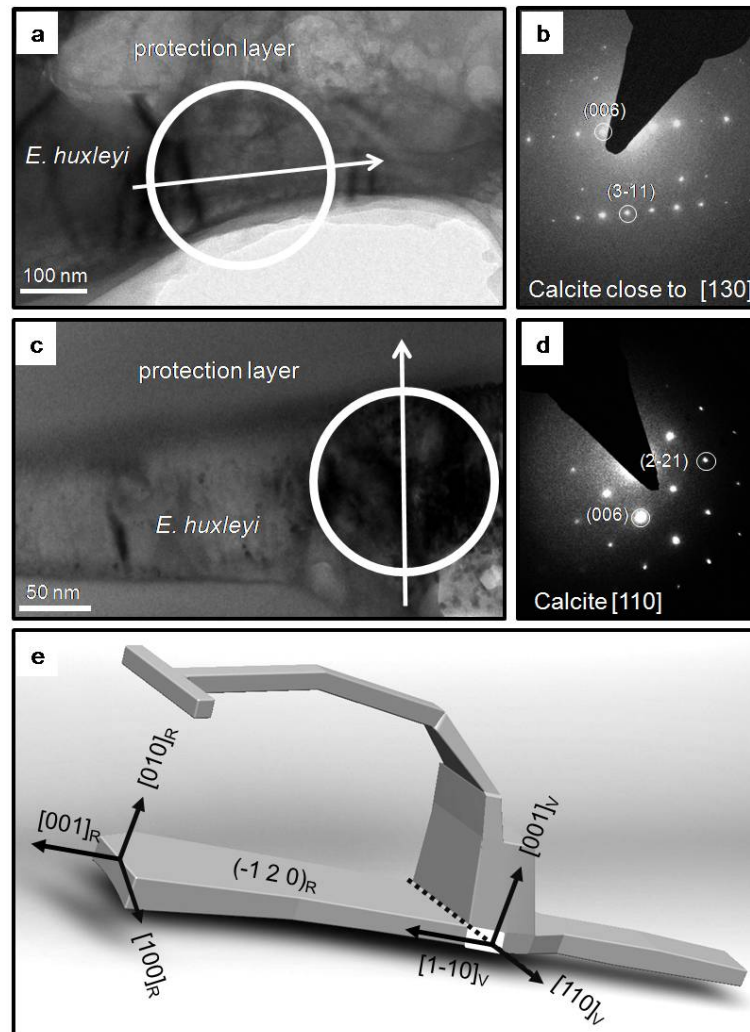


Figure 6.2 V/R unit of *E. huxleyi* coccolith shield elements.

- a) BF TEM image of the proximal shield element of *E. huxleyi*. The white arrow shows the projection of the crystallographic c-axis determined from the diffraction pattern given in b. The b-axis lies perpendicular to the coccolith plane and the c-axis is oriented parallel to the coccolith plane. The angle between the zone axis and the b-axis is approximately 14° .
- b) Electron diffraction pattern of the marked area (white circle in a). The diffraction pattern indicates calcite tilted close to the $[1\ 3\ 0]$ zone axis. During the experiments the tilt angles were $\alpha = 11.6^\circ$ and $\beta = 3.1^\circ$.
- c) A BF TEM image of the V-unit of *E. huxleyi*. The V-unit $[1\ 1\ 0]$ direction is in tangential direction of the coccolith ring and the c-axis (white arrow) direction is pointing perpendicular to the coccolith plane.
- d) Electron diffraction pattern of the marked area (white circle in c) indicating calcite tilted to the $[1\ 1\ 0]$ zone axis. Compared to the diffraction pattern in b, the sample was tilted to $\alpha = 0.7^\circ$ and $\beta = 4.6^\circ$.
- e) Crystallographic orientation of the R- and the V-unit in a three dimensional sketch of coccolith segment of *E. huxleyi*.

lie within the coccolith plane. For the R-unit the b-axis is perpendicular to the coccolith plane (Fig. 6.2e). A representative BF image of an R-unit area is given in figure 6.2a.

In figure 6.2b the corresponding electron diffraction pattern of the encircled area in figure 6.2a is shown. The electron diffraction pattern taken from the area where the V-unit should occur (Fig. 6.2c) reveals that here the $[001]$ direction is perpendicular to that of the R-unit (marked by the white arrow in figure 6.2d). This orientation was predicted by Young *et al.*, based on analogy with other coccoliths [9]. The analysis of our diffraction experiments revealed that the $[110]$ direction of the V-unit is in tangential direction of the coccolith ring and its $[1\bar{1}0]$ direction is radial with respect to the coccolith ring (Fig. 6.2e)

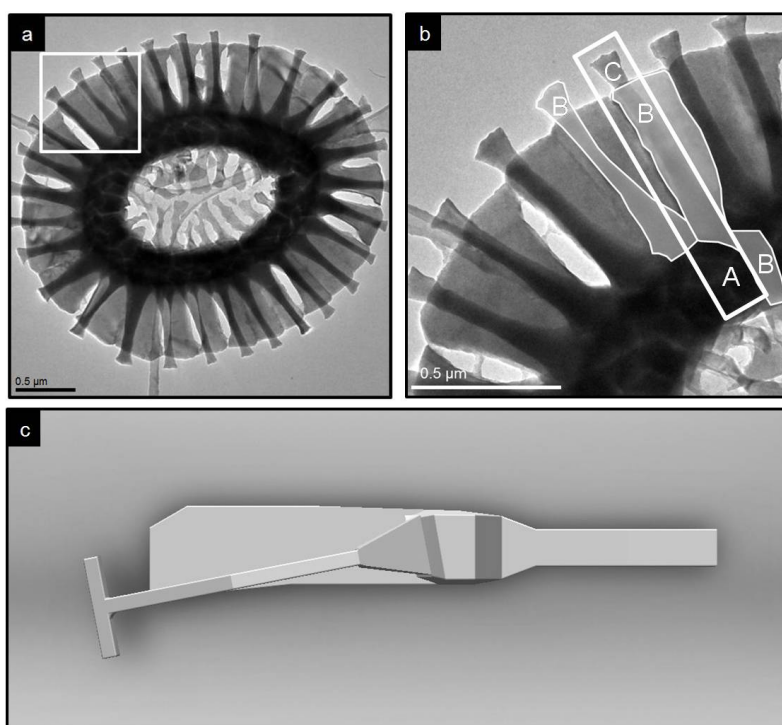


Figure 6.3 Three dimensional structure of *E. huxleyi* segments.

- a) BF TEM image of an incomplete grown coccolith of *E. huxleyi*, in plan-view. The white rectangle marks the area enlarged in b.
- b) Three visible elements composing one segment (distal shield element, proximal shield element and central area element) are outlined by a thin white line and labeled by B. The white rectangle marks the position of a potential FIB-section cutting through the elements of 3 different coccolith segments (A, B, and C). Such a FIB lamella would contain the distal shield element of the coccolith segment C, the proximal shield element of the coccolith segment B, and the central area element of the coccolith segment A.
- c) Three dimensional model to illustrate the complex three dimensional structure of a coccolith segment.

The mesoscale crystallographic constitution of the *E. huxleyi* calcite was investigated by nano probe electron diffraction experiments, as well as by BF and HR imaging with the same param-

eters as given above. Due to the complex three dimensional structures of the coccolith segments (Fig. 6.3c), the FIB cross-section can pass through three different segments instead of one (see BF plan-view image Fig. 6.3). The visible elements (distal shield-, the proximal shield- and the central area element), of one coccolith segment, are labeled as B. The white rectangle marked in figure 6.3b is a potential position for a FIB cross-section. This cross-section would pass through the distal shield element of the segment labeled as C, the proximal shield element of the segment labeled as B, and the central area element of the segment labeled as A. If the *c*-axis is expected to be precisely radial with respect to the ring, measurements using such a cross-section would show different crystal orientations for the elements, as they belong to differently oriented segments (A, B, C). To avoid these problems samples viewed perpendicular to the coccolith ring (plan-view samples) were used in the experiments.

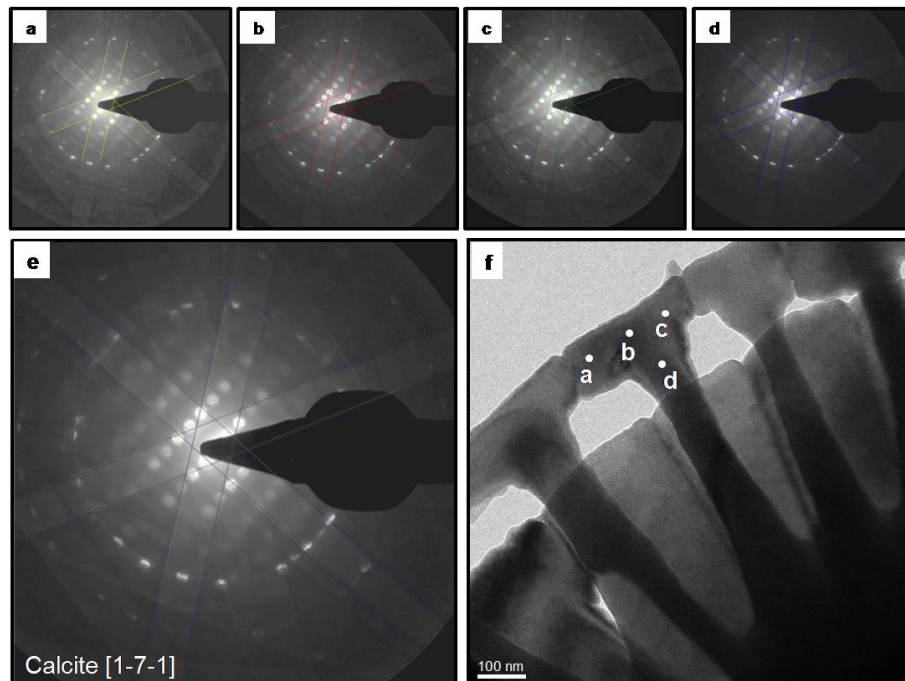


Figure 6.4 Nano probe diffraction within the distal shield element of *E. huxleyi*.

a-d) Nano probe electron diffraction patterns of the distal shield element of *E. huxleyi* marked in the BF image given in 6.4f. The Kikuchi lines are colored in yellow (a), in red (b), in green (c) and in blue (d).

e) Overlain diffraction patterns a-d of the distal shield element. The Kikuchi lines show no evidence of relative misorientations between the patterns a-d within the experimental uncertainty of circa 1° .

f) BF image of a plan-view sample with the position of the diffraction patterns (a-d) marked by white dots.

To investigate the orientation within one coccolith segment and to study the arrangement of the calcite crystals we performed nano probe diffraction experiments on plan-view samples. For these experiments the samples from the North Atlantic series taken from 200-300 m and 300-500 m were used. With this method a high spatial resolution (around 6 nm in our experi-

ments) could be achieved. The measurements were started by tilting one area of the coccolith cross-section to a zone axis. Then these goniometer angles were kept while the whole element was investigated in the diffraction mode by translation of the sample holder. The nano probe diffraction patterns obtained were overlain using a color code for the Kikuchi lines. If any crystallographic orientation variations occurred within one coccolith element, this procedure would enable us to detect this mosaic structure.

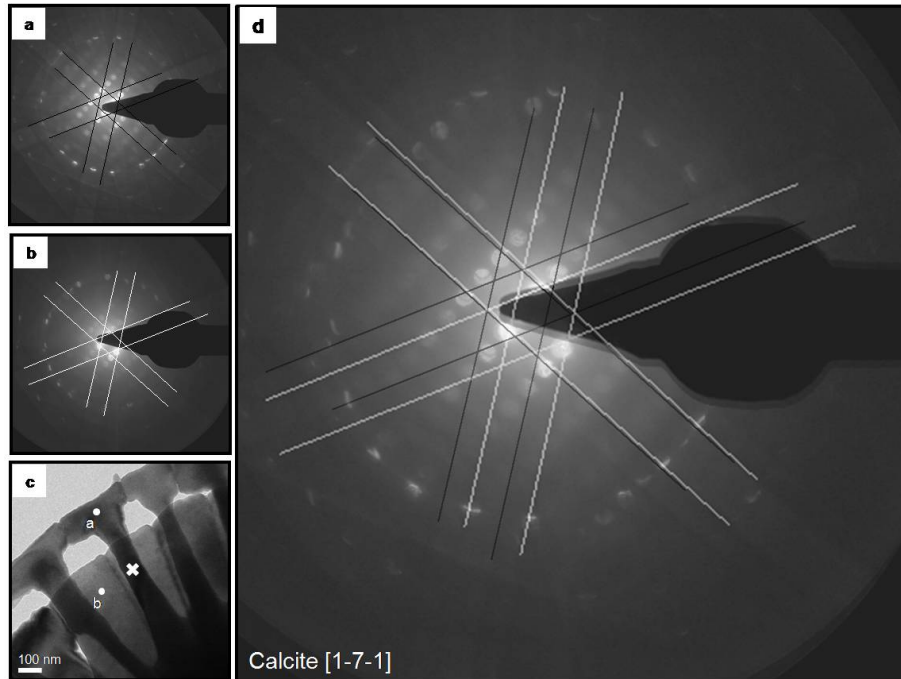


Figure 6.5 Nano probe diffraction of the distal- and the proximal shield element of *E. huxleyi*.
 a) Nano probe electron diffraction pattern of the distal shield element of *E. huxleyi* marked in the BF image given in c. The Kikuchi lines are marked by black lines.
 b) Nano probe diffraction pattern of the proximal shield element marked in the image given in c. The Kikuchi lines are marked by white lines.
 c) BF image of a plan-view sample with the position of the diffraction patterns a and b marked. The white dots mark the location where the nanoprobe electron diffraction patterns were taken and the white cross shows the area where the shift in the Kikuchi lines starts.
 d) Overlaid diffraction patterns of the distal and the proximal shield elements. The overlaid Kikuchi lines show a parallel translation for two pairs of Kikuchi lines. This is caused by tilting of $4^\circ \pm 1^\circ$ around the (101) plane normal.

We studied 7 distal- and proximal shield elements using 2 different plan-view samples. We took 21 nano probe diffraction patterns of the distal shield elements and 11 nano probe diffraction patterns of the proximal shield elements. Within the distal shield element we only used the area, where the proximal shield element did not contribute to the diffraction pattern. Figure 6.4 shows the results of one diffraction experiment in the distal shield element (Fig. 6.4f). The Kikuchi lines in the nano probe diffraction patterns 6.4a-d are marked by different colors. These

patterns were overlain (Fig. 6.4e) and the overlain Kikuchi lines of this area do not reveal tilting or rotation of the Kikuchi lines. An experimental uncertainty of 1° must be considered for this method [32]. Accordingly the tip of the distal shield element of *E. huxleyi* has a coherent single-crystal-like lattice, as no indication of misorientations or a mosaic like crystalline constitution within a precision of $\pm 1^\circ$ was found.

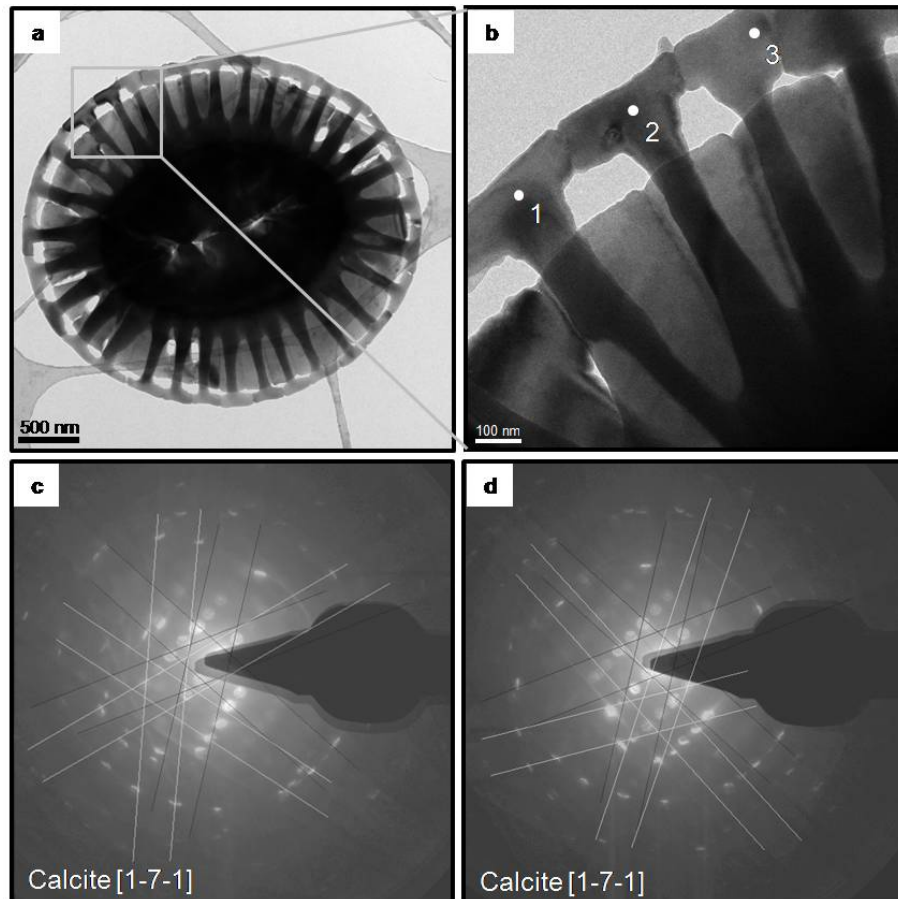


Figure 6.6 Diffraction experiments to determine the angle between different segments of *E. huxleyi*.

- BF image of *E. huxleyi*, with the position of the measurement marked by the grey square.
- BF image with the position of the nano probe diffraction pattern 1, 2 and 3 marked by white dots.
- Overlain diffraction patterns of position 1 (Kikuchi lines are marked in white) and 2 (Kikuchi pattern marked in black). The Kikuchi lines indicate a rotation of $8^\circ \pm 1^\circ$ between these segments around the direction normal to the coccolith ring.
- Overlain diffraction patterns of position 2 (Kikuchi lines are marked in black) and 3 (Kikuchi pattern marked in white). The Kikuchi lines indicate a rotation of $7^\circ \pm 1^\circ$ between these segments around the direction normal to the coccolith ring.

The same result was obtained for the outer rim of the proximal shield element. In order to investigate if the distal- and the proximal shield element together form one single-crystal

additional nano probe diffraction experiments with plan view samples were performed. As given in figure 6.5, we tilted the distal shield element to a zone axis (Fig. 6.5a) and, while keeping the goniometer angles constant, acquired a diffraction pattern of the proximal shield element (Fig. 6.5b). The positions where the diffraction patterns were taken are marked in the BF image in figure 6.5c. These diffraction patterns were overlain (Fig. 6.5d). Two out of three Kikuchi pairs were found to be shifted with respect to each other. Using the calibrated camera constant we calculated from these shifts a relative tilt angle [32] of $4^\circ \pm 1^\circ$ around the (1 0 1) plane normal direction. These observations are based on the investigation of 3 different pairs of distal- and proximal shield elements. Further investigations of the Kikuchi lines showed that these shifts start already within the middle of the distal shield element (white cross in Fig. 6.5c) with a tilt angle of approximately $1\text{-}2^\circ$.

We also investigated the change of lattice orientation between different coccolith segments (Fig. 6.6). The BF image in figure 6.6a shows the entire *E. huxleyi* coccolith with the area where we measured the rotation between three different segments marked by a grey square. The location of the diffraction patterns on the three segments are given in the BF image in figure 6.6b. In figure 6.6c the nano probe diffraction patterns of the distal shield elements of segment 1 and segment 2 are overlaid. Using the Kikuchi lines of both segments (white for segment 1 and black for segment 2), we found that the segments are rotated by $8^\circ \pm 1^\circ$ relative to each other around the direction normal to the coccolith ring. The same experiment was performed with the nano probe diffraction pattern of segment 2 (Kikuchi lines given in black) and segment 3 (Kikuchi lines given in white), where we obtained a rotation of $7^\circ \pm 1^\circ$ between the segments (Fig. 6.6d). This is in accordance to the value which we obtain geometrically from the elliptical shape of the coccolith.

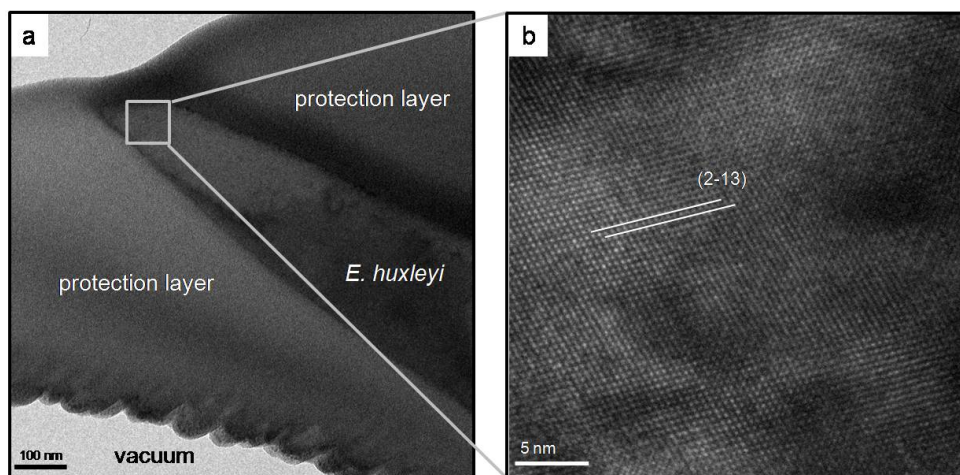


Figure 6.7 HR image of *E. huxleyi*.

- a) BF TEM image showing the area for HR imaging marked by the grey square. The protection layer is the carbon coating applied before FIB sectioning.
- b) The HRTEM image of the coccolith element contains no crystal boundaries. The differences in contrast are due to the bending of the element.

For detailed analyses of the coccolith segments such as distal shield-, proximal shield- and central area element HR imaging was performed. Within the elements, the HR images showed no evidence for a nano-mosaic or for intra-crystalline organic matrix. Figure 6.7b is an example of a HR image taken of an area of the distal shield element, which is indicated in the BF image shown in figure 6.7a.

6.4 Discussion

Investigations of coccoliths by TEM were done in previous studies [17, 18, 12, 33, 15], which applied different methods to prepare electron-transparent TEM samples. Several groups washed, centrifuged and dispersed the culture samples on TEM grids and finally used etching to obtain sufficiently thin samples [16, 17]. This sample preparation method could produce only plan-view TEM samples. Another preparation method was to sonicate the coccolith suspension for one minute and disperse this suspension on a TEM grid [18, 12, 33]. This method allowed to obtain plan-view and cross-section samples, which represented randomly-oriented cuts through coccolith segments. Wilbur and Watabe and Watabe used a preparation method to gain only cross-section samples: dried cultured samples were embedded in Vestopal H and cut with a diamond knife [16, 17]. However, the coccolith rings disintegrated such that the sample consisted of a random distribution of coccolith segments so that a well-defined cross-section could not be obtained. Our results show that the preparation method using FIB sectioning is able to produce site specific, oriented beam-transparent cross-sections through coccoliths.

Previous studies revealed that crystals of the V- unit could be found in very early growth stages in proto-coccolith rings [9]. These crystals were reported to have an average size of 30 to 60 nm [9]. Due to their size and the fact that they will be overgrown by R-crystals in later stages of development it was not possible to determine the crystallographic orientation of the V-units by light microscopy or electron diffraction [9] so far. With the target-preparation method we applied, we were able to detect the overgrown V-unit in fully grown coccolith segments of *E. huxleyi*. With the help of SAED and BF imaging in TEM we found the $[00\ 1]$ direction of the R-unit parallel and the $[0\ 1\ 0]$ direction perpendicular to the coccolith plane. The V-unit $[00\ 1]$ direction is perpendicular while the $[1\ \bar{1}\ 0]$ direction is parallel to the coccolith plane oriented. Our electron microscopy study thus confirms the V- and R-model of the c-axis orientation obtained by light microscopy of Young *et al.* for *E. huxleyi* and it complements the full crystallographic orientation [9]. Mann and Sparks described in their study that the crystallographic c-axis of the proximal shield element is parallel to the coccolith plane and the b-axis is perpendicular to the coccolith plane [18]. Our electron diffraction patterns taken from isolated shield elements confirmed the single-crystal nature and the absence of a mosaic spread for both the proximal-as well as the distal shield element of *E. huxleyi*. However, in 1988 the mosaic like assembly of biomaterial crystals was not known. So in this study the possibility that the coccolith calcite consists of a mosaic like assembly was considered during the diffraction experiments.

Modern high-resolution studies of carbonate materials constituting the shells, spines, and teeth of marine organisms such as brachiopods, sea urchins, corals and mollusks showed that their carbonate crystals have a mosaic like crystalline constitution [19, 20, 21, 34, 35, 26, 29]. Therefore we aimed to test if a mosaic-like crystalline structure is present in the calcite shell of *E. huxleyi*. Other studies [18] had used SAED, where the size of the illuminated area is determined by the SAED aperture typically 150 nm in diameter. In our study we performed experiments using nano probe electron diffraction and Kikuchi lines, where tilting angles $\geq 1^\circ$ can be detected at high spatial resolution of around 6 nm. This method revealed no misorientations within the tip of the distal- and proximal shield element of *E. huxleyi* but we found a clear shift of the Kikuchi lines starting from the middle of the distal shield element leading to a crystallographic misorientation of $4^\circ \pm 1^\circ$ around the (101) plane normal direction. This is necessary to obtain the spherical shape of the coccosphere. In principle, different scenarios can account for this. First, the upper and lower shield element might be separated by a small angle tilt grain boundary. In that case, we would expect an abrupt change in the orientation visible in a clearly resolvable shift of the Kikuchi lines. Experimentally, we do not observe an abrupt change but instead we measure a continuous change in orientation when taking nano probe diffraction pattern along the upper shield elements towards the central element. Second, the tilt could be obtained by geometrically necessary dislocations and we estimated that they should have a distance of around 7 nm to lead to an angle of 4° . These dislocations could be edge, screw or of mixed type. We did not observe strain fields associated with such dislocations; however, they could be invisible in the viewing directions used. Furthermore, the associated lattice distortion might be below the resolution limit of our microscope. A third possible explanation would be that the element is elastically bent due to a chemical gradient leading to a change in lattice parameters from top to bottom, due to stresses from the surrounding organic and/ or due support by the surrounding organic or due to gravitational forces. This would lead to a continuous orientation change. However, assuming a Young's modulus of 70 GPa [36] for the shield elements a stress (load per area) of around 4.6 GPa would be required to induce the 4° distortion mechanically. This essentially excludes mechanical stress as the origin of the misorientation, and since there is no evidence for a chemical gradient, dislocations seem to be the most likely explanation. A single coccolith is shaped like a flat domed bowl, which is necessary to create the spherical coccosphere by an assembly of these bowls. The relative misorientation between the proximal- and the distal shield elements of *E. huxleyi* serves to obtain the flat domed character of the coccoliths.

The different segments of the coccolith ring are also rotated with respect to each other around the normal of the coccolith ring, in order to form the circumference of the ellipsoidal ring. For the segments which we measured the angle is in the order of $7-8^\circ \pm 1^\circ$. These values fit nicely with results of former studies using Kikuchi lines in TEM [14]. In the study of Saruwatari *et al.* for each shield element one Kikuchi pattern was taken [14]. Furthermore, they did not use several electron patterns within one shield element to investigate orientation changes.

Multi-cellular calcifiers, for which a mosaic like crystalline constitution of the carbonate crystals has been demonstrated [19, 21, 37, 24, 23, 26, 27, 28] are formed in an extracellular process,

where vesicles containing amorphous calcium carbonate are exocytosed and attach to the carbonate shell, spines, or teeth, where they crystallize with a slight misorientation to form a crystal with a mosaic-spread [38]. In Contrast the whole coccolith ring is produced in a vesicle inside the cell [11]. So far our high-resolution imaging gave no evidence for organic layers within one crystal unit, nor of any nanomosaicity. If the tilt of 4° between the distal- and the proximal shield element is caused by a chemical gradient, gravitational forces and/or by support of the surrounding organic the coccoliths would differ from the multi-cellular marine calcifiers.

6.5 Conclusion

In this study it has been shown that FIB sectioning of coccoliths can be used to gain pristine site specific cross-sections of the coccoliths of *E. huxleyi*. The described methods allowed to image and analyze the orientation of the overgrown V-unit. The analysis revealed that the $[110]$ direction of the V-unit is in tangential direction of the coccolith ring and the $[1\bar{1}0]$ direction is radial with respect to the coccolith ring.

Our nanoprobe electron diffraction experiments with a precision of 1° reveal that the distal- and the proximal element of the R-unit show a relative tilt of $4^\circ \pm 1^\circ$ around the (101) plane normal direction. This misorientation starts already within the middle of the distal shield element. This tilt within and between the shield elements serves to obtain the flat domed character of the coccoliths, which is necessary to form a coccosphere. The HRTEM images do not show evidence of a mosaic like assembly of the calcite crystals of the shield elements that build up the coccoliths of *E. huxleyi*.

For the future applying the techniques developed here to other coccoliths has great potential to elucidate the structure of coccolith species which are too small to study with optical microscopy and SEM. Hence we are confident that these techniques can significantly advance our knowledge of the range biomineralisation patterns in coccoliths and the degree to which variation in such patterns is responsible for the extraordinary diversity in coccolith forms.

6.6 Bibliography

- [1] HONJO, S. Coccoliths: production, transportation and sedimentation. *Marine Micropaleontology* **1** (1976), 65–79.
- [2] WINTER, A., AND SIESSER, G. W., Eds. *Coccolithophores*. University Press, Cambridge, 1994.
- [3] YOUNG, J. R., BERGEN, J. A., BOWN, P. R., BURNETT, J. A., FIORENTINO, A., JORDAN, R. W., KLEIJNE, A., VAN NIEL, B. E., ROMEIN, A. J. T., AND VON SALTS, K. Guidelines for coccolith and calcareous nannofossil terminology. *Palaeontology* **40**, 4 (1997), 875–912.

- [4] YOUNG, J. R., GEISEN, M., CROS, L., KLEIJNE, A., SPRENGEL, C., PROBERT, I., AND ÖSTERGAARD, J. A guide to extant coccolithophore taxonomy. *Journal of Nannoplankton Research. Special Issue 1* (2003), 1–132.
- [5] RILEY, J., CHESTER, J. P., AND CHESTER, R., Eds. *Treatise on chemical oceanography*. Academic Press, London, 1976.
- [6] STANLEY, S. M. *Earth system history*. W.H. Freeman and Company, New York, 1999.
- [7] MCINTYRE, A. Coccoliths as paleoclimatic indicators of Pleistocene glaciation. *Science* **158** (1967), 1314–1317.
- [8] SATO, T., KAMEO, K., AND TAKAYAMA, T. Coccolith biostratigraphy of the Arabian Sea. *Proceedings of the Ocean Drilling Program - Scientific Results* **117** (1991), 37–54.
- [9] YOUNG, J. R., DIDYMUS, J. M., BOWN, P. R., PRINS, B., AND MANN, S. Crystal assembly and phylogenetic evolution in heterococcoliths. *Nature* **356** (1992), 516–518.
- [10] YOUNG, J. R., DAVIS, S. A., BOWN, P. R., AND MANN, S. Coccolith ultrastructure and biomineralisation. *Journal of Structural Biology* **126**, 3 (1999), 195–215.
- [11] YOUNG, J. R., AND HENRIKSEN, K. Biomineralization within vesicles: The calcite of coccoliths. *Reviews in Mineralogy and Geochemistry* **54** (2003), 189–215.
- [12] DIDYMUS, J. M., YOUNG, J. R., AND MANN, S. Construction and morphogenesis of the chiral ultrastructure of coccoliths from the marine alga *Emiliana huxleyi*. *Proceedings of the Royal Society London B: Biological Sciences* **258** (1994), 237–245.
- [13] SARUWATARI, K., OZAKI, N., NAGASAWA, H., AND KOGURE, T. Crystallographic alignments in a coccolith (*Pleurochrysis carterae*) revealed by electron back-scattered diffraction (EBSD). *American Mineralogist* **91**, 11-12 (2006), 1937–1940.
- [14] SARUWATARI, K., OZAKI, N., NAGASAWA, H., AND KOGURE, T. Comparison of crystallographic orientations between living (*Emiliana huxleyi* and *Gephyrocapsa oceanica*) and fossil (*Watznaueria barnesiae*) coccoliths using electron microscopes. *American Mineralogist* **93** (2008), 1670–1677.
- [15] SARUWATARI, K., AKAI, J., FUKUMORI, Y., OZAKI, N., NAGASAWA, H., AND KOGURE, T. Crystal orientation analyses of biominerals using Kikuchi patterns in TEM. *Journal of Mineralogical and Petrological Sciences* **103** (2008), 16–22.
- [16] WILBUR, K. M., AND WATABE, N. Experimental studies on calcification in molluscs and the alga *Coccolithus huxleyi*. *Annals of the New York Academy of Sciences* **109** (1963), 82–112.

-
- [17] WATABE, N. Crystallographic analysis of the coccolith of *Coccolithus huxleyi*. *Calcified Tissue Research* **1** (1967), 114–21.
- [18] MANN, S., AND SPARKS, N. H. C. Single crystalline nature of coccolith elements of the marine alga *Emiliania huxleyi* as determined by electron diffraction and high-resolution Transmission. *Proceedings of the Royal Society B: Biological Sciences* **234** (1988), 441–453.
- [19] NEFF, J. M. Ultrastructure of the outer epithelium of the mantle in the clam *Mercenaria mercenaria* in relation to calcification of the shell. *Tissue & Cell* **4**, 4 (1972), 591–600.
- [20] FENG, Q. L., CUI, F. Z., PU, G., WANG, R. Z., AND LI, H. D. Crystal orientation, toughening mechanisms and a mimic of nacre. *Materials Science and Engineering: C* **11** (2000), 19–25.
- [21] WEISS, I. M., TUROSS, N., ADDADI, L., AND WEINER, S. Mollusc larval shell formation: amorphous calcium carbonate is a precursor phase for aragonite. *The Journal of Experimental Zoology* **293** (2002), 478–91.
- [22] ROUSSEAU, M., LOPEZ, E., STEMPFLÉ, P., BRENDLÉ, M., FRANKE, L., GUETTE, A., NASLAIN, R., AND BOURRAT, X. Multiscale structure of sheet nacre. *Biomaterials* **26**, 31 (2005), 6254–62.
- [23] GRIESSHABER, E., SCHMAHL, W. W., NEUSER, R., PETTKE, T., BLUM, M., MUTTERLOSE, J., AND BRAND, U. Crystallographic texture and microstructure of terebratulide brachiopod shell calcite: An optimized materials design with hierarchical architecture. *American Mineralogist* **92** (2007), 722–734.
- [24] JACOB, D. E., SOLDATI, A. L., WIRTH, R., HUTH, J., WEHRMEISTER, U., AND HOFMEISTER, W. Nanostructure, composition and mechanisms of bivalve shell growth. *Geochimica et Cosmochimica Acta* **72** (2008), 5401–5415.
- [25] GOETZ, A. J., GRIESSHABER, E., NEUSER, R. D., LÜTER, C., HÜHNER, M., HARPER, E., AND SCHMAHL, W. W. Calcite morphology, texture and hardness in the distinct layers of rhynchonelliform brachiopod shells. *European Journal of Mineralogy* **21**, 2 (2009), 303–315.
- [26] BENZERARA, K., MENGUY, N., OBST, M., STOLARSKI, J., MAZUR, M., TYLISZAK, T., BROWN, G. E., AND MEIBOM, A. Study of the crystallographic architecture of corals at the nanoscale by scanning transmission X-ray microscopy and transmission electron microscopy. *Ultramicroscopy* **111**, 8 (2011), 1268–75.
- [27] ADDADI, L., VIDAUSKY, N., AND WEINER, S. Transient precursor amorphous phases in biomineralization. In the footsteps of Heinz A. Lowenstam. *Zeitschrift für Kristallographie - Crystalline Materials* **227** (2012), 711–717.

- [28] SCHMAHL, W. W., GRIESSHABER, E., KELM, K., BALL, A., GOETZ, A., XU, D., KREITMEIER, L., AND JORDAN, G. Towards systematics of calcite biocrystals: insight from the inside. *Zeitschrift für Kristallographie - Crystalline Materials* **227** (2012), 604–611.
- [29] SETO, J., MA, Y., DAVIS, S. A., MELDRUM, F., GOURRIER, A., KIM, Y.-Y., SCHILDE, U., SZTUCKI, M., BRUGHAMMER, M., MALTSEV, S., JÄGER, C., AND CÖLFEN, M. Structure-property relationships of a biological mesocrystal in the adult sea urchin spine. *Proceedings of the National Academy of Sciences* **109**, 18 (2012), 7126–7126.
- [30] SONG, R.-Q., AND CÖLFEN, H. Mesocrystals–ordered nanoparticle superstructures. *Advanced Materials* **21** (2010), 1–30.
- [31] MAYER, J., GIANNUZZI, L. A., KAMINO, T., AND MICHAEL, J. TEM sample preparation and FIB-induced damage. *MRS Bulletin* **32** (2007), 400–407.
- [32] WILLIAMS, D. R., AND CARTER, B. C. *Transmission electron microscopy a textbook for material sciences*, 2 ed. Springer-Verlag, New York, 2009.
- [33] DAVIS, S. A., YOUNG, J. R., AND MANN, S. Electron microscopy studies of shield elements of *Emiliania huxleyi* coccoliths. *Botanica Marina* **38** (1995), 493–497.
- [34] SCHMAHL, W. W., GRIESSHABER, E., MERKEL, C., KELM, K., DEUSCHLE, J., NEUSER, R. D., GÖTZ, A. J., SEHRBROCK, A., AND MADER, W. Hierarchical fibre composite structure and micromechanical properties of phosphatic and calcitic brachiopod shell biomaterials An overview. *Mineralogical Magazine* **72**, 2 (2008), 541–562.
- [35] VIELZEUF, D., FLOQUET, N., CHATAIN, D., BONNETE, F., FERRY, D., GARRABOU, J., AND STOLPER, E. M. Multilevel modular mesocrystalline organization in red coral. *American Mineralogist* **95** (2010), 242–248.
- [36] MERKEL, C., DEUSCHLE, J., GRIESSHABER, E., ENDERS, S., STEINHAUSER, E., HOCHLEITNER, R., BRAND, U., AND SCHMAHL, W. W. Mechanical properties of modern calcite- (*Mergerlia truncata*) and phosphate-shelled brachiopods (*Discradisca stella* and *Lingula anatina*) determined by nanoindentation. *Journal of Structural Biology* **168**, 3 (2009), 396–408.
- [37] AIZENBERG, J., WEAVER, J. C., THANAWALA, M. S., SUNDAR, V. C., MORSE, D. E., AND FRATZL, P. Skeleton of *Euplectella* sp.: structural hierarchy from the nanoscale to the macroscale. *Science* **309** (2005), 275–278.
- [38] BENIASH, E., AIZENBERG, J., ADDADI, L., AND WEINER, S. Amorphous calcium carbonate transforms into calcite during sea urchin larval spicule growth. *Proceedings of the Royal Society B: Biological Sciences* **264** (1997), 461–465.

7 TEM preparation methods and their influence on radiation damage on the beam sensitive CaCO₃ shell of *Emiliana huxleyi*

This chapter is based on the following publication:

Hoffmann R., Wochnik A. S., Betzler S. B., Matich S., Griesshaber E., Schmahl W. W. and Scheu C. (2014): *Micron* **62** 28-36

7.1 Introduction

Since the industrial revolution 250 years ago the atmospheric carbon dioxide level increased by nearly 40% [1]. This trend is predicted to continue, and by the end of the century CO₂ levels might exceed 800 ppm [2]. The current atmospheric CO₂ rate is driven by the use of fossil fuel and deforestation, which is known as the anthropogenic CO₂ rate [3]. This is very different to the changes in the past, since temperatures are rising at a much greater rate [4]. The rising CO₂ level is slowed down by the global oceans, which absorb a significant amount of the CO₂ including one-third of the anthropogenic CO₂ emission [3]. But the CO₂ absorption of the ocean has its consequences as it lowers the pH value of the ocean water body and leads to alterations in fundamental chemical balances, known as ocean acidification [5]. Marine organisms which build calcium carbonate shells like corals, mollusks, echinoderms, foraminifera and coccolithophores will be directly influenced by ocean acidification [5]. Laboratory experiments show that many calcifying species reduce calcification and growth rates under high-CO₂ conditions [5]. However, the potential of marine organisms to adapt to the increasing CO₂ level under natural long term conditions is not well known yet [5, 6]. To investigate the potential of marine organisms with CaCO₃ shells for CO₂ storage, the understanding of the ultrastructure and the crystallographic assembly is very important. Therefore high resolving methods like TEM and related techniques like HR imaging, electron diffraction and EELS are necessary. The TEM studies require very thin electron transparent samples. In this regard the sensitivity of the material must be considered during the sample preparation. Different types of electron interaction can lead to different kinds of radiation damage in the TEM [7, 8]. Atomic displacement (knock-on damage) and electron-

beam sputtering of atoms from the surface often occur due to (quasi) elastic scattering, which at the same time gives rise to electron-diffraction patterns and phase contrast images [7, 8]. In addition, inelastic scattering, which is used for EELS, can lead to radiolysis effects (breaking atomic bonds and thus changing the structure of a specimen) or remove material, which leads to mass loss and to hydrocarbon contamination [7, 8].

CaCO₃, which is investigated in this study, is very sensitive to electron bombardment, mechanical load and thermal treatment. Several studies already revealed that the single-crystalline calcite will transform to poly-crystalline lime during illumination with an electron beam [9, 10, 11]. Therefore, several precautions have to be considered during sample preparation and structural investigations of CaCO₃ shells, which protect living organisms for example, the coccolithophores.

Since coccolithophores live in almost all marine habitats [12] and are one of the most important primary producers in the oceans [13], they are of high interest for CO₂ studies. These small organisms are formed in a vesicle inside the cell and show a radial structure, which is characteristically formed by two alternating types of crystal units [14]. These are the V-unit with a sub-vertical crystallographic c-axis and the R-unit with a sub-radial c-axis [14]. The TEM sample preparation for coccolithophores is in particular demanding since their skeletal elements possess sizes smaller than 10 μm as visible in the SEM image in figure 7.1.

In this work we studied the abundant coccolithophore *E. huxleyi*. This species was already investigated with high spatial resolution methods such as SEM and TEM and its analytical techniques by several groups [15, 16, 17, 18] but still open questions remain concerning e.g. influence of the CO₂ content on the assembly. Very thin samples should be prepared and the sensitivity of the material should be considered during the sample preparation. Different methods were used in literature to obtain TEM samples. Culture samples were washed, centrifuged and dispersed on TEM grids and finally etched with 0.1 M HCl for 5 min [19, 15]. This sample preparation method allowed producing only plan-view TEM samples. Another preparation method which was applied is to sonicate the coccolith suspension for one minute and disperse this suspension on a TEM grid [16, 20, 17]. This method allowed obtaining plan-view and cross-section samples, which represented randomly-oriented cuts through coccolith segments. Watabe and Wilbur and Watabe used a preparation method to gain only cross-section samples [19, 15]. They dried cultured samples embedded in Vestopal H (a copolymer between a polyester of maleic and fumaric acids, esterified with di- and tri- hydroxyalcohols and styrene) and cut them with a diamond knife. However, the coccolith rings disintegrated such that the sample consisted of a random distribution of coccolith segments and a well defined cross-section could not be obtained.

In this study preparation techniques for TEM plan-view and cross-section samples were investigated and adjusted for the sensitive CaCO₃ shell of *E. huxleyi*. Furthermore the electron beam sensitivity of the coccolith calcite was compared to the sensitivity of geological single calcite crystals (Iceland spar). This was done for all preparation methods. The experiments were done by TEM and associated analytical techniques including SAED experiments, EELS, BF- and HRTEM imaging. These investigations serve as a pre-requisite for further studies of *E. huxleyi* which concentrate on the pH-value dependence of the coccoliths and on the amount

and distribution of trace elements within the calcite.

7.2 Materials and methods

7.2.1 Samples

Two different Plankton sample series from the Atlantic Ocean were used during this study. The first sample series provided by M. Kučera and H. Schulz is stemming from the North Atlantic (POS 334, stat. 4 MSN K7). The material derives from five different water depth intervals: 0-100 m, 100-200 m, 200-300 m, 300-500 m and 500-700 m. The second series was provided by J. Young and was collected from the South Atlantic (PMT 18, CTD 89). This series contained samples from three different water depths: 0 m, 48 m and 96 m.

To avoid bacterial growth and to buffer the carbonate system the samples were preserved with formalin and hexamine after the collection. They were sieved to reduce the particles to a size smaller than 20 μm . The South Atlantic samples were filtered with a vacuum pump onto a Millipore polycarbonate membrane filter (diameter: 47 mm, pore size: 0.45 μm).

7.2.2 Instrumentation

For SEM imaging and FIB sectioning a Zeiss NVision40 FIB microscope was used, which combines the technologies of a GEMINI electron column with a focused ion beam (zeta FIB column - operated at 30 kV) and a single-injector multi-channel GIS needle. Secondary electron images were acquired at a low acceleration voltage of 2.5 kV.

For TEM investigations we used a FEI Titan 80-300 kV field emission (S)/TEM equipped with an energy-dispersive X-ray spectrometer and a Gatan Tridiem imaging filter. The measurements were performed at 300 kV.

The analytical and imaging methods used in this study were SAED experiments, EELS, BF- and HR imaging. For the SAED an aperture of 160 nm diameter was used. The full width at half maximum (FWHM) of the zero loss peak (ZLP) was around 0.9 – 1.2 eV for the EELS measurements. energy loss near edge structure (ELNES) analysis was done in diffraction mode with a dispersion of 0.3 eV/channel. A 2 mm spectrometer entrance aperture and a camera length of 130 mm were used resulting in a collection semi-angle of 13.5 mrad. Channel-to-channel gain variation and dark current correction was done for all EEL spectra. For background subtraction a power-law fitting procedure was used [21]. All EELS data were acquired in locations where no carbon film was present.

7.3 Results

7.3.1 Preparation methods

In this study two different kinds of materials were investigated, on the one hand biological built calcite and on the other hand calcite geologically formed (Iceland spar). To investigate biologically formed calcite the coccolithophore species *E. huxleyi* was used. The general assembly of these marine organisms is indicated in figure 7.1 which shows a SEM image of a complete coccosphere with a single coccolith platelet zoomed in.

Plan-view samples of *E. huxleyi* and the Iceland spar crystal should be prepared as gently as possible. Therefore we modified the preparation method developed by Wilbur and Watabe and Watabe [19, 15]. They used 0.1 M HCl for 5 min to thin the sample, which was dropped on a copper TEM grid, while we applied dH₂O for the thinning procedure as described in detail below. To prepare coccolith plan-view samples the 200-300 m and the 300-500 m sample of the North Atlantic series were used. For the preparation of TEM samples the coccolith concentration had to be increased, while the salt concentration needed to be reduced. In this regard two different preparation methods were applied. One method used dialysis in dH₂O for 48 h to reduce the salt concentration followed by centrifugation (3000 rpm, 5 min) to increase the particle concentration. The second method was based on filtration. By using a Nuclepore polycarbonate membrane filter (diameter: 47 mm, pore size: 0.8 μm) the samples were dispersed. After the filter was dried the sample was removed with a spatula and dissolved in ethanol.

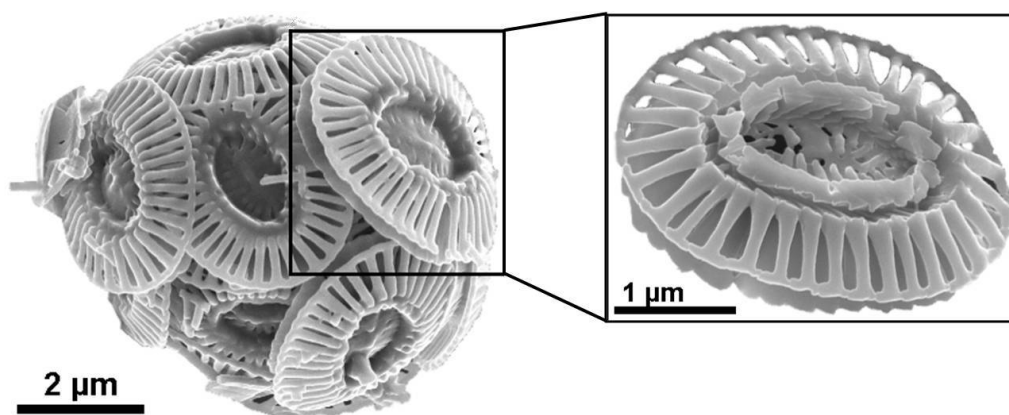


Figure 7.1 SEM image of a complete coccosphere of *E. huxleyi*. The zoomed in area shows a SEM image of a single coccolith.

The plan-view samples were prepared by dropping the samples on a copper TEM finder grid coated with a holey carbon film. This allowed determining the position of a well preserved coccolith of *E. huxleyi* in the SEM, which was then studied in detail in the TEM. To gain the requested sample thickness the TEM grids were etched by floating coated side down in dH₂O for several hours. This has the advantage of being gentler than the HCl treatment. The thinning time has to be adjusted for each species. For *E. huxleyi* a thinning time of 30 h was found to

be adequate and resulted in a thickness between 60 nm and 90 nm.

For the Iceland spar plan-view samples the crystals were pulverized first using a mortar. Afterwards the powder was kept in bi dH₂O for 26 h and then dropped on a TEM copper grid with a lacey carbon film. These samples were dried and could be used immediately without further etching. To avoid contamination problems these samples were plasma cleaned for 20 s directly before the TEM investigations.

For the coccolith cross-section preparation the 0-100 m and 100-200 m sample from the North Atlantic and the three samples from the South Atlantic series were used. To remove the salt and to enhance the coccolith concentration the North Atlantic samples were dialyzed and centrifuged as described above for the preparation of the plan-view samples. Afterwards the samples were dropped onto a Si-Wafer. The south Atlantic samples were used directly for the cross-section preparation. This allows us to compare whether the thinning/dialysis in dH₂O causes demineralization.

To obtain cross-sectional TEM samples, conventional preparation methods were not successful and therefore the target prepared TEM samples were obtained by FIB sectioning. It is known that radiation damage under ion bombardment can easily occur [22]. In order to protect the sensitive sample material a carbon layer of a total thickness of around 1 μm was deposited on the sample surface. Firstly, an approximately 50 nm thin carbon layer was deposited by EBID at 2.5 kV, using the high current mode and an 120 μm aperture for a total of 15 min. Secondly, the thicker protection layer was deposited on top of that for 5 min via IBID, using a beam current of 300 pA at 30 kV. In this study carbon was used instead of platinum, since it turned out that platinum affected adversely the sample's behavior because it deeply penetrated into the sample. The sectioning with Ga⁺-ions was done at a working distance of 4.9 mm while the stage was tilted at 54°. A lamella of a size of 2 μm x 20 μm x 5 μm was cut from the coccolith and transferred to a lift out copper grid by a manipulator needle. Carbon was used to fix the lamella onto the grid. The final polishing of the lamella was done with 40 pA at 30 kV from both sides of the lamella until the lamella had a final thickness of around 70 nm.

To prepare a crosssection of the Iceland spar crystals the sample was pulverized first and then dissolved in ethanol. Afterwards the sample was dropped on a Si-Wafer and dried. A thin carbon film using a BAL-TEC coating system was deposited on the samples, which were then FIB sectioned as described above for the coccoliths. The final sample thickness was around 70 nm as well.

7.3.2 Material transformation

In the present work, besides investigating suitable sample preparation techniques, we were also interested in the material stability under electron beam bombardment using 300 kV electrons. For the assessment of damage we used changes in the diffraction pattern, formation of randomly oriented nano-crystals (nanomosaic) and changes in the low-loss and core-loss EELS data. The accumulated electron dose was calculated from the beam current, the size of the illuminated area

and the time after the irradiation had started [21, 8]. Images and EELS data obtained with the maximum tolerable dose, above which the first visible material transformation occurred, are shown. To illustrate the effect of damage and associated material change, we also present images and data with clearly visible changes taken after long acquisition times and a high accumulated dose exceeding the tolerable value by several magnitudes. A detailed time dependent damage study was beyond the scope of the present work.

The intention to use 300 kV was motivated by the fact that a higher spatial resolution can be achieved compared to 80 kV measurements and that radiolysis is expected to be lower [8]. In a very recent study, we have successfully performed nanoprobe electron diffraction investigations at 80 kV on coccoliths to determine their crystallographic assembly [23], however, the quality of the HR images was low. Thus it will be beneficial for future studies e.g. to detect defect structures in the coccoliths, if we can demonstrate the successful use of 300 kV electrons.

The TEM measurements of the coccolith plan-view samples have been performed on four different samples. Figure 7.2a exemplary shows a BF TEM image of a plan-view sample at higher magnification segments before beam damage occurred and the material transformed. Selected area electron diffraction pattern of the undamaged samples revealed that the coccoliths consist of single-crystalline calcite (Fig. 7.2b). Corresponding HRTEM images confirmed that the untransformed material is single-crystalline (Fig. 7.2c). The maximum tolerable dose above which damage was observed was 10^5 e/nm². As Figure 7.2d reveals the material clearly changes. The diffraction patterns taken after 5 min exposure time corresponding to a accumulated dose of 3×10^7 e/nm² show a transformation from single-crystalline calcite into a poly-crystalline material (Fig. 7.2e). This can be also seen in the HRTEM micrographs like in Figure 7.2f. The analysis of the SAED patterns exhibits the d-spacings of the transformed material. The values indicate the formation of poly-crystalline calcium oxide, lime. In principle, considering an error of 3% of the determined d-values the transformed material could be assigned to poly-crystalline aragonite (a CaCO₃ modification) as well, even this is very unlikely since calcite is thermodynamically much more stable than aragonite. Nevertheless, using electron diffraction only, it cannot be excluded.

The beam damage experiments were done at two different coccolith cross-section samples. In Figure 7.3a an exemplary BF TEM image of an *E. huxleyi* segment prepared by FIB sectioning without prior beam damage is given. The SAED pattern of undamaged areas of the sample, as exemplary shown in Figure 7.3b reveal d-spacings that indicate single-crystalline calcite. Also the HRTEM images (Fig. 7.3c) of the undamaged sample confirm that the sample is single-crystalline. In Figure 7.3d the BF image of the same sample as in figure 7.3a after an exposure to a dose of $\sim 3 \times 10^7$ e/nm² of electron beam bombardment is given. Obviously, beam damage occurred and the corresponding diffraction patterns (Fig. 7.3e) reveal a transformation from a single into a poly-crystalline material. This can be confirmed by HRTEM imaging as figure 7.3f shows exemplary. For the plan-view coccolith samples the analysis of the poly-crystalline diffraction pattern indicates that the transformed material is lime or aragonite.

Similar measurements as described for the *E. huxleyi* coccolith plan-view and cross-section

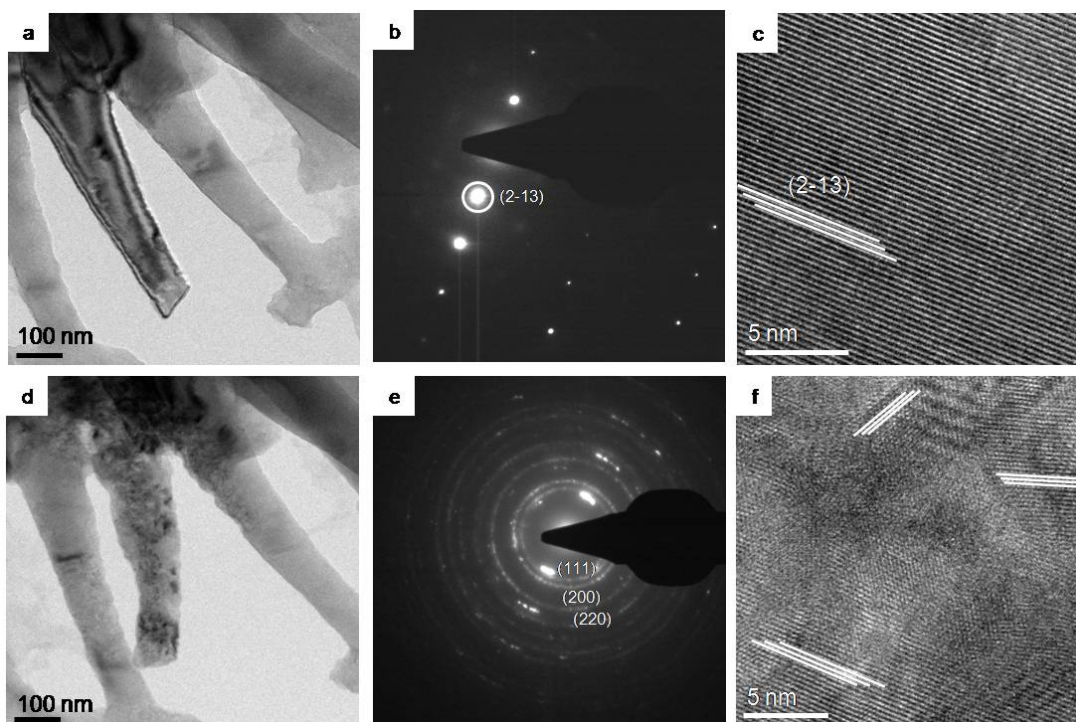


Figure 7.2 TEM investigations of a representative plan-view sample recording the beam sensitivity of the material at an acceleration voltage of 300 kV.

a) BF image of an *E. huxleyi* coccolith plan-view sample (North Atlantic 200-300 m) before beam damage occurs.

b) Selected area electron diffraction pattern of an undamaged area of the coccolith indicating single-crystalline calcite.

c) An area of the coccolith without beam damage is shown in this HRTEM image. It is indicating that the material is single-crystalline. The white lines highlight the position of the $(2\bar{1}3)$ lattice plane. The accumulated dose was $\sim 10^5$ e/nm².

d) BF image of an *E. huxleyi* coccolith plan-view sample after 5 min under electron beam bombardment.

e) The transformation of the coccolith calcite can be seen in this selected area electron diffraction pattern. The transformation of crystalline calcite to a poly-crystalline material after 5 min under electron beam bombardment is given here. The accumulated dose was $\sim 3 \times 10^7$ e/nm². Since the diffraction patterns d-spacings show a smaller error for lime the hkl- values for lime are given here.

f) HRTEM image showing an area of the coccolith after 5 min of beam bombardment. It is indicating that the material is transformed from a single-crystalline to a poly-crystalline material. To illustrate the transformation different lattice plane distances are highlighted by white lines.

samples were performed with mineralogical single-crystalline calcite (Iceland spar). These experiments were used to verify if calcite from geological and biological sources behave differently under electron beam bombardment.

For the beam damage experiments four different plan-view samples were investigated. The results of these studies are exemplarily shown in figure 7.4. A BF image of an undamaged area

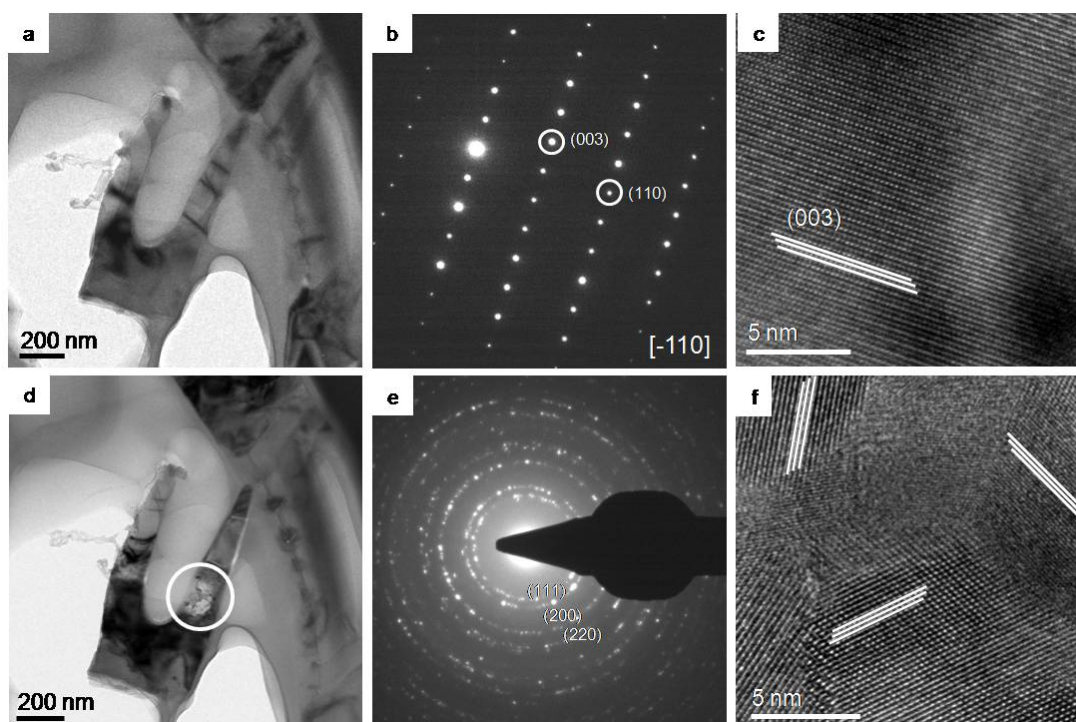


Figure 7.3 The analysis of a cross-section coccolith sample recording the beam sensitivity of the material by TEM. The measurements were done at an acceleration voltage of 300 kV.

a) This BF image illustrates how an *E. huxleyi* coccolith cross-section sample appears before beam damage occurs (South Atlantic 48 m).

b) A SAED pattern of an undamaged area of the coccolith is given. The analysis of the d-spacings indicate single-crystalline calcite in the $[\bar{1}10]$ zone axis.

c) HRTEM image taken at an area of the coccolith without beam damage. It is indicating that the material is single-crystalline and the position of the (003) lattice plane is marked.

d) The *E. huxleyi* coccolith cross-section sample after 2 min under electron beam bombardment is shown in this BF image. The damaged area is marked by the white circle.

e) Selected area electron diffraction pattern of a damaged area of the coccolith indicating the transformation of crystalline calcite to a poly-crystalline material after 2 min under electron beam bombardment corresponding to an accumulated dose of $\sim 10^7$ e/nm². The hkl values for lime are given here, since the diffraction patterns d-spacings show a smaller error for lime.

f) An area of the coccolith after 2 min of beam bombardment is shown in this HRTEM image. This result reveals that the material is transforming from a single-crystalline to a poly-crystalline material. The white lines highlight the different lattice plane distances.

of the single calcite crystal is given in figure 7.4a. The corresponding diffraction pattern given in figure 7.4b indicates single-crystalline calcite in the $[\bar{1}11]$ zone axis. The HRTEM image given in figure 7.4c confirms that the sample material is single-crystalline. The Iceland spar plan-view samples changed under electron beam bombardment, as clearly shown in figure 7.4d.

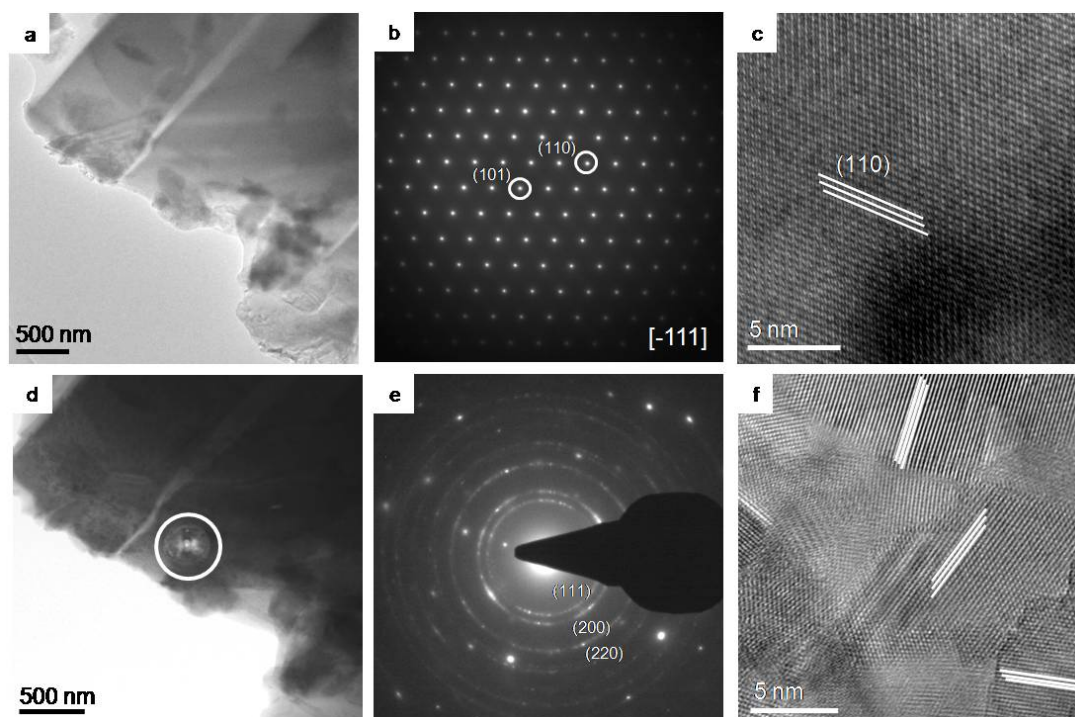


Figure 7.4 The beam sensitivity of the Iceland spar plan-view sample investigated by TEM at an acceleration voltage of 300 kV.

- The calcite sample before beam damage occurs is shown in this BF image.
- The SAED pattern of an undamaged area of the calcite single-crystal is acquired in the $[\bar{1}11]$ zone axis.
- The single-crystalline character of the material is also shown in this HRTEM image of an untransformed sample. The (110) lattice plane is highlighted by the white lines.
- A BF image of the Iceland spar crystal after electron beam bombardment corresponding to an accumulated dose of $\sim 10^7$ e/nm² is given here. The beam damage area is marked by the white circle.
- The SAED pattern of the damaged area of the crystal shows the material transformation. The single-crystalline calcite transforms to a poly-crystalline material, which can be indicated as lime by the d-spacings. The hkl values are given in the image. It is worth to mention that considering an error of 3 % the d-spacings could indicate aragonite as well.
- In the HRTEM image the crystal after less than 2 min of beam bombardment is shown. It confirms the transformation of the crystal from a single-crystal into a poly-crystal. The transformation is illustrated by the different lattice plane distances, which are highlighted by white lines.

The diffraction pattern (Fig. 7.4e) taken in that area reveals a transformation from single-crystalline calcite into a disordered poly-crystalline material. In the corresponding HRTEM image (Fig. 7.4f) this transformation is also clearly visible. The d-spacings of the transformed material were analyzed and revealed that the calcite transforms also into lime or aragonite under electron beam bombardment.

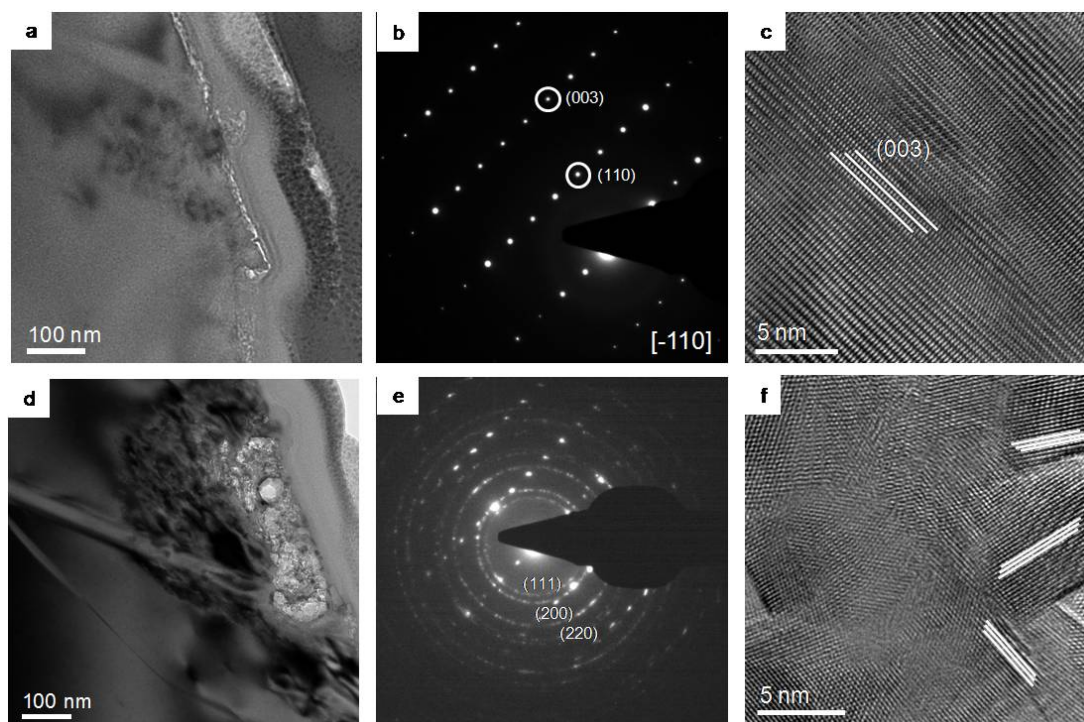


Figure 7.5 TEM investigations of the Iceland spar cross-section samples done at an acceleration voltage of 300 kV to record the beam sensitivity of the material.

- a) This BF image shows an untransformed Iceland spar cross-section sample.
- b) The SAED pattern of the undamaged sample reveals a single calcite crystal in the $[\bar{1}10]$ zone axis.
- c) The corresponding HRTEM image is showing an area of the Island spar without beam damage. The lattice planes confirm that the material is single-crystalline and the position of the (003) lattice plane is highlighted by white lines.
- d) The crystal after 5 min under electron beam bombardment corresponding to an accumulated dose of $\sim 3 \times 10^7$ e/nm² can be seen in this BF image. The damaged area is clearly visible.
- e) Selected area electron diffraction pattern of a transformed area of the calcite crystal. Here the transformation of single-crystalline calcite to a poly-crystalline material can be seen. Since the diffraction patterns d-spacings show a smaller error for lime the hkl values for lime are given here.
- f) After 5 min of beam bombardment the sample clearly changed, which can be revealed in the HRTEM image. It confirms the transformation from single-crystalline calcite to a poly-crystalline material. To illustrate this transformation different lattice plane distances are highlighted by white lines.

The beam stability of the Iceland spar FIB prepared sample was investigated as well. Therefore TEM measurements at different areas of one cross-section sample were performed. Figure 7.5a shows an exemplary BF TEM image of an Iceland spar cross-section without beam damage. In the SAED pattern of the undamaged area the material could be identified as single-crystalline calcite in the $[\bar{1}10]$ zone axis (Fig. 7.5b). This was confirmed by HRTEM imaging of the undamaged sample as shown in figure 7.5c.

An example of a cross-section sample after 5 min of electron beam bombardment corresponding to an accumulated dose of $\sim 3 \times 10^7$ e/nm² is given in figure 7.5d. The area where the beam damage occurred and the material changed can clearly be seen. The corresponding diffraction pattern (Fig. 7.5e) of this area shows the transformation from a single-crystal into a poly-crystal. The HRTEM image taken in this area (Fig. 7.5f) confirms that the material is becoming poly-crystalline. As for the coccolith and the Iceland spar plan-view samples the analysis of the diffraction pattern revealed that the material also transformed into poly-crystalline lime or aragonite.

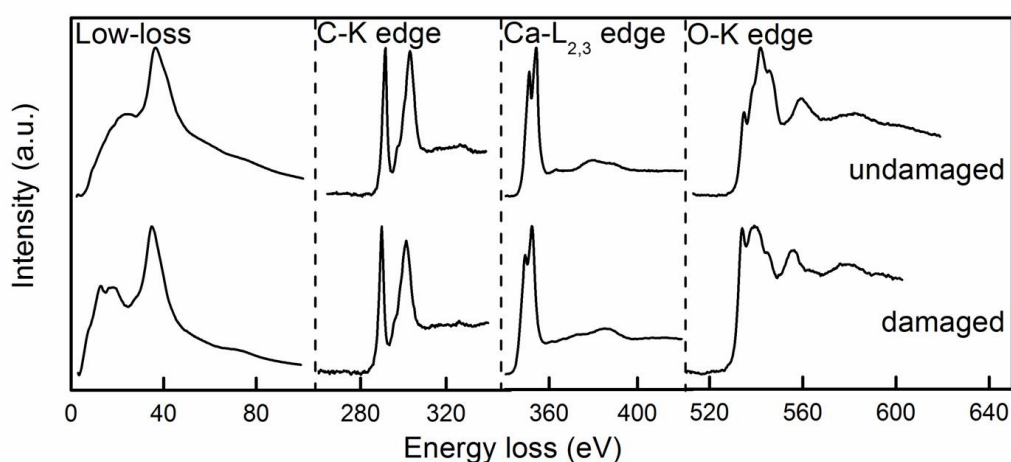


Figure 7.6 EELS measurements acquired in diffraction mode of plan-view coccolith samples showing the low-loss region, the carbon K-edge, the calcium L_{2,3}-edge and the oxygen K-edge before and after beam damage occurred. The measurements were performed at an acceleration voltage of 300 kV.

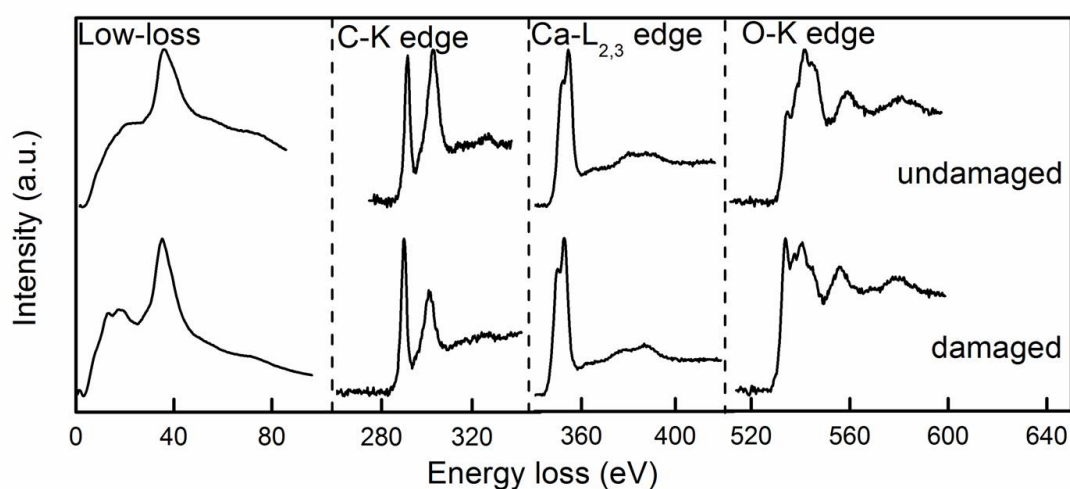


Figure 7.7 EELS measurements taken in diffraction mode on the Iceland spar plan-view samples giving the low-loss region, the carbon K-edge, the calcium L_{2,3}-edge and the oxygen K-edge before and after beam damage occurred. The investigations were done at an acceleration voltage of 300 kV.

EELS measurements were performed in diffraction mode using the plan-view and the cross-section coccolith and Iceland spar samples. Since the spectra of the plan-view and the cross-section samples are similar, the spectra of the plan-view samples are exemplarily shown here (Figs. 7.6 and 7.7). The performed EELS measurements as well as the SAED experiments and HR imaging show that the material is changing under electron beam bombardment. This transformation can be observed for the *E. huxleyi* coccolith (Fig. 7.6) and the Iceland spar samples (Fig. 7.7). For the Iceland spar samples the acquisition time was shortened to 1 s with 10 read-out cycles for the carbon C-K and calcium Ca-L_{2,3} edge and to 1 s with 100 iterations for the oxygen O-K edge. With these parameters the calcite did not transform during the measurement. The EELS measurements for the *E. huxleyi* coccolith were performed for 1 s with 100 interactions for the C-K and the Ca-L_{2,3} edge and with 10 s with 20 interactions for the O-K edge. Due to the lower acquisition times the element specific edges are noisier for the Iceland spar samples (Fig. 7.7) compared to the spectra of the coccolith plan-view samples (Fig. 7.7). The low-loss region reveals a dominant peak at around 36 eV belonging to the Ca-M_{2,3} edge (edge onset at around 25.5 eV) superimposed on the plasmon peak. The low-loss region of the coccolith and the Iceland spar appear clearly different after material transformation. While the features in the low-loss region of the undamaged samples show a small intensity peak followed by a high intensity peak at around 36 eV with a small width, the small peak splits into two peaks and gets more prominent in the damaged samples (Figs. 7.6 and 7.7). Within the energy resolution of our EELS experiments, the ELNES of the C K-edge as well as the Ca-L_{2,3} ELNES do not significantly change (except for a change in the intensity ratio between the peaks of the C-K-edge). In contrast the O-K edge does clearly change (Figs. 7.6 and 7.7). The O-K edge of the undamaged samples reveals two characteristic features at the beginning of the edge, a small pre-peak followed by a high intensity main peak with a shoulder at the high energy side (Figs. 7.6 and 7.7). After material transformation the intensity of the pre-peak increases and the shape of the main peak changes (Figs. 7.6 and 7.7).

7.4 Discussion

Radiation damage occurring during TEM investigations is a well known phenomenon and various observations are described in literature [7, 8, 24, 25]. Egerton *et al.* reviewed different ways in which the electron beam can affect inorganic and organic samples during electron microscopic examination [7]. This study confirmed that the amount of radiation damage is proportional to the electron dose and the amount of energy deposited in the specimen [7]. They found that a highly condensed electron beam can induce severe beam damage. Egerton reported in 2013 about the control of radiation damage for soft materials and organic specimen by low-dose techniques, cooling or encapsulating procedures. In addition the choice of the imaging mode, incident-beam diameter as well the incident-electron energy was discussed [24].

Srot *et al.* demonstrated the strong influence of the electron beam on mineralized dental tissues and dental pulp. In their study the changes in composition and the associated differences in the

ELNES were shown for different sample preparation methods [26]. They used FIB sectioning by Ga^+ ions, ultramicrotomy, pulverization and tripod polishing followed by Ar^+ ion-milling performed with liquid nitrogen cooling. They found tripod polishing followed by low Ar^+ ion energy milling (at low temperature) is best suited for their material [26].

Our investigation of the biological and mineralogical formed calcite prepared with two different techniques revealed that all samples have similar stability and behavior under electron bombardment. The transformation of single-crystalline calcite into a poly-crystalline material could be observed for all four samples with SAED and HRTEM. The analysis of the diffraction pattern revealed, considering a systematic error of 3 %, that the material is either poly-crystalline lime or poly-crystalline aragonite. The latter is unlikely to form, however, only additional EELS measurements allow to determine uniquely, which material is formed during the transformation. In comparison with the low-loss data for lime of Mkhoyan *et al.* [27] and for aragonite of Katti *et al.* [28] it turned out that the poly-crystalline material is lime. The peaks in the low-loss region of CaO show significant characteristics, which are comparable with the features of our measurement, while the low-loss region of aragonite is similar to the low-loss region of calcite. This result could be confirmed by comparison of the oxygen K-edge ELNES with the data for lime of Mkhoyan *et al.* [27] and for aragonite of Srot *et al.* [29]. The oxygen K-edge ELNES of lime shows similar features as observed in our data after beam damage had occurred (Figs. 7.6 and 7.7), while the oxygen K-edge ELNES of aragonite possesses different characteristic features.

The transformation of calcite to lime under electron beam bombardment was already described by Boynton [30]. Ruiz-Agudo *et al.* [9] and Rodriguez-Navarro *et al.* [10] used two dimensional X-ray diffraction and TEM diffraction experiments to study the phase transformation of calcite by thermal decomposition as well as by electron beam bombardment. They also observed the formation of lime. Reyes-Gasga and Garcia-Gacia [25] studied the electron-beam-sample interaction using an accelerating energy range from 0.1 to 2 MeV. The analysis was based on the standard theory for fast electrons. This theory was applied for the systems $\text{YBA}_2\text{Cu}_3\text{O}_{7-x}$, $\text{Al}_{62}\text{Cu}_{20}\text{Co}_{15}\text{Si}_3$ and the tooth enamel hydroxylapatite. In this study it was shown that in samples consisting of different atomic species, atoms with small binding energy are displaced first. The remaining atoms are displaced at higher acceleration voltages and amorphization could be observed [25]. Beside that the acceleration voltage and the temperature are important factors. The developed theory described the individual atomic behavior in crystals before disordering takes place [25]. In the case of the tooth enamel hydroxyapatite a transformation to lime under expulsion of $(\text{OH})^-$ ions was observed [25]. In our work the transformation of calcite to lime was also noticed. Here the transformation occurs under CO_2 dispersion, which was also described by Rodriguez-Navarro *et al.* [10]. This material change can be attributed to heating processes in the TEM and the binding energy of the material [10].

In our study the electron beam stability of biological and mineralogical grown calcite was compared. We found no significant differences in stability for the biological calcite of *E. huxleyi* and the mineralogical single-crystalline calcite (Iceland spar). In addition a similar transformation behavior was observed. This is mostly related to the finding that an organic layer is surrounding

the coccoliths and organic is not present within the crystal units or between nanosized calcite crystals. This is different compared to other multi-cellular marine calcifiers [23]. Accordingly the coccoliths behave similar as geological calcite and this explains why they resist a relatively high accumulated dose.

A further aim was to investigate if the sample preparation has an influence on the stability of the samples. Our findings reveal that the *E. huxleyi* and Iceland spar plan-view samples prepared by etching with dH₂O as well as the cross-section samples prepared by FIB sectioning behave similar under electron bombardment and show beam damage above an accumulated dose of $\sim 10^5$ e/nm². In conclusion, we did not find any significant effect of the preparation techniques for the sample stability.

Our results show that it is possible to investigate calcite samples at 300 kV by fast using a moderate maximum dose of $\sim 10^5$ e/nm². Recently we have studied *E. huxleyi* samples with an acceleration voltage of 80 kV and a low dose, with a focus on the crystallographic orientation of the R-unit and the V-unit and the assembly of the R-unit [23]. Herby we reduced the knock-on damage and the material transformation to lime occurred after longer acquisition times [23]. It is worth to mention that other types of beam damage might occur at 80 kV. Nevertheless, the resolution especially for HRTEM imaging is much better for 300 kV and thus the finding of the present study will allow us to observe structural changes caused by pH variations in the future.

The results of this study show that both sample preparation methods are very well suitable for biological and mineralogical calcite samples. Cross-section preparation for the *E. huxleyi* coccoliths by FIB sectioning is very appropriate. Pronounced artifacts or defects caused by the ion milling could not be observed in the TEM, at least in the interior of the coccolith segments (Fig. 7.3a-c) and the stability of the crystals is not affected, as confirmed by comparison with the plan-view samples (Fig. 7.2a-c). The sample preparation of the plan-view coccolith samples by etching with distilled water turned out to be a very gentle method to obtain adequate electron transparent samples for TEM investigations. In comparison with the more aggressive HCl our study reveals that by etching with distilled water the coccolith assembly stays intact and the delicate structure of *E. huxleyi* can be preserved. In addition, the comparison between the results of the South Atlantic samples prepared by FIB and the ones obtained by thinning with dH₂O show that demineralization does not occur.

7.5 Conclusion

Preparation methods for TEM plan-view and cross-section samples were successfully developed and adjusted for the sensitive shell of *E. huxleyi* and Iceland spar. The electron beam sensitivity of the biological and mineralogical calcite was investigated by HRTEM, electron diffraction and EELS in order to find suitable parameters for TEM measurements. The results show that both preparation techniques, FIB sectioning for cross-section and dH₂O etching for plan-view studies, lead to samples which can be illuminated with an parallel electron beam up to an accumulated dose of $\sim 10^5$ e/nm² without altering the ultrastructure. For longer acquisition

times, the diffraction pattern indicated a change from single-crystalline calcite into a polycrystalline material. This was confirmed by HRTEM, where the formation of nano-crystals was observed. Changes in the low loss region of EEL spectra as well as in the ELNES of the element specific O-K edges indicate the formation of lime. No significant differences in the electron beam stability of the biological and mineralogical grown calcite were found. With these findings, studies of the CaCO₃ shell of *E. huxleyi* in dependence on the environmental conditions become feasible.

7.6 Bibliography

- [1] SOLOMON, S., QIN, D., MANNING, M., CHEN, Z., MARQUIS, M., AVERYT, K. B., TIGNOR, M., AND MILLER, H. L., Eds. *Climate change 2007: The physical science basis: Contribution of working group I to the fourth assessment report of the intergovernmental panel on climate change*. Cambridge University Press, Cambridge, United Kingdom and New York, 2007.
- [2] RAUPACH, M. R., MARLAND, G., CIAIS, P., LE QUÉRÉ, C., CANADELL, J. G., KLEPPER, G., AND FIELD, C. B. Global and regional drivers of accelerating CO₂ emissions. *Proceedings of the National Academy of Sciences of the United States of America* **104**, 24 (2007), 10288–10293.
- [3] SABINE, C. L., FEELY, R. A., GRUBER, N., KEY, R. M., LEE, K., BULLISTER, J. L., WANNINKHOF, R., WONG, C. S., WALLACE, D. W. R., TILBROOK, B., MILLERO, F. J., PENG, T.-H., KOZYR, A., ONO, T., AND RIOS, A. F. The oceanic sink for anthropogenic CO₂. *Science* **305** (2004), 367–371.
- [4] BECKAGE, B., OSBORNE, B., GAVIN, D. G., PUCKO, C., SICCAMA, T., AND PERKINS, T. A rapid upward shift of a forest ecotone during 40 years of warming in the Green Mountains of Vermont. *Proceedings of the National Academy of Sciences of the United States of America* **105**, 11 (2008), 4197–202.
- [5] DONEY, S. C., FABRY, V. J., FEELY, R. A., AND KLEYPAS, J. A. Ocean acidification: the other CO₂ problem. *Annual Review of Marine Science* **1** (2009), 169–192.
- [6] BOYD, P. W., DONEY, S. C., STRZEPEK, R., DUSENBERRY, J., LINDSAY, K., AND FUNG, I. Climate-mediated changes to mixed-layer properties in the Southern Ocean: assessing the phytoplankton response. *Biogeosciences* **5** (2008), 847–864.
- [7] EGERTON, R. F., LI, P., AND MALAC, M. Radiation damage in the TEM and SEM. *Micron* **35** (2004), 399–409.
- [8] WILLIAMS, D. R., AND CARTER, B. C. *Transmission electron microscopy a textbook for material sciences*, 2 ed. Springer-Verlag, New York, 2009.

- [9] RUIZ-AGUDO, E., RODRIGUEZ-NAVARRO, C., LUQUE, A., RODRIGUEZ-NAVARRO, A., AND ORLTEGA HUERTAS, M. A TEM and 2D-XRD study of the thermal decomposition of calcite. *Revista de la sociedad española de mineralogía* **9** (2008), 223–224.
- [10] RODRIGUEZ-NAVARRO, C., RUIZ-AGUDO, E., LUQUE, A., RODRIGUEZ-NAVARRO, A. B., AND ORTEGA-HUERTAS, M. Thermal decomposition of calcite: Mechanisms of formation and textural evolution of CaO nanocrystals. *American Mineralogist* **94** (2009), 578–593.
- [11] MOHAMED, M., YUSUP, S., AND MAITRA, S. Decomposition study of calcium carbonate in cockle shell. *Journal of Engineering and Technology* **7**, 1 (2012), 1–10.
- [12] WINTER, A., AND SIESSER, G. W., Eds. *Coccolithophores*. University Press, Cambridge, 1994.
- [13] HONJO, S. Coccoliths: production, transportation and sedimentation. *Marine Micropaleontology* **1** (1976), 65–79.
- [14] YOUNG, J. R., AND HENRIKSEN, K. Biomineralization within vesicles: The calcite of coccoliths. *Reviews in Mineralogy and Geochemistry* **54** (2003), 189–215.
- [15] WATABE, N. Crystallographic analysis of the coccolith of *Coccolithus huxleyi*. *Calcified Tissue Research* **1** (1967), 114–21.
- [16] MANN, S., AND SPARKS, N. H. C. Single crystalline nature of coccolith elements of the marine alga *Emiliana huxleyi* as determined by electron diffraction and high-resolution Transmission. *Proceedings of the Royal Society B: Biological Sciences* **234** (1988), 441–453.
- [17] DAVIS, S. A., YOUNG, J. R., AND MANN, S. Electron microscopy studies of shield elements of *Emiliana huxleyi* coccoliths. *Botanica Marina* **38** (1995), 493–497.
- [18] SARUWATARI, K., OZAKI, N., NAGASAWA, H., AND KOGURE, T. Comparison of crystallographic orientations between living (*Emiliana huxleyi* and *Gephyrocapsa oceanica*) and fossil (*Watznaueria barnesiae*) coccoliths using electron microscopes. *American Mineralogist* **93** (2008), 1670–1677.
- [19] WILBUR, K. M., AND WATABE, N. Experimental studies on calcification in molluscs and the alga *Coccolithus huxleyi*. *Annals of the New York Academy of Sciences* **109** (1963), 82–112.
- [20] DIDYMUS, J. M., YOUNG, J. R., AND MANN, S. Construction and morphogenesis of the chiral ultrastructure of coccoliths from the marine alga *Emiliana huxleyi*. *Proceedings of the Royal Society London B: Biological Sciences* **258** (1994), 237–245.
- [21] EGERTON, R. F. *Electron energy-loss spectroscopy in the electron microscope*, 3 ed. Springer Science+ Business Media, New York, 2011.

-
- [22] MAYER, J., GIANNUZZI, L. A., KAMINO, T., AND MICHAEL, J. TEM sample preparation and FIB-induced damage. *MRS Bulletin* **32** (2007), 400–407.
- [23] HOFFMANN, R., WOCHNIK, A. S., HEINZL, C., BETZLER, S. B., MATICH, S., GRIESSHABER, E., SCHULZ, H., KUČERA, M., YOUNG, J. R., SCHEU, C., AND SCHMAHL, W. W. Nanoprobe crystallographic orientation studies of isolated shield elements of the coccolithophore species *Emiliana huxleyi*. *European Journal of Mineralogy* **26**, 4 (2014), 473–483.
- [24] EGERTON, R. F. Control of radiation damage in the TEM. *Ultramicroscopy* **127** (2013), 100–108.
- [25] REYES-GASGA, J., AND GARCIA-GARCIA, R. Analysis of the electron-beam radiation damage of TEM samples in the acceleration energy range from 0.1 to 2 MeV using the standard theory for fast electrons. *Radiation Physics and Chemistry* **64** (2002), 359–367.
- [26] SROT, V., BUSSMANN, B., SALZBERGER, U., KOCH, C. T., AND VAN AKEN, P. A. Linking microstructure and nanochemistry in human dental tissues. *Microscopy and Microanalysis* **18** (2012), 509–523.
- [27] MKHOYAN, K. A., SILCOX, J., MCGUIRE, M. A., AND DISALVO, F. J. Radiolytic purification of CaO by electron beams. *Philosophical Magazine* **86**, 19 (2006), 2907–2917.
- [28] KATTI, K. S., QIAN, M., FRECH, D. W., AND SARIKAYA, M. Low-loss electron energy-loss spectroscopy and dielectric function of biological and geological polymorphs of CaCO₃. *Microscopy and Microanalysis* **5** (1999), 358–364.
- [29] SROT, V., WEGST, U. G. K., SALZBERGER, U., KOCH, C. T., HAHN, K., KOPOLD, P., AND VAN AKEN, P. A. Microstructure, chemistry, and electronic structure of natural hybrid composites in abalone shell. *Micron* **48** (2013), 54–64.
- [30] BOYNTON, R. S. *Chemistry and technology of lime and limestone*, 2 ed. Wiley-Interscience, New York, 1980.

8 Insight in *Emiliana huxleyi* coccospheres by focused ion beam sectioning

This chapter is based on the following publication:

Hoffmann R., Kirchlechner C., Langer G., Wochnik A. S., Griesshaber E., Schmahl W. W. and Scheu C. (2015): *Biogeosciences* **12** 825-834

8.1 Introduction

In the context of the current climate change debate, understanding ecosystem response to environmental disturbances has become a matter of unprecedented urgency. To predict how ecosystems in general and groups of organisms in particular will respond to ongoing changes such as global warming and ocean acidification, an understanding of past climate changes and the corresponding response of organisms is pivotal [1, 2]. The marine sedimentary archive potentially provides an enormous database of past organismal responses to climate change [3]. In particular, the calcium carbonate shells of the major pelagic calcifiers – coccolithophores and foraminifera – constitute an archive that extends for tens of millions of years [4, 5]. Coccolithophores are surrounded by a sphere (termed coccosphere) of interlocking calcareous platelets, the coccoliths which consist primarily of a radial array of complexly shaped crystals of calcite [6, 7, 8]. Both the chemical composition of coccoliths and the morphology of the coccosphere as well as of the coccoliths provide information about physiological parameters such as growth and calcification rate at different times in the geological past [9, 2]. The morphological analysis of coccospheres and coccoliths relies on SEM, a tool which renders the accurate determination of size and morphological modification possible [10, 11]. Until now, SEM samples were often prepared by means of conventional sample preparation methods – either smearing coccoliths onto sample holders or using the microtome to create single cross sections through the cells. However, advances in technology now allow us to serially image and section through the coccospheres, opening up a whole new way of observing coccosphere architecture. This is important since some features cannot be revealed by classical SEM. The number of coccoliths per cell, for instance, can only be estimated on the basis of the coccoliths that can actually be seen [11]. The coccolith quota is needed to calculate particulate inorganic carbon (PIC) quota. The inner coccosphere diameter, which equals the cell diameter, can be used to calculate particulate organic carbon (POC) quota. Both coccolith quota and inner coccosphere diameter cannot be determined using con-

ventional SEM, but can be obtained accurately by FIB sectioning combined with SEM. The PIC/POC ratio determines whether coccolithophores act as a source or a sink of CO₂ relative to the atmosphere [12, 13, 14] and therefore is an important variable for modeling carbon cycling in the oceans [15]. Moreover, coccolithophore response to climate change is often expressed in terms of PIC and POC quotas. Shedding light on these features and gaining further insight into coccosphere architecture requires step-by-step cross sectioning of complete coccospheres.

A helpful tool to gain information on the interior architecture of samples is FIB-SEM [16, 17, 18, 19, 20]. This combination enables bulk samples to be locally sectioned by means ion milling and subsequently imaged at high resolution [21]. This application of FIB-SEM instruments is commonly referred to as FIB tomography [16, 22]. Using FIB-SEM tomography to investigate insulators like biological, geological and ceramic samples is challenging because of charging effects that disturb the sectioning as well as the imaging [21]. Nevertheless the FIB-SEM microscope is often used to analyse biological materials which are difficult to cut, such as teeth [23] and bones [24]. Another application for FIB-SEM microscopes in biology is the preparation of thin lamellae which can be analysed in a TEM [21, 25, 26]. Using BSE instead of SE for the image formation allows for discrimination of differently aligned crystals with the same mass contrast due to channelling contrast mechanisms, which depend on the crystallographic orientation of the investigated volume [21].

In the present work FIB-SEM sectioning and SE as well as BSE imaging were used to study the coccosphere's internal architecture and to determine the coccolith quota of the abundant coccolithophore species *E. huxleyi*. The so obtained information was used to calculate the PIC/POC ratio and to estimate the density as well as the sinking velocity of individual coccolithophore cells.

8.2 Materials and methods

8.2.1 Samples

Clonal cultures of *E. huxleyi* type A (strain RCC1238) [27] were grown in aged, sterile-filtered (0.2 μm pore-size cellulose-acetate filters) North Sea seawater enriched with 100 $\mu\text{mol L}^{-1}$ nitrate, 6.25 $\mu\text{mol L}^{-1}$ phosphate, trace metals and vitamins as in f/2 medium [28]. The strains were obtained from the Roscoff Culture Collection (www.sb-roscoff.fr/Phyto/RCC). The cultures were grown under a 16 : 8 hour light–dark cycle at a light intensity of 400 $\mu\text{mol photons m}^{-2}\text{s}^{-1}$ in an adjustable incubator (Rubarth Apparate GmbH, Germany) at 20 °C. Cells were grown in dilute batch cultures, ensuring a quasi-constant seawater carbonate system over the course of the experiment [29].

The sample was filtered directly after the collection with a vacuum pump onto an Omnipore polycarbonate membrane filter (diameter: 47 mm; pore size: 0.45 μm), which was dried at 60 °C. The material was then removed with a spatula from the dried filter and dissolved in ethanol. Next the sample was dropped on a Si-Wafer and dried. In order to protect the sensitive sample

material from electron beam damage and to avoid charging effects, a thin carbon film using a BAL-TEC coating system was deposited.

8.2.2 Serial sectioning and imaging

Serial sectioning was performed with a Zeiss Auriga[®] crossbeam, using the SEM for imaging and the FIB microscope for cutting roughly 50 nm thick slices from the coccolithophore samples. The acceleration voltage of the SEM was set to 2 kV, and a 30 μm aperture was chosen, resulting in a 20 pA imaging current. The Auriga[®] is equipped with SE, BSE and in-lens detectors, which were used to image the cross-sectional slices at constant contrast and brightness settings.

The FIB gun was operated with 30 kV Ga^+ ions and a current of 240 pA. During the cutting process the FIB gun is inclined by 54° with respect to the SEM gun and no sample rotation or tilt is required for imaging the cross section of the cut sphere. In order to minimize the ion beam damage, a local electrode was used to avoid charging and drift correction was performed before and after each slice. Drift correction and slice thickness measurement were carried out using a cross-marker in a post-processing step.

8.2.3 Carbon quota and density estimates

The cellular PIC quota was calculated using the following equation [29, 10]:

$$\frac{PIC[pg]}{cell} = n \times m \times \frac{M_C}{M_{CaCO_3}} = n \times \rho \times \frac{M_C}{M_{CaCO_3}} \times V = n \times \rho \times \frac{M_C}{M_{CaCO_3}} \times k_s \times L^3. \quad (8.1)$$

Here, n is the number of coccoliths per cell (coccosphere); m is the mass of one coccolith; $\frac{M_C}{M_{CaCO_3}}$ is the molar mass ratio of C and CaCO_3 , which is equal to 0.12; ρ is the density of the coccolith; and V is the volume of one coccolith. V can be estimated using the coccolith length L and the shape constant k_s [10]. To compare our results to those of the literature, we used a coccolith length of $L = 3.5 \pm 1.0 \mu\text{m}$ and the *E. huxleyi* morphotype A shape constant value $k_s = 0.020 \pm 0.004$ [10]. In addition, a density value of $\rho = 2.7 \text{ pg}/\mu\text{m}^3$ was used, which is based on the assumption that the coccoliths are pure calcite [10]. The parameter n , the number of coccoliths per cell, was determined experimentally by using the FIB sectioning.

The cellular POC quota can be calculated according to the literature as follows [30]:

$$\frac{POC[pg]}{cell} = a \times V_{cell}^b. \quad (8.2)$$

Here, V_{cell} is the volume of the cell (protoplast), which is calculated from the inner coccosphere diameter, and a and b are constants which vary depending on the investigated species. For plankton the literature values obtained via log–log plots are $b = 0.939$ (with a 95% confidence interval of 0.041) and $\log a = -0.665$ (with a 95% confidence interval of 0.132), resulting in a value of $a = 0.216$ [30]. For better comparison with the literature, we have used these values for our calculations. The inner coccosphere diameter was obtained experimentally by using the

FIB cross sections.

The overall cell density was calculated from the total cell volume and mass. The total cell volume was estimated using the outer coccosphere diameter. The total cell mass was calculated as follows: the density of the protoplast was assumed to be equal to the density of seawater. Using this assumption and the inner coccosphere diameter, i.e. the maximum protoplast diameter, the mass of the protoplast was calculated. The mass of the coccosphere, i.e. the calcite extracellular matrix mass and the non-calcite extracellular matrix mass, was calculated by using the cellular PIC quota, converted to the cellular calcite quota. The cellular calcite quota divided by the density of calcite yields the volume of the coccosphere occupied by calcite. The volume derived from the outer coccosphere diameter minus the volume derived from the inner coccosphere diameter yields the total coccosphere volume, precisely the volume of the extracellular matrix. The latter minus the volume of the coccosphere occupied by calcite equals the volume of the coccosphere not occupied by calcite. This residual volume was assumed to have the density of seawater. Using the non-calcite coccosphere volume and the density of seawater, the mass of the non-calcite coccosphere volume can be calculated. The total cell mass was therefore the sum of the protoplast mass, the non-calcite extracellular matrix mass and the calcite extracellular matrix mass. The total cell mass divided by the volume derived from the outer coccosphere diameter equals the overall cell density. The sinking velocity was calculated according to Stokes law [31] using the overall cell density, the outer coccosphere radius, the density of seawater ($1.024 \text{ pg}/\mu\text{m}^{-3}$) the dynamic viscosity of seawater ($0.00107 \text{ kgms}^{-1}$) and the acceleration due to gravity (9.81 ms^{-2}).

8.3 Results

To investigate the 3D morphology of the coccolithophore species *E. huxleyi* serial sectioning in the SEM-FIB was used. SE images acquired at different stages of the milling (the video of the whole sequence can be found in the supplementary information) illustrate the complex morphology of *E. huxleyi* (Fig. 8.1). Starting from a single complete coccosphere (Fig. 8.1.1), the individual coccoliths are milled by Ga^+ ions (Fig. 8.1.2). When the interior of the cell is reached, it becomes obvious that the individual coccolith platelets are layered (Fig. 8.1.3 and 8.1.4). For the shown example, the layers of coccoliths are uneven (Fig. 8.1.5 and 8.1.6.); however this is only visible after the middle of the coccosphere is reached. These results imply that the whole coccosphere has to be milled (Fig. 8.1.7 and 8.1.8), and it is not sufficient just to mill part of the organism. Our methodology also enables us to visualize the organic residues and intracellular coccoliths within the coccospheres (Fig. 8.1). However, for a detailed study of the intracellular coccolith, it would be necessary to reduce beam damage of the organic material even further by using, for example, a He source instead of a Ga source in the FIB.

To get reliable information of the coccosphere architecture of a specific strain, it is not sufficient to mill only one sample. Exemplary SE images of six sliced *E. huxleyi* coccospheres are summarized in Fig. 8.2. To illustrate the size distribution of the cell cavity, the images used for

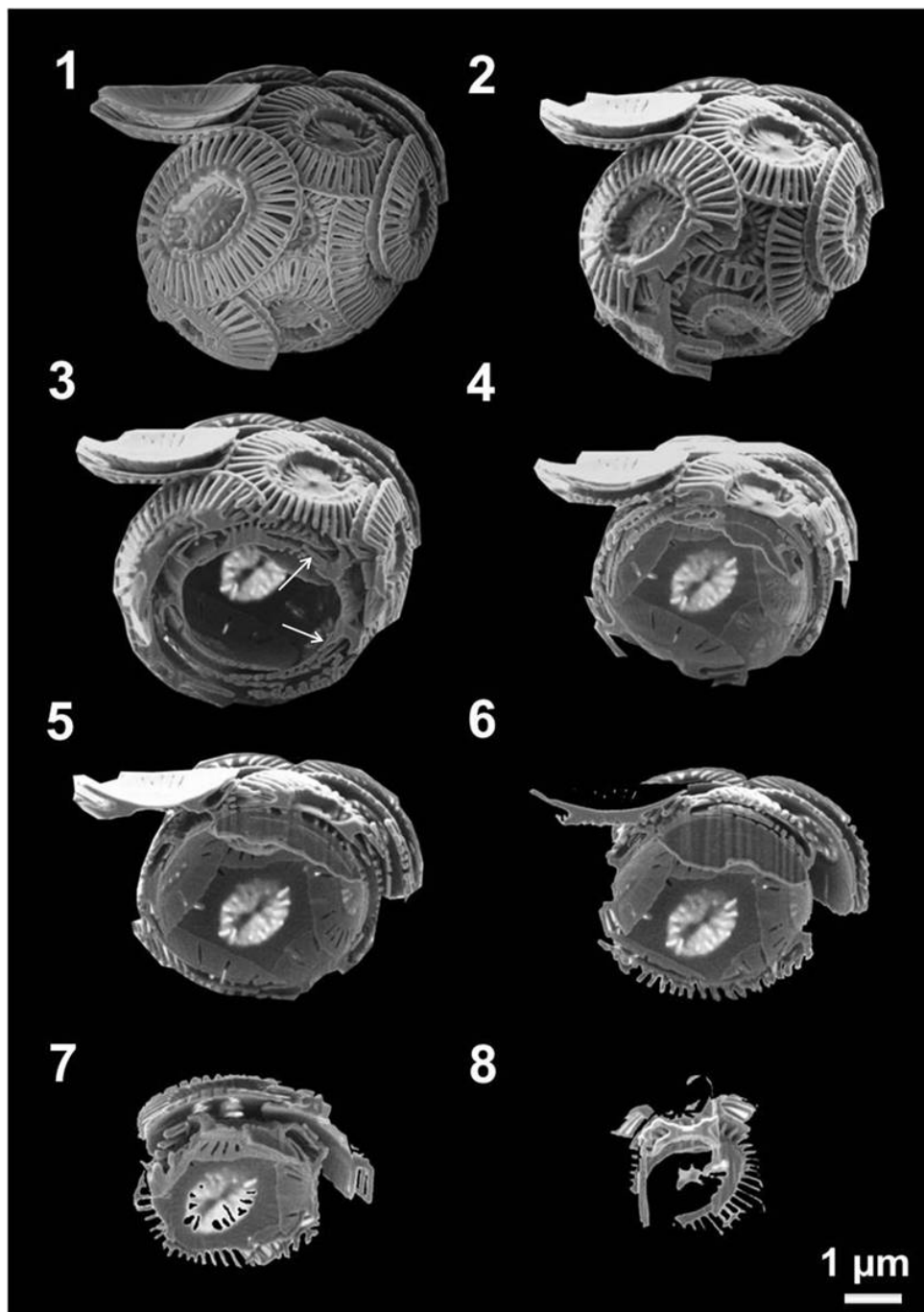


Figure 8.1 SEM-FIB sectioning sequence of the coccolithophore species *E. huxleyi*. Image 1 shows the complete coccosphere before slicing, and in 2 the sectioning has just begun. Images 3 and 4 reveal the interlocked layers of coccoliths which make up the coccosphere. The coccosphere is formed by three coccolith layers at the upper region and one in the lower region (5). An organic residue of the coccolithophore cell in the upper area of the sphere is visible in 6. In 7 and 8 the last steps of the sectioning can be seen.

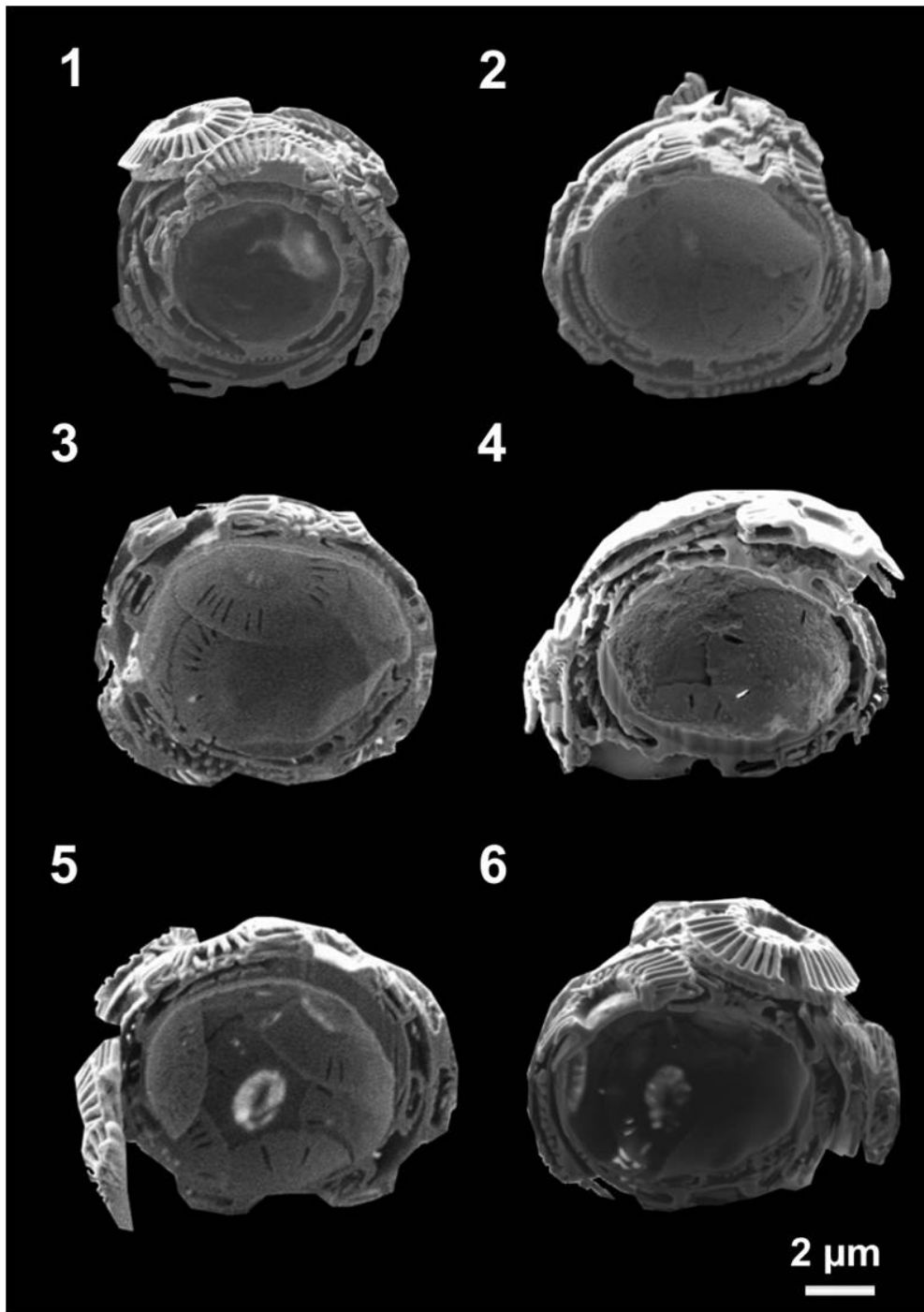


Figure 8.2 Six exemplary SE images of cross sections through the coccolithophore species *E. huxleyi*. The coccosphere in image 1 is composed of four coccolith layers and shows the highest shell thickness. In 2 a coccosphere composed of three coccolith layers given. A coccosphere that indicates that the coccolith layers are not equally spread over the sphere is shown in image 3 and 4. Images 5 and 6 reveal that the shell thickness of the coccospheres is different depending on the number of coccolith layers.

this figure show the maximum diameter of the cavity. The architecture, i.e. the interlocking of individual coccoliths, as well as the diversity in coccolith layer numbers and the assembly of the coccolith layers can be seen. We found that the coccospheres of our cultured clone are quite heterogeneous. Some have three layers of coccoliths (Fig. 8.2.2 and 8.2.4), whilst others have only two (Fig. 8.2.3). Only one coccosphere was found which had four layers of coccoliths and a smaller inner coccosphere diameter compared to the others (Fig. 8.2.1). Whether this represents a trend, however, cannot be decided on the basis of a single observation. Most of the coccospheres have an unequal number of layers (Fig. 8.2.3–8.2.6), which may correspond had coccoliths that were evenly distributed. The FIB-SEM data indicate that the thickness of the coccospheres is related to the coccolith layer number.

The number of coccoliths that make up the sphere were also counted and used for the calculation of the POC quota. Two different approaches were used to determine the coccolith quota. In one approach only one SEM image was used. Here all visible coccoliths were counted and the coccoliths on the reverse side were estimated. An average of 15 coccoliths were found for the coccospheres containing 2–3 layers. In a second approach the total coccolith number was counted by using the FIB section series. This method showed that the 2–3-layer coccospheres consist of around 20 coccoliths per cell.

Serial SEM-FIB sectioning was performed at 27 different *E. huxleyi* coccolithophores to compare the inner and outer diameters, the number of the coccoliths and layers, and their influence on the shell thickness. The SE images which showed the maximum diameter of the cavity were used to measure the diameter of the outer and inner coccosphere shell. The correlation between inner and outer diameter of the coccosphere shell is given in Fig. 8.3. The open circles denote the outer diameter and the filled circles the inner sphere diameter, which are plotted in Fig. 8.3a as a function of the maximum number of layers (in the case of non-equally distributed number of coccoliths). The gray lines correspond to the fitted slope as well as to the calculated 0.9, 0.95, and 0.99 confidence levels. The inner diameter of the coccosphere, which equals the cell diameter, is independent of the maximum number of coccolith layers, while the outer diameter increases linearly with the maximum number of coccolith layers. In addition, in Fig. 8.3b we have plotted the inner and outer diameter of the coccosphere as a function of the number of coccoliths forming this shell. A similar trend can be observed with the inner diameter remaining nearly constant and the outer diameter increasing with increasing number of coccoliths.

Figure 8.4 shows the relationship between coccosphere thickness (outer–inner diameter) and the number of coccolith layers. As described above, the number of coccolith layers is evenly distributed over the coccosphere in only one of three cases. For the coccospheres where the coccoliths were not evenly distributed, the maximum number of layers was used in the plot. Coccospheres with 1–4 coccolith layers were observed and since most measured points are given for 2–3 layers, the average coccolith layer number for the strain used is 23 (Fig. 8.4). The plot also reveals that the coccosphere thickness increases by about $1 \mu\text{m}$ per coccolith layer (Fig. 8.4a). The thickness of the coccosphere as a function of the number of coccoliths forming this shell is given in Fig. 8.4b. It can be seen that the thickness is increasing linearly with

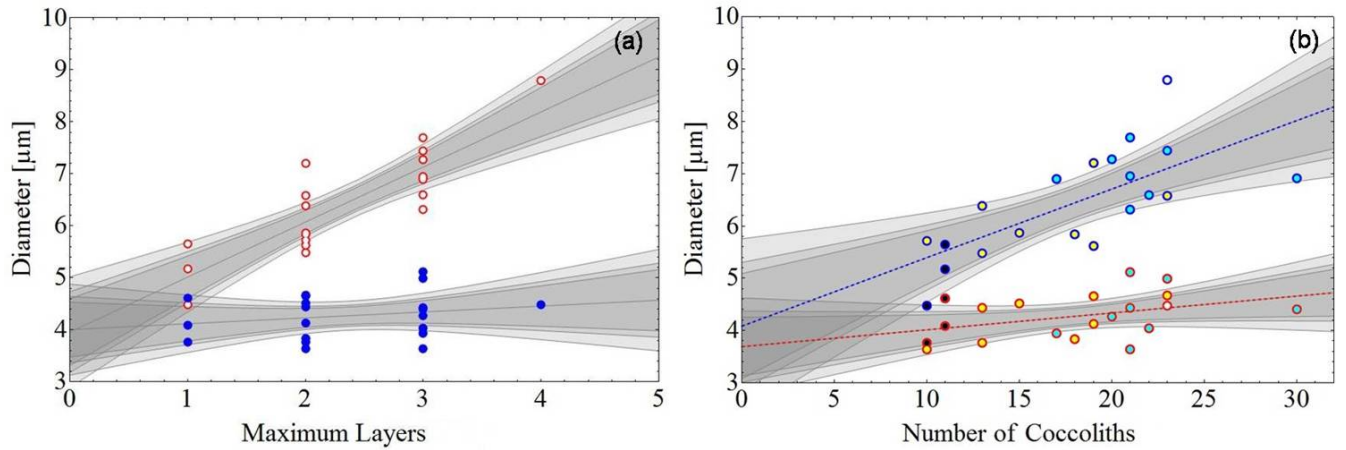


Figure 8.3 The correlation between inner and outer coccosphere diameter is illustrated. The filled blue circles in (a) show the measured values for the inner diameter, while the open red circle display the data for the outer diameter of the coccosphere. In (b) the dots with a blue shell refer to the outer and the ones with a red shell to the inner coccosphere diameter. The black filling relates to coccospheres with a maximum thickness of one layer, the yellow to those with a maximum of two layers, the blue to those with a maximum of three layers and the white to those with a maximum of four layers. The fitted slopes as well as the calculated 0.9, 0.95 and 0.99 confidence levels are given by the grey lines.

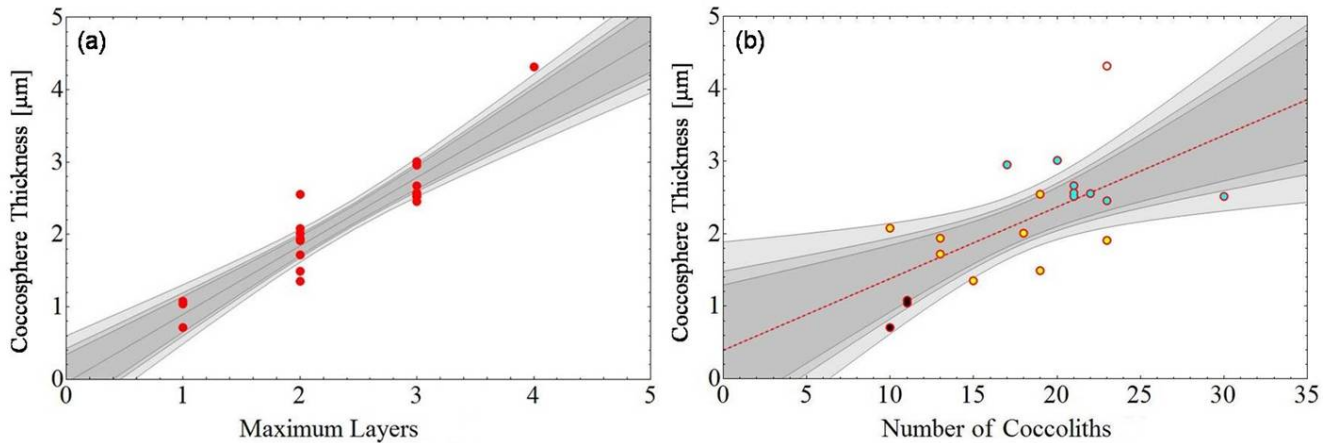


Figure 8.4 (a) The relationship between the number of coccolith layers which make up the sphere and the thickness of the coccosphere shell is given. A maximum four layers was found in this strain. It can be observed that the thickness increases by approximately $1 \mu\text{m}$ with each coccolith layer. (b) In this plot the thickness is plotted as a function of the number of coccoliths. The black dots refer to coccospheres with a maximum of one layer, the yellow to those with a maximum of two layers, the blue to those with a maximum of three layers and the white to those with a maximum of four layers. The fitted slopes as well as the calculated 0.9, 0.95 and 0.99 confidence levels are given by the grey lines.

increasing number of coccoliths. The fitted slope as well as the confidence level is given by the grey lines.

To gain detailed information of the coccosphere structure, different detectors were used for the imaging. In Fig. 8.5 a coccosphere cross section imaged using two different imaging methods is shown. An image obtained by a SE detector using the surface near secondary electrons is given in 8.5.1. Here the surface topography is illustrated and the SE image gives a three-dimensional impression due to the effect that surfaces which are inclined towards the detector appear brighter than surfaces that are turned away [32]. In Fig. 8.5.2 a BSE in-lens detector was used to create the micrograph. These images reveal information about the elements distribution. Light elements like carbon appear darker than elements or materials with a higher atomic number. Due to this so-called material/ compositional contrast the organic residue on the left side of the coccosphere appears dark gray (Fig. 8.5.2). Besides material contrast, channelling contrast can occur in BSE images, which depends on the crystallographic orientation of the investigated volume and allows for differentiating of differently aligned crystals with the same mass-contrast. Thus, the contrast differences of the coccoliths in the BSE image (brighter area at the lower right side of the coccosphere in Fig. 8.5) can be caused by differences in the crystallographic orientation of the calcite crystals and/or by differences in the angle of the exposed face relative to the beam.

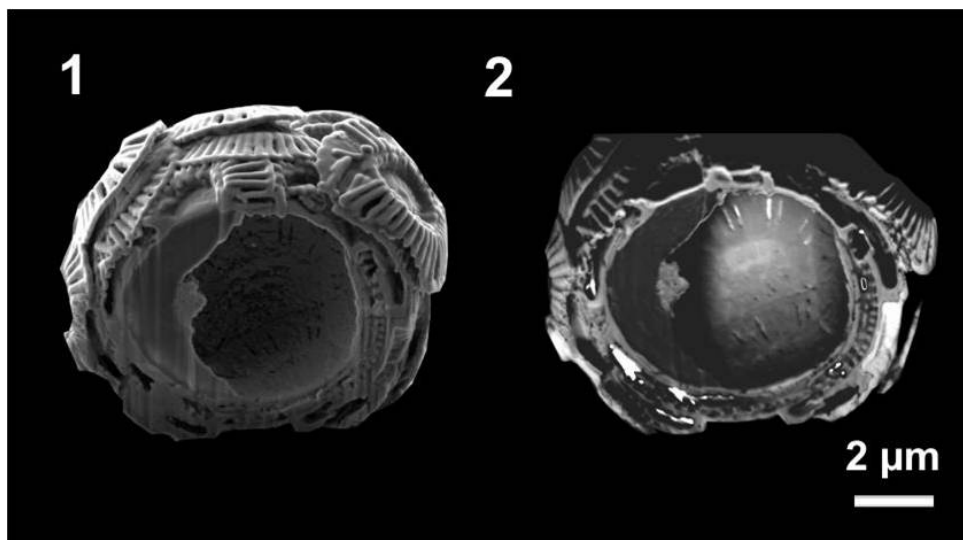


Figure 8.5 SEM images of the same coccosphere cross section taken using secondary electrons (1) and backscattered electrons (2). Secondary electrons are generated closer to the surface, so image 1 shows a lot more of the finer surface features. Backscattered electrons are sensitive to chemical composition, and are generated deeper in the sample.

8.4 Discussion

In the present study, FIB-SEM sectioning was used to obtain detailed information about the architecture of *E. huxleyi* coccospheres. FIB-SEM sectioning was shown to be appropriate for biological samples for the first time in 1993 [33]. Since this seminal study this method has improved and several groups have reported about the use of FIB-SEM microscopes for material sciences and biological materials [34, 18, 24, 35, 36, 37]. Nevertheless, the investigation of biological and non-conductive materials remains challenging due to the radiation-sensitive nature of these samples and their interaction with the electron and ion beam [36]. The quality of the imaging is limited by charging effects of the material [36]. In our study, charging was reduced by depositing a thin carbon film and using a local electrode close to the imaged area. Thus, drift due to charging during the FIB milling as well as SEM imaging was considerably reduced and a continuous drift correction before and after each slice was not necessary. Slice thickness evaluation and drift correction were only performed as a post-processing step using the SE images and a cross-marker. The combination of these methods allowed us to increase the imaging quality and to gain a relatively stable FIB section series. Nevertheless, charging effects could not be avoided completely.

In any case, we have shown that FIB-SEM sectioning is an appropriate method for analysing coccosphere architecture in a way which is impossible using conventional SEM. For instance, the number of coccoliths per cell can only be estimated on the basis of conventional scanning electron micrographs, because not all coccoliths can be seen. In an experimental study using *C. leptoporus* the number of visible coccoliths per coccosphere was analysed in this way [38]. This approach might yield a satisfactory result for *C. leptoporus*, which typically produces one layer of coccoliths only. However, the situation is more complicated in *E. huxleyi*, because the species does not stop coccolith production upon cessation of cell division [11] or completion of a coccosphere, resulting in multiple layers of coccoliths [39]. These multiple layers can even be seen in exponentially growing cultures such as the one analysed here. We showed that *E. huxleyi* RCC1238 features 2–3 layers of coccoliths, corresponding to 20 coccoliths per cell. Using the conventional SEM view of a coccosphere, only 15 coccoliths can be seen, which underestimates coccolith quota by 25%.

Another interesting aspect of multi-layer coccospheres is the diameter of the coccosphere. The outer coccosphere diameter was positively correlated with the number of layers (Fig. 8.3). Our results show that coccospheres composed of 1–3 coccolith layers have a quasi-constant inner diameter of about 4.36 μm (Fig. 8.3).

Since the cell diameter is positively correlated with the POC quota [30], the inner sphere diameter can be used to estimate POC quota. The corresponding PIC quota can be estimated using coccoliths per sphere and converting the coccolith size to mass [10]. Hence, these data render it possible to estimate the PIC/POC ratio of individual cells. We calculated a cellular POC quota of 7.2 (standard deviation (SD) 2.1) pg/cell and a PIC quota of 5 (SD 1.5) pg/cell. Both the POC and the PIC quota are lower than values determined on bulk samples using

elemental analysis via dynamical flash combustion [29]. The difference between our estimates and the data in [29], however, is very small considering the two radically different approaches used to determine carbon quotas. First, we used a small sample of individual cells as opposed to an average of millions of cells. Second, our estimates are based on standardised conversion factors, which might not be perfectly suited for this particular set of samples. Third, our raw data are biometrical as opposed to the chemical-analytical raw data on which the [29] data set is based. The PIC/POC ratio estimated here, i.e. 0.72 (SD 0.24), falls well within the range of values reported in [29]. The high, by comparison with data in [29], standard deviation of 0.24 reflects the fact that we picked a small number of cells comprising a considerable range with respect to number of coccolith layers or number of coccoliths (Fig. 8.6). Despite the large scatter in the data, a clear positive correlation between the PIC/POC ratio and the number of coccoliths and coccolith layers occurs (Fig. 8.6).

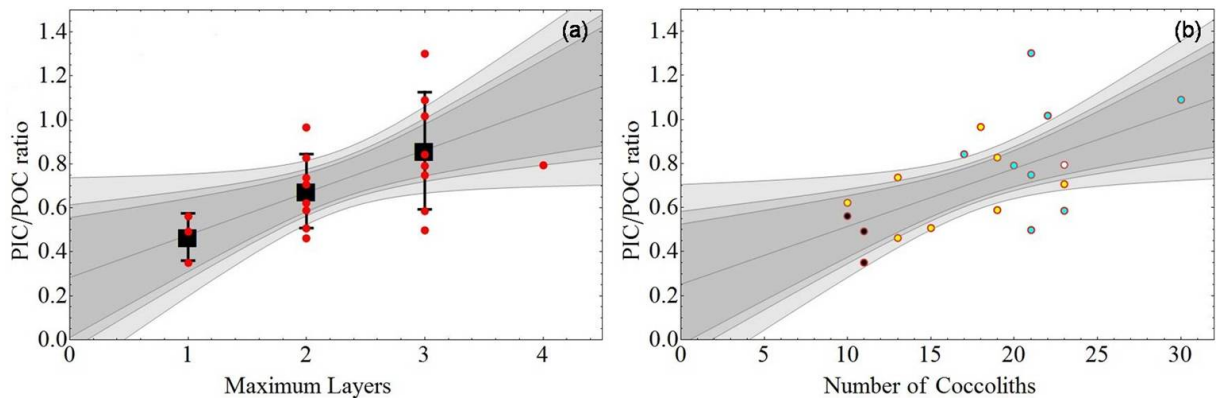


Figure 8.6 The calculated PIC/POC ratio as a function of (a) maximum layer of coccoliths and (b) number of coccoliths is given. In (b) the black dots refer to coccospheres with a maximum of one layer, the yellow to those with a maximum of two layers, the blue to those with to maximum of three layers and the white to those with a maximum of four layers. The fitted slopes as well as the calculated 0.9, 0.95, and 0.99 confidence levels are given by the gray lines.

At first glance this suggests that a higher PIC/POC ratio entails a higher overall density of the cell [40]. This assumption is important in the ongoing debate on the question of nutrient limitation of coccolithophores in particular and the function of coccoliths in general. It has been proposed that coccoliths may have a ballasting function by increasing the cell's density [31]. A widely held, but by no means uncontested [41, 42], notion is that nutrient limitation leads to increased calcification rate, which in turn leads to a higher overall cell density and thus increased sinking rate [43]. Indeed, several studies have shown an increase in *E. huxleyi*'s PIC/POC ratio due to nutrient limitation regardless of the calcification rate [44]. Our data set renders it possible to test the hypothesis that an increase in the PIC/POC ratio entails an increase in overall cell density and therefore sinking rate [40].

The overall cell density and the sinking velocity are plotted as a function of the PIC/POC ratios in Fig. 8.7. While the sinking velocity is linearly increasing with increasing PIC/POC

ratio, there is no good correlation between overall cell density and the PIC/POC ratio. Hence, a change in PIC/POC ratio alone is not sufficient to infer a change in overall cell density. While this might seem counter-intuitive, it reflects the fact that cell architecture plays an important role in defining overall cell density. This role of cell architecture has, understandably, been overlooked so far.

In the context of a standard culture experiment, the number of analyses required is at least an order of magnitude greater than the one performed in the present study. This is far too time-consuming for the scope of a standard culture experiment, which usually focuses on other parameters such as organic carbon production. However, density and sinking rate estimates might alternatively be based on light microscopy data [2], which are easier to obtain than FIB-SEM data. It would be worthwhile to perform a comparative study to figure out whether densities and sinking velocities based on light microscopy agree with those based on FIB-SEM data. The fossil material used by [2] would in fact be ideal for further studies, because it features, quite unusually, many complete coccospheres. Thus this material would additionally render it possible to apply the FIB-SEM method to fossil material. PIC and POC quotas as well as overall cell density and sinking rate are a very interesting amendment to the data presented by [2], because the authors showed that *Coccolithus* displays peak- Paleocene-Eocene Thermal Maximum (PETM)-specific cell geometry, namely higher coccolith quota and bigger coccospheres. PIC/POC ratios would allow for assessing this important calcifier's feedback on carbon cycling over the PETM, the closest geological approximation to current climate change. Sinking rates give insights into the nutrient-limitation-sinking-rate debate [43], because nutrient availability during the PETM was presumably considerably altered [2].

Our measurements have indicated that the overall cell density is not a linear function of the PIC/POC ratio but instead the data are scattering around a nearly constant value (Fig. 8.7a). In contrast, the sinking velocity is increasing linearly with increasing PIC/POC ratio (Fig. 8.7b). The reason for this is that Stokes' law, which was used to calculate the sinking rate, features not only particle density but also particle diameter. Hence only the combination of the latter two parameters allows for statements to be made about the sinking rate. Therefore it seems as if the PIC/POC ratio is a poor indicator of density, but possibly a useful one of sinking rate. That would vindicate the conclusion, if not the reasoning, of [40].

Is the method of estimating density employed here accurate enough? We argue that it is. First, the values calculated here agree well with the ones calculated by [45] based on a fundamentally different approach. Second, the assumptions made here are reasonable. Most marine phytoplankton cells have, indeed, a protoplast density which equals that of seawater [46]. Moreover it is reasonable to assume that the non-calcite space in the coccosphere (i.e. the extracellular matrix) has the density of seawater, because it actually is seawater in a polysaccharide matrix, and even if the polysaccharides present [47] should lower the density, this would only affect the absolute value of overall cell density and not the relationship of overall cell density and the PIC/POC ratio (Fig. 8.7a). In summary, our cell-architecture-based approach allows us to estimate, with sufficient accuracy, the overall density of an individual coccolithophore cell. Taken

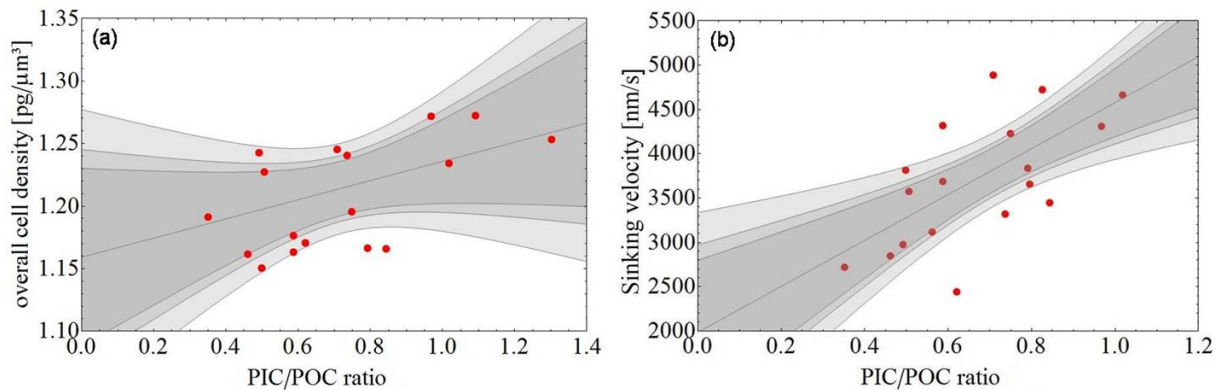


Figure 8.7 The overall cell density as function of the PIC/POC ratio is plotted in (a). The black line illustrates a linear trend that was assumed in the literature [44]. The linear regression is described by: $\text{density} = 0.08 \times (\text{PIC/POC}) + 1.16$ ($r^2 = 0.10$). In (b) the sinking velocity is plotted as a function of the PIC/POC ratio. The fitted slopes as well as the calculated 0.9, 0.95 and 0.99 confidence levels are given by the grey lines. The linear regression is described by: $\text{sinking rate} = 2593 \times (\text{PIC/POC}) + 1986$ ($r^2 = 0.50$).

together with individual cell PIC/POC ratios, this sheds new light on the old question of the relationship between coccolithophore nutrient limitation and sinking rates.

8.5 Conclusion

In the present work we studied the shells of *E. huxleyi* coccoliths by using a combination of FIB sectioning and SEM imaging. We showed that the combination of a thin carbon film coating and drift correction by using a cross-marker in a post-processing step is a useful method to reduce charging effects and drift when imaging *E. huxleyi* coccospheres by means of FIB-SEM. By using this preparation and imaging technique we were able to get information about the inner assembly of *E. huxleyi* coccospheres. The culture (Strain RCC1238) studied here, was found to consist of 2–3 coccolith layers and an average number of 20 coccoliths per cell. The cell cavity for these coccospheres shows a constant diameter of about $4.36 \mu\text{m}$. It was demonstrated that FIB sectioning is a useful tool to elucidate coccosphere architecture, rendering accurate determination of cellular coccolith quota and estimates of single cell PIC/POC ratio, density and sinking rate possible.

8.6 Bibliography

- [1] CUREY, H., LOWENSTAM, H. A., EPSTEIN, S., AND MCKINNEY, C. R. Measurement of paleotemperatures and temperatures of the Upper Cretaceous of England, Denmark, and the Southeastern United States. *Geological Society of America Bulletin* **62**, 4 (1951), 399–416.

- [2] GIBBS, S. J., POULTON, A. J., BOWN, P. R., DANIELS, C. J., HOPKINS, J., YOUNG, J. R., JONES, H. L., THIEMANN, G. J., ODEA, S. A., AND NEWSAM, C. Species-specific growth response of coccolithophores to Palaeocene/Eocene environmental change. *Nature Geoscience* **6** (2013), 218–222.
- [3] GERHARD, F., AND WEFER, G., Eds. *Use of proxies in paleoceanography. Examples from the South Atlantic*. Springer-Verlag, Berlin, Heidelberg, 1999.
- [4] BOWN, P., AND PEARSON, P. Calcareous plankton evolution and the Paleocene/Eocene thermal maximum event: New evidence from Tanzania. *Marine Micropaleontology* **71** (2009), 60–70.
- [5] HAMILTON, E. L. Upper Cretaceous, Tertiary, and recent planktonic foraminifera from mid-Pacific flat-topped seamounts. *Journal of Paleontology* **27** (1953), 204–237.
- [6] YOUNG, J. R., DIDYMUS, J. M., BOWN, P. R., PRINS, B., AND MANN, S. Crystal assembly and phylogenetic evolution in heterococcoliths. *Nature* **356** (1992), 516–518.
- [7] YOUNG, J. R., DAVIS, S. A., BOWN, P. R., AND MANN, S. Coccolith ultrastructure and biomineralisation. *Journal of Structural Biology* **126**, 3 (1999), 195–215.
- [8] YOUNG, J. R., AND HENRIKSEN, K. Biomineralization within vesicles: The calcite of coccoliths. *Reviews in Mineralogy and Geochemistry* **54** (2003), 189–215.
- [9] STOLL, H. M., AND SCHRAG, D. P. Coccolith Sr/Ca as a new indicator of coccolithophorid calcification and growth rate. *Geochemistry, Geophysics, Geosystems* **1**, 5 (2000), 1–29.
- [10] YOUNG, J. R., AND ZIVERI, P. Calculation of coccolith volume and its use in calibration of carbonate flux estimates. *Deep Sea Research Part II* **47** (2000), 1679–1700.
- [11] LANGER, G., OETJEN, K., AND BRENNIS, T. On culture artefacts in coccolith morphology. *Helgoland Marine Research* **67** (2013), 359–369.
- [12] BALCH, W. M., HOLLIGAN, P. M., ACKLESON, S. G., AND VOSS, K. J. Biological and optical properties of mesoscale coccolithophore blooms in the Gulf of Maine. *Limnology and Oceanography* **36**, 4 (1991), 629–643.
- [13] HOLLIGAN, P. M., FERNÁNDEZ, E., AIKEN, J., BALCH, W. M., BOYD, P., BURKILL, P. H., FINCH, M., GROOM, S. B., MALIN, G., MULLER, K., PURDIE, D. A., ROBINSON, C., TREES, C. C., TURNER, S. M., AND VAN DERWAL, P. A biogeochemical study of the coccolithophore, *Emiliana huxleyi*, in the North Atlantic. *Global Biogeochemical Cycles* **7**, 4 (1993), 879–900.
- [14] BUITENHUIS, E., VAN BLEIJSWIJK, J., BAKKER, D., AND VELDHIJS, M. Trends in inorganic and organic carbon in a bloom of *Emiliana huxleyi* in the North Sea. *Marine Ecology Progress Series* **143** (1996), 271–282.

-
- [15] RIDGWELL, A., SCHMIDT, D. N., TURLEY, C., BROWNLEE, C., MALDONADO, M. T., TORTELL, P., AND YOUNG, J. R. From laboratory manipulations to Earth system models: scaling calcification impacts of ocean acidification. *Biogeosciences* **6**, 11 (2009), 2611–2623.
- [16] INKSON, B. J., MULVIHILL, M., AND MÖBUS, G. 3D determination of grain shape in a FeAl-based nanocomposite by 3D FIB tomography. *Scripta Materialia* **45** (2001), 753–758.
- [17] WILLIAMS, R. E. A., UCHIC, M., DIMIDUK, D., AND FRASER, H. L. Three-dimensional reconstruction of alpha laths in alpha/beta Titanium alloys by serial sectioning with a FEI NOVA. *Microscopy and Microanalysis* **11**, Suppl 2 (2005), 836–837.
- [18] UCHIC, M. D., GROEBER, M. A., DIMIDUK, D. M., AND SIMMONS, J. P. 3D microstructural characterization of nickel superalloys via serial-sectioning using a dual beam FIB-SEM. *Scripta Materialia* **55** (2006), 23–28.
- [19] HOLZAPFEL, C., SCHÄF, W., MARX, M., VEHOFF, H., AND MÜCKLICH, F. Interaction of cracks with precipitates and grain boundaries: Understanding crack growth mechanisms through focused ion beam tomography. *Scripta Materialia* **56** (2007), 697–700.
- [20] KATO, M., ITO, T., AOYAMA, Y., SAWA, K., KANEKO, T., KAWASE, N., AND JINNAI, H. Three-dimensional structural analysis of a block copolymer by Scanning Electron Microscopy combined with a Focused Ion Beam. *Journal of Polymer Science Part B: Polymer Physics* **45** (2007), 677–683.
- [21] DE WINTER, M. D. A., SCHNEIJDENBERG, C. T. W. M., LEBBINK, M. N., LICH, B., VERKLEIJ, A. J., DRURY, M. R., AND HUMBEL, B. M. Tomography of insulating biological and geological materials using focused ion beam (FIB) sectioning and low-kV BSE imaging. *Journal of Microscopy* **233** (2009), 372–83.
- [22] KUBIS, A. J., SHIFLET, G. J., DUNN, D. N., AND HULL, R. Focused ion-beam tomography. *Metallurgical and Materials Transactions A: Physical Metallurgy and Materials Science* **35**, A (2004), 1935–1943.
- [23] NALLA, R. K., PORTER, A. E., DARAIO, C., MINOR, A. M., RADMILOVIC, V., STACH, E. A., TOMSIA, A. P., AND RITCHIE, R. O. Ultrastructural examination of dentin using focused ion-beam cross-sectioning and transmission electron microscopy. *Micron* **36** (2005), 672–80.
- [24] GIANNUZZI, L. A., PHIFER, D., GIANNUZZI, N. J., AND CAPUANO, M. J. Two-dimensional and 3-dimensional analysis of bone/dental implant interfaces with the use of focused ion beam and electron microscopy. *Journal of Oral and Maxillofacial Surgery : Official Journal of the American Association of Oral and Maxillofacial Surgeons* **65** (2007), 737–47.

- [25] SCHMAHL, W. W., GRIESSHABER, E., MERKEL, C., KELM, K., DEUSCHLE, J., NEUSER, R. D., GÖTZ, A. J., SEHRBROCK, A., AND MADER, W. Hierarchical fibre composite structure and micromechanical properties of phosphatic and calcitic brachiopod shell biomaterials An overview. *Mineralogical Magazine* **72**, 2 (2008), 541–562.
- [26] KELM, K., GOETZ, A., SEHRBROCK, A., IRSEN, S., HOFFMANN, R., SCHMAHL, W. W., AND GRIESSHABER, E. Mosaic Structure in the Spines of *Holopneustes porosisimus*. *Zeitschrift für Kristallographie - Crystalline Materials* **227**, 11 (2012), 758–765.
- [27] LANGER, G., AND BODE, M. CO₂ mediation of adverse effects of seawater acidification in *Calcidiscus leptoporus*. *Geochemistry Geophysics Geosystems* **12**, 5 (2011), 1–8.
- [28] GUILLARD, R. R. L., AND RYTHER, J. H. Studies of marine planktonic diatoms, I, *Cyclotella nanna* (Hustedt) and *Detonula convervacea* (Cleve). *Canadian Journal of Microbiology* **8**, 2 (1962), 229–239.
- [29] LANGER, G., NEHRKE, G., PROBERT, I., LY, J., AND ZIVERI, P. Strain-specific responses of *Emiliania huxleyi* to changing seawater carbonate chemistry. *Biogeosciences* **6** (2009), 2637–2646.
- [30] MENDEN-DEUER, S., AND LESSARD, E. J. Carbon to volume relationships for dinoflagellates, diatoms, and other protist plankton. *Limnology and Oceanography* **45**, 3 (2000), 569–579.
- [31] WINTER, A., AND SIESSER, G. W., Eds. *Coccolithophores*. University Press, Cambridge, 1994.
- [32] GOODHEW, P. J., HUMPHREYS, J. F., AND BEANLAND, R. *Electron microscopy and analysis*, 3 ed. Taylor and Francis, London, New York, 2001.
- [33] YOUNG, R. J., DINGLE, T., ROBINSONS, K., AND PUGH, P. J. A. An application of scanned focused ion beam milling to studies on the internal morphology of small arthropods. *Journal of Microscopy* **172**, 1 (1993), 81–88.
- [34] PHANEUF, M. Applications of focused ion beam microscopy to materials science specimens. *Micron* **30** (1999), 277–288.
- [35] LESER, V., DROBNE, D., PIPAN, Z., MILANI, M., AND TATTI, F. Comparison of different preparation methods of biological samples for FIB milling and SEM investigation. *Journal of Microscopy* **233**, 2 (2009), 309–319.
- [36] GRANDFIELD, K., AND ENGQVIST, H. K. Focused ion beam in the study of biomaterials and biological matter. *Advances in Materials Science and Engineering* **2012** (2012), 1–6.

-
- [37] SROT, V., BUSSMANN, B., SALZBERGER, U., KOCH, C. T., AND VAN AKEN, P. A. Linking microstructure and nanochemistry in human dental tissues. *Microscopy and Microanalysis* **18** (2012), 509–523.
- [38] LANGER, G., GUSSONE, N., NEHRKE, G., RIEBESELL, U., EISENHAUER, A., KUHNERT, H., ROST, B., TRIMBORN, S., AND THOMS, S. Coccolith strontium to calcium ratios in *Emiliana huxleyi*: The dependence on seawater strontium and calcium concentrations. *Limnology and Oceanography* **51**, 1 (2006), 310–320.
- [39] PAASCHE, E. A review of the coccolithophorid *Emiliana huxleyi* (Prymnesiophyceae), with particular reference to growth, coccolith formation, and calcification-photosynthesis interactions. *Phycologia* **40** (2002), 503–529.
- [40] BENNER, I. *The utilization of organic nutrients in marine phytoplankton with emphasis on coccolithophores*, vol. 2. Dissertation, Universität Bremen, 2008.
- [41] LANGER, G., OETJEN, K., AND BRENNEIS, T. Calcification of *Calcidiscus leptoporus* under nitrogen and phosphorus limitation. *Journal of Experimental Marine Biology and Ecology* **413** (2012), 131–137.
- [42] LANGER, G., OETJEN, K., AND BRENNEIS, T. Coccolithophores do not increase particulate carbon production under nutrient limitation: A case study using *Emiliana huxleyi* (PML B92/11). *Journal of Experimental Marine Biology and Ecology* **443** (2013), 155–161.
- [43] BAUMANN, G. F., ISENBERG, H. D., AND GENNARO, J. J. The inverse relationship between nutrient nitrogen concentration and coccolith calcification in cultures of the coccolithophorid *Hymenomonas sp.* *Journal of Protozoology* **25**, 2 (1978), 253–256.
- [44] PAASCHE, E. Roles of nitrogen and phosphorus in coccolith formation in *Emiliana huxleyi* (Prymnesiophyceae). *European Journal of Phycology* **33** (1998), 33–42.
- [45] BACH, L. T., RIEBESELL, U., SETT, S., FEBIRI, S., RZEPKA, P., AND SCHULZ, K. G. An approach for particle sinking velocity measurements in the 3–400 μm size range and considerations on the effect of temperature on sinking rates. *Marine Biology* **159** (2012), 1853–1864.
- [46] BOYD, C., AND GRADMANN, D. Impact of osmolytes on buoyancy of marine phytoplankton. *Marine Biology* **141** (2002), 605–618.
- [47] HENRIKSEN, K., YOUNG, J. R., BOWN, P. R., AND STIPP, S. L. S. Coccolith biomineralisation studied with atomic force microscopy. *Palaeontology* **47**, 3 (2004), 725–743.

9 Influence of CO₂ on growth and crystallographic assembly of *Emiliana huxleyi* and *Calcidiscus leptoporus* coccospheres

9.1 Introduction

By the end of the next century, the expected atmospheric CO₂ level will be nearly 40% above the pre-industrial level, 250 years ago [1]. The global oceans can absorb a significant amount of the rising CO₂ level, but this will cause changes of the seawater chemistry [2]. These changes will have a direct influence on marine organisms that build CaCO₃ shells like corals, mollusks, echinoderms, foraminifera and particularly coccolithophorids [3]. Laboratory experiments have shown that many calcifying species reduce calcification and growth rates under high-CO₂ conditions [3].

To understand the adaptation potential of coccolithophorids to changing pH-values is interesting, since the biogenic carbonate precipitation is mainly (nearly 80 %) carried out by planktonic microorganisms [4] and particularly by these small marine algae [5]. The most common species *E. huxleyi* forms different morphotypes as a function of the habitat [6]. Temperature, salinity and the nutrient amount of the water body affects the morphology of this coccolith species [6]. Furthermore a study of de Bodt *et al.* showed that the pH value of the oceans has also an influence on the morphology of *E. huxleyi* coccoliths [7]. Culture samples of *E. huxleyi* were grown under different pH levels and temperatures. The coccoliths were divided into four different categories based on the shape of the crystals. It was shown that the number of well formed crystals of category one was reduced with rising pH values, while the temperature had no significant influence on the coccolith morphology [7]. Another study performed on cultured samples of *Coccolithus pelagicus* (*C. pelagicus*) and *C. leptoporus* revealed that the PIC of *C. leptoporus* changes with increasing CO₂ concentration in a nonlinear relationship, while the POC remains constant over the range of CO₂ concentrations investigated. The PIC/POC ratio shows an optimum curve [8]. In contrast neither PIC nor POC of *C. pelagicus* cultures changes significantly over the CO₂ range tested and the PIC/POC ratio was constant during the experiment [8]. Hence the two investigated species have shown different behavior during the experiment and therefore it is important to consider species-specific effects when evaluating whole ecosystem responses [8].

The aim of the present study is to correlate the morphological variations of *E. huxleyi* and *C. leptoporus* to defined environmental parameters. Therefore cultured *E. huxleyi* and *C. leptoporus* coccoliths were grown under different pH values. To gain information about shape and size of the coccoliths SEM imaging was applied. In future experiments TEM imaging will be used to investigate the diameter, size and thickness of coccolith segments on the nanoscale and EELS measurements will be performed to gain information of the chemical composition. For this measurements electron transparent samples are required. Thus, in this work suitable TEM preparation techniques were developed, which pave the way for the planned TEM studies.

9.2 Materials and methods

9.2.1 Samples

To study the influence of the seawater chemistry on the shells of different coccolithophorids two different species were used. Since it is possible to grow the most common species *E. huxleyi* and one of the biggest coccosphere species *C. leptoporus* in culture experiments these species were chosen. The cultures were grown in seawater with different CO₂ levels.

A first series containing an *E. huxleyi* strain was provided by Dr. Lothar Miersch (IFM-GEOMAR, Kiel). These clonal cultures of *E. huxleyi* (strain: #62) were grown in aged, sterile-filtered North Sea seawater enriched with 64 $\mu\text{mol kg}^{-1}$ nitrate, 4 $\mu\text{mol kg}^{-1}$ phosphate, trace metals and vitamins according to f/8 and 10 nmol kg^{-1} selenium. The temperature was 15 °C and the light concentration was 150 $\mu\text{mol photons m}^{-2}\text{s}^{-1}$. The samples were provided as triplicates in approximately 100 ml bottles. formaldehyde was used to avoid bacterial growth and to conserve the samples. This culture was grown under three different average CO₂ levels, 400, 1100 and 2200 microatm.

A second series provided by Dr. Gerald Langer (University of Cambridge, UK) contained clonal cultures of *C. leptoporus* from the Roscoff Culture Collection (www.sb-roscoff.fr/Phyto/RCC) (strain:RCC1130) grown in aged, sterile-filtered (0.2 μm pore-size cellulose-acetate filters) North Sea seawater. The water was enriched with 100 $\mu\text{mol kg}^{-1}$ nitrate, 14 $\mu\text{mol kg}^{-1}$ phosphate and trace metals and vitamins according to f/2 [9]. The temperature was 20 °C and the light concentration was 300 $\mu\text{mol photons m}^{-2}\text{s}^{-1}$. The samples were provided as triplicates in approximately 200 ml bottles. To avoid bacterial growth and to conserve the sample formaldehyde and heat treatment were applied. The five different average CO₂ levels used for this experiment are 200, 400, 800, 1200 and 1600 microatm.

Both sample series were filtered with a vacuum pump onto an Omnipore polycarbonate membrane filter (diameter: 47 mm, pore size: 0.45 μm), that was dried at room temperature. The material was then carefully removed with a spatula from the dried filter and dissolved in bi dH₂O for a specific amount of time depending on the species, the scientific question and the analysis method. Afterwards the samples were either dropped on a Si-Wafer or a TEM finder grid with a holey carbon film and then dried at room temperature. To avoid charging effects during the

SEM investigations the Si-Wafers were sputtered with a thin carbon film using a BAL-TEC coating system.

9.2.2 Instrumentation

For the SEM imaging four different microscopes were used, that are listed below:

- SEM (JSM-6500F) from JEOL, equipped with an energy dispersive x-ray spectroscopy (EDS) detector (*INCA ENERGY*) from Oxford Instruments,
- Field emission SEM (NVision40) from Zeiss,
- Field emission SEM (UltraPlus) from Zeiss equipped with an EDS detector (*INCA ENERGY*) from Oxford Instruments and
- SEM (Leo Modell 1450 VP) from Zeiss.

To avoid beam damage effects the SE images were taken at an acceleration voltage of 2.5 kV to 5 kV.

9.3 Results

In a first step the coccolithophore samples have to be conserved. One sample series of the *C. leptoporus* culture was conserved with formaldehyde and a second series was heated to a temperature of 40 °C. By using formaldehyde the coccospheres are still connected but calcium sulfate precipitates form. In contrast, the formation of calcium sulfate is hindered by heating, but the spheres break and only single coccoliths remain in the sample. Furthermore it could be observed that the bacterial growth is not stopped by heating the samples and the calcite is dissolved after some time. Hence for this study formaldehyde was used to conserve the sample and avoid bacterial growth.

To gain information about shape and size of the coccoliths grown under different pH-values SEM investigations were performed. The cultured series of *C. leptoporus* was taken and for each average CO₂ concentration twenty SEM images were acquired. In figure 9.1 a representative image for each CO₂ level is given. In figure 9.1a and in the zoomed-in area in figure 9.1b a well formed *C. leptoporus* coccolith is displayed. The crystal size is around 3 μm in length and 1 μm in width. It can be seen that the crystals start to deform at 400 microatm CO₂ (Fig. 9.1c and d). The single crystals grow bigger in width and thickness at a CO₂ concentration of 800 microatm. The length and shape is mostly the same like for lower CO₂ values (Fig. 9.1e and f). Like figure 9.1g and the zoomed-in area in figure 9.1h show, the crystal size increases at a CO₂ concentration of 1200 microatm. At the same time, the shape of the crystals started to change to a rectangular form. In this sample well formed coccoliths, that look like the coccoliths found at 200 microatm CO₂ concentration were additionally observed. This is shown in figure 9.2, were both coccolith types are displayed. Figure 9.2a and the zoomed-in area in 9.2b show the well

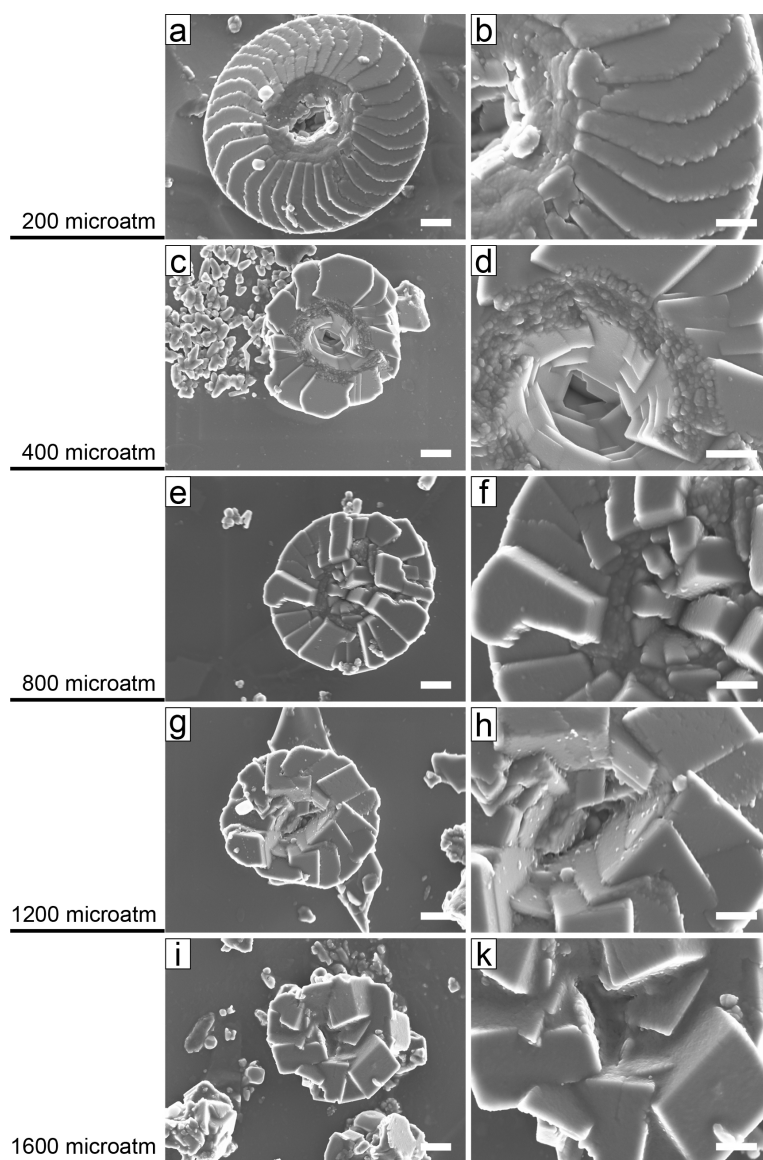


Figure 9.1 Representative SEM images of the *C. leptoporus* culture grown at five different CO₂ levels. The scale bar for each image is 1 μ m.

- a) SEM image revealing the morphology of a coccolith grown at 200 microatm CO₂.
- b) The coccolith given in a) imaged with a higher magnification to illustrate the crystal morphology.
- c) SEM image of a *C. leptoporus* coccolith grown at 400 microatm CO₂.
- d) Zoom-in of the same coccolith as in c).
- e) *C. leptoporus* coccolith grown at 800 microatm CO₂.
- f) To reveal the morphology of the deformed crystals of the coccolith given in e) a higher magnified image is displayed.
- g) SEM image showing a coccolith grown at a CO₂ level of 1200 microatm.
- h) Higher magnified image of the coccolith given in g).
- i) This image reveals the morphology of a coccolith grown at 1600 microatm CO₂.
- k) Higher magnified image of the coccolith shown in i).

formed coccolith, while in figure 9.2c and 9.2d the deformed coccolith is displayed. At an average CO_2 value of 1600 microatm even more crystals appear in an rectangular form (Fig. 9.1i and k). To summarize, we found that the length of the coccoliths remained nearly constant during the pH experiment while the width and thickness increased with a rising CO_2 concentration. The crystal shape also changed from a rectangular form to a quadratic form with an increase in the CO_2 concentration. Preliminary studies of *E. huxleyi* coccoliths revealed that the morphological variations as a function of the CO_2 value are less distinct for this species in comparison with *C. leptoporus* coccoliths (these images are not shown here). However, further investigations are necessary to confirm this observation.

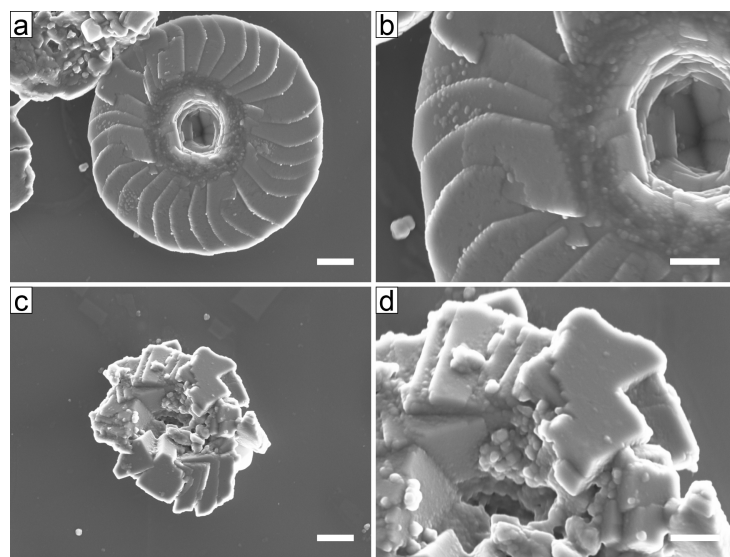


Figure 9.2 Two different morphologies of *C.leptoporus* coccoliths were observed at a CO_2 level of 1200 microatm. The scale bar for all images is $1 \mu\text{m}$.

- a) SEM image revealing the well formed morphology of a *C. leptoporus* coccolith at a CO_2 level of 1200 microatm.
- b) SEM image of the same coccolith as in a) taken with a higher magnification to illustrate the crystal morphology.
- c) SEM image of a deformed *C. leptoporus* coccolith grown at 1200 microatm CO_2 .
- d) To illustrate the crystal morphology of the coccolith given in c) a higher magnified image is displayed.

For TEM investigations thin samples are required. Since coccoliths have a maximum thickness of around 500 nm, the thickness has to be reduced. For the thinning procedure bi dH₂O was used. The coccolith samples were filtered with a vacuum pump onto a polycarbonate membrane filter and dried at room temperature. The remaining coccoliths were removed with a spatula and transferred into bi dH₂O. This solution was dropped on a TEM copper finder grid with a holey carbon film and dried afterwards at room temperature. The calcite shell of coccoliths is sensitive to bi dH₂O and when the thinning times are not well enough adjusted it can easily happen that the coccoliths dissolve completely. Therefore the thinning times have to be adapted for *E. huxleyi* and *C. leptoporus*. In a first experiment coccoliths of both species were kept for

5, 24, 31 and 50 hours in bi dH₂O and were dropped afterwards onto a Si-Wafer.

With the help of SEM imaging it turned out that for *C. leptoporus* the best thinning times are between 10 and 20 hours and for the more sensitive shell of *E. huxleyi* between one and five hours. A further experiment with thinning times between 10 and 20 hours in one hour steps revealed that the optimum thinning time is between 16 and 18 hours depending on the CO₂ level for *C. leptoporus*.

9.4 Discussion

In this study heat treatment as an alternative method for the sample conservation was tested. It was noticed that the heat treated coccospheres were disconnected, while the samples conserved with formaldehyde are still connected. Heating the samples up to 40 °C might have destroyed the organic material that surrounds the coccoliths and helps to build the coccosphere. The bacterial growth is not stopped at this low temperature and thus will affect the calcite of the coccoliths after a while. But this conservation method is adequate if coccoliths instead of coccospheres are required for e.g. nanodiffraction experiments and if the samples will be used immediately after the collection. Due to the findings, all other SEM experiments were done on samples which had been conserved by formaldehyde.

In this study SE images of 20 different *C. leptoporus* coccoliths for each CO₂ value were taken. It turned out that the morphology of the coccoliths changes significantly with an increase of the CO₂ level. However in the sample with a CO₂ value of 1200 microatm deformed as well as well formed coccoliths were found. That might be caused by the fact that the coccoliths of *C. leptoporus* can adapt to this CO₂ value and therefore, appear in the well formed shape. But it can not be excluded that this effect is caused by a change in sample composition. To exclude this, the samples should be prepared again and at least SE images of 50 different coccoliths should be taken.

The SEM investigation of the coccoliths of *C. leptoporus* showed that the crystal morphology changes significantly by changes of the CO₂ amount, while for the coccoliths of *E. huxleyi* the changes in the morphology were only small. This observation indicates that the coccoliths of *E. huxleyi* adapt much better to a rising CO₂ amount than the coccoliths of *C. leptoporus*. For a more quantitative understanding, further SEM investigations are necessary. It would be useful to take at least SE images of 50 different coccoliths for each CO₂ level. In addition, the crystal morphology at the nano scale should be investigated in the TEM, since it is possible that the changes caused by the CO₂ level occur at the internal structure of the crystals. For such TEM measurements the sample preparation parameters found in this work can be taken.

Different thinning times for *E. huxleyi* and *C. leptoporus* were tested to obtain electron transparent samples. Here we found an optimum thinning time of 3 hours for *E. huxleyi* and 16 to 18 hours for the much bigger coccoliths of *C. leptoporus*. These parameters were achieved by SEM studies, which revealed that in the case of *C. leptoporus* the crystals grow by an increase of the CO₂ level in microatm. Hence, for TEM sample preparation stepwise thinning times are

required. For the samples with the lowest CO₂ values (200 and 400 microatm) thinning for 16 hours was found to be adequate. The sample with an CO₂ level of 800 microatm was thinned for 17 hour and the samples that were grown at the highest CO₂ amount (1200 and 1600 microatm) and therefore possessed the thickest crystals were thinned for 18 hours. With these samples, TEM investigations can be performed to obtain information on the nanoscale concerning the crystallographic orientation and chemical composition.

9.5 Conclusion

In this study sample preparation methods for *E. huxleyi* and *C. leptoporus* coccoliths grown under different CO₂ conditions were developed. First of all an alternative for conservation with formaldehyde was searched. Heating the samples up to 40 °C was tested but it turned out that the individual coccoliths of the coccospheres separate. Thus, to determine the morphology of the coccolith crystals conserving the samples with formaldehyde is more appropriate. Since coccoliths have an initial thickness of around 500 nm at their thickest region and for TEM investigations a thickness of around 100 nm is required, they have to be thinned. For this, bi dH₂O was used and the thinning times for *E. huxleyi* and *C. leptoporus* were adjusted. For *E. huxleyi* a thinning time of three hours in bi dH₂O was found to be adequate. Since the coccoliths of *C. leptoporus* are larger and even grow thicker by an increase of the CO₂ level the thinning times had to be increased and range between 16 and 18 hours. This recipe can be used to prepare TEM samples for future experiments. Preliminary SEM investigations showed that the morphology of the crystals of the *C. leptoporus* coccoliths is changing strongly with the pH value, while the morphology of the *E. huxleyi* coccoliths seems to be mostly unaffected. This hints to the conclusion that the coccoliths of *E. huxleyi* can adopt better to an increase of the CO₂ value. Since in this present study the SEM investigations concentrated on the sample preparation, more detailed studies concerning the morphology are necessary, where besides SEM imaging TEM should be applied. By TEM investigations changes of the internal nanostructure can be detected which might be invisible in SEM.

9.6 Bibliography

- [1] SOLOMON, S., QIN, D., MANNING, M., CHEN, Z., MARQUIS, M., AVERYT, K. B., TIGNOR, M., AND MILLER, H. L., Eds. *Climate change 2007: The physical science basis: Contribution of working group I to the fourth assessment report of the intergovernmental panel on climate change*. Cambridge University Press, Cambridge, United Kingdom and New York, 2007.
- [2] SABINE, C. L., AND FEELY, R. A. The oceanic sink for carbon dioxide. In *Greenhouse Gas Sinks*, D. Reay, N. Hewitt, J. Grace, and K. Smith, Eds. CABI Publishing, Oxfordshire, UK, 2007, pp. 31–49.

- [3] DONEY, S. C., FABRY, V. J., FEELY, R. A., AND KLEYPAS, J. A. Ocean acidification: the other CO₂ problem. *Annual Review of Marine Science* **1** (2009), 169–192.
- [4] MILLIMAN, J. Production and accumulation of calcium carbonate in the ocean budget of a nonsteady state. *Global Biogeochemical Cycles* **7** (1993), 927–957.
- [5] WESTBROEK, P., YOUNG, J. R., AND LINSCHOOTEN, K. Coccolith production (biomineralization) in the marine alga *Emiliania huxleyi*. *Journal of Protozoology* **36**, 4 (1989), 368–373.
- [6] BOLLMANN, J., AND HERRLE, J. O. Morphological variation of *Emiliania huxleyi* and sea surface salinity. *Earth and Planetary Science Letters* **255** (2007), 273–288.
- [7] DE BODT, C., VAN OOSTENDE, N., HARLAY, J., SABBE, K., AND CHOU, L. Individual and interacting effects of pCO₂ and temperature on *Emiliania huxleyi* calcification: study of the calcite production, the coccolith morphology and the coccosphere size. *Biogeosciences* **7** (2010), 1401–1412.
- [8] LANGER, G., GUSSONE, N., NEHRKE, G., RIEBESELL, U., EISENHAUER, A., KUHNERT, H., ROST, B., TRIMBORN, S., AND THOMS, S. Coccolith strontium to calcium ratios in *Emiliania huxleyi*: The dependence on seawater strontium and calcium concentrations. *Limnology and Oceanography* **51**, 1 (2006), 310–320.
- [9] GUILLARD, R. R. L., AND RYTHER, J. H. Studies of marine planktonic diatoms, I, *Cyclotella nanna* (Hustedt) and *Detonula confervacea* (Cleve). *Canadian Journal of Microbiology* **8**, 2 (1962), 229–239.

10 Summary

This thesis had three different aims. The first aim was the precise and reliable determination of the hierarchical structure of coccoliths at the nanoscale using electron microscopy and electron diffraction techniques. The artifact free target preparation of the coccoliths and their elements is challenging and therefore the second aim was the development and optimization of preparation techniques for coccolith plan-view and cross-section TEM samples. In addition, optimal parameters for the TEM measurements needed to be found. The third aim was the determination of the influence of a rising CO₂ concentration on the morphology and crystal shape of the coccoliths. Furthermore, FIB sectioning was used to obtain information on the inner assembly of the coccolithosphere.

In order to understand calcite crystallization and assembly in a coccosphere with nanoscale resolution, the crystal orientation and interdigitation of the structural units was investigated by TEM imaging, selected-area and nano probe electron diffraction. For this purpose the abundant coccolithophore species *E. huxleyi* was chosen because it is the most common and best investigated species. FIB sectioning of coccoliths of this species was applied to obtain target-prepared specimens in suitable orientation. It was possible to detect and analyze the V-unit, which is overgrown by the R-unit in the case of *E. huxleyi*. The [001] direction of the V-unit points perpendicular to the coccolith plane while the [110] axis is tangential to the coccolith ring. The c-axis of the R-unit is parallel and the b-axis is perpendicular to the c-axis to the coccolith plane. These results verified the R- and V-model of Young *et al.* 1992, which was based on SEM and optical microscopy. Furthermore it was shown that the distal- and the proximal shield element of an individual R-unit of a single segment is tilted by $4^\circ \pm 1^\circ$ with respect to each other. This orientation change is required to obtain the flat domed character of the coccoliths. This in turn allows to form the sphere like coccosphere. The orientation change between the distal- and the proximal shield element seems to appear continuously. In a further study it would be interesting to investigate the structure of the R- and V-unit of further coccolith species like *C. leptoporus*.

For a detailed understanding of the crystal structure and chemical composition of coccoliths at the nanoscale, high resolution methods like TEM can be used, given that sufficiently thin samples can be prepared. In this thesis sample preparation techniques for cross-section and plan-view investigations for *E. huxleyi* coccoliths were developed. The results show that both preparation techniques, FIB sectioning for cross-section and dH₂O etching for plan-view studies, produce suitable TEM samples. Furthermore the sample stability under electron bombardment was tested. Coccoliths of *E. huxleyi* were chosen and in addition to the biological sample mineralogical samples (Iceland spar) were prepared for comparison. The HRTEM imaging, electron

diffraction and EELS studies revealed that all prepared samples are relatively stable under electron bombardment at an acceleration voltage of 300 kV when using a parallel illumination. Above an accumulated dose of $\sim 10^5$ e/nm² the material, independent of its origin, transformed to poly-crystalline calcium oxide.

Coccolithophores are able to fix dissolved inorganic carbon either through photosynthesis POC or through calcification PIC. The ratio of calcification to photosynthesis (PIC/POC ratio) is an important factor for modeling carbon cycling in the oceans and therefore is significant for climate change discussions. In a third study coccospheres of a cultured *E. huxleyi* clone were sampled in the exponential growth phase and sectioned using a FIB microscope with the purpose to gain detailed information on the internal structure that could be used for the PIC/POC ratio calculations. An average of 69 sections were taken. The corresponding SE micrographs per coccosphere provided detailed information on the coccosphere architecture. The latter features, 2-3 layers on average and 20 coccoliths per cell, of which only 15 can be seen in conventional SEM images. It was found that the outer coccosphere diameter is positively correlated with the number of coccolith layers. By contrast, the inner coccosphere diameter (around 4.36 μm), and hence the cell diameter was found to be quasi-constant. A further finding was that the coccoliths were not evenly distributed across the coccosphere, resulting in one part of the coccosphere displaying more coccolith layers than the other. The architectural data allowed to calculate, with sufficient accuracy, the PIC/POC ratio and the density of the individual cells.

Since the ultrastructure of biologically formed CO₂ crystals depends on environmental conditions such as pH value, temperature and salinity they can be used as indicator for climate changes. Therefore, it is important to investigate the ability of marine organisms to adapt to changing environmental parameters. In the last part of this thesis *E. huxleyi* and *C. leptoporus* grown under different CO₂ conditions were studied. The sample preparation parameters were adjusted for these species in a first step. It was found that for *E. huxleyi* a thinning time of three hours in bi dH₂O is adequate while for the thicker coccoliths of *C. leptoporus* the thinning times were between 16 and 18 hours depending on the CO₂ level. The morphology of the *E. huxleyi* coccoliths seems to be not affected by an increase of the CO₂ value while the morphology of the *C. leptoporus* coccoliths changes strongly with an increase of the CO₂ amount. This indicates that the coccoliths of *E. huxleyi* can adopt better to an increase of the CO₂ level compared to the ones of *C. leptoporus*. But these observations are only based on preliminary studies using SEM imaging. In future TEM investigations can be used to study changes of the nano structure.

11 Curriculum Vitae

Personal Information

First Name: Ramona
Last Name: Hoffmann
Nationality: German
Family status: children
Jonathan Adson Hoffmann (08.10.2007)
Charlotta Magdalena Hoffmann (20.03.2014)

University Education

05/2010 – until now PhD study: Earth and Environmental Sciences and Chemistry at the Ludwig Maximilians University Munich
10/2002 – 01/2009 Studies of Geosciences at the Eberhard Karls University Tübingen and at the Martin Luther University Halle/Wittenberg, graduation: Diploma
10/1998 – 09/2002 Studies of Socialwork and Socialpedagogics at the University of Applied Sciences Merseburg, graduation: Diploma (FH)

School Education

08/1996 – 07/1998 Professional School for health, personal hygiene and socialpedagogic in Halle/Saale, graduation: special qualification for university of applied sciences entrance (Fachhochschulreife)
08/1990 – 07/1996 Secondary school in Halle/Saale, graduation: certificate of secondary education
08/1986 – 07/1990 Primary school in Halle/Saale

Additional Skills

Technical skills

- Autonomous working at scanning electron microscopes (SEM) (Zeiss Leo Modell 1450 VP, FEI XL 40 ESEM, Zeiss field emission SEM ULTRA Plus)
- Autonomous working at a focused ion beam (FIB) microscope (ZeissNVision40)

- Autonomous working at transmission electron microscopes (TEM) (Jeol 2010, FEI Titan S/TEM 80-300 keV)
- Conventional TEM cross-section sample preparation and FIB lamellae preparation

Teaching skills

- Teaching SEM users at the FEI XL 40 ESEM
- Preparation of a new SEM course for master students including writing an user skript
- Supervision of master students during SEM course
- Scientific supervision of students (Bachelor thesis and research internships)
- Organization and realization of internships for school students (such as Girls day and Students information day)

EDV

- MS- Office user knowledge (Word, Excel, Power Point)
- Linux basic knowledge (Open Office, Destop publishing - LaTeX)
- Others: Digital Micrograph (good), ImageJ (good), ESVision (basic), Corel Draw (good)

Languages

- German (native language)
- English (good, written and spoken)
- Spanish (basic knowledge)
- French (basic knowledge)

Membership, funding and prizes

since 2011	Member of the German Society for Electron Microscopy (DGE)
2010 – 2012	PhD sholarship of the Bavarian Elite Funding Law (BayEFG)
2011	Travel funding of the DGE to participate at the MC 2011
2012	Travel funding of the DGE to participate at the EMC 2012
2012	Image Contest of the Royal Microscopical Society, 3th place
2013	Travel funding of the UK-IODP to participate at the TMS 2013

12 List of scientific contributions

12.1 Publications

Hoffmann R., Kirchlechner C., Langer G., Wochnik A. S., Griesshaber E., Schmahl W. W. and Scheu C. (2015) Insight in *Emiliana huxleyi* coccospheres by focused ion beam sectioning. *Biogeosciences*, **12**, 825-834.

Hoffmann R., Wochnik A. S., Heinzl C., Betzler S. B., Matich S., Griesshaber E., Schulz H., Kučera M., Young J. R., Scheu C. and Schmahl W. W. (2014) Nanoprobe crystallographic orientation studies of isolated shield elements of the coccolithophore species *Emiliana huxleyi*. *European Journal of Mineralogy*, **26** (4), 473-483.

Hoffmann R., Wochnik A. S., Betzler S. B., Matich S., Griesshaber E., Schmahl W. W. and Scheu C. (2014) TEM preparation methods and their influence on radiation damage on the beam sensitive CaCO₃ shell of *Emiliana huxleyi*. *Micron*, **62**, 28-36.

Wochnik A. S., Frank A., Heinzl C., Häusler J., Schneider J., Hoffmann R., Matich S. and Scheu C. (2013) Insight into the core-shell structures of Cu-In-S microspheres. *Solid State Sciences*, **26**, 23-30.

Kelm K., Goetz A., Sehrbrock A., Irsen S., Hoffmann R., Schmahl W. W. and Griesshaber E. (2012) Mosaic structure in the spines of *Holopneustes porosisimus*. *Zeitschrift für Kristallographie*, **277**, 758-765.

Edlmayr V., Harzer T. P., Hoffmann R., Kiener D., Scheu C. and Mitterer C. (2011) Effects of thermal annealing on the microstructure of sputtered Al₂O₃ coatings. *Journal of Vacuum Science and Technology A: Vacuum, Surfaces, and Films*, **29** (4), 041506-1-041506-8.

Numberger L., Hemleben C., Hoffmann R., Mackensen A., Schulz H., Wunderlich J.-M. and Kučera M. (2009) Habitats, abundance patterns and isotopic signals of morphotypes of the planktonic foraminifer *Globigerinoides ruber* (d'Orbigny) in the eastern Mediterranean Sea since the Marine Isotope Stage 12. *Marine Micropalaeontology*, **73** (1-2), 90-104.

12.2 Oral presentations

20.-23.01.2014 Mechanic meets Energy II Symposium Winterberg, Germany:

Hoffmann R.: TEM investigations on the crystal structure of *Emiliana huxleyi* coccoliths

16.-19.09.2013 DMG, GV and Sediment Meeting Tübingen, Germany:

Hoffmann R., Wochnik A., Heinzl C., Betzler S., Matich S., Griesshaber E., Scheu C. and Schmahl W. W.: TEM investigations of the assembly of the calcium carbonate crystals of *Emiliana huxleyi* coccoliths

27.-30.08.2013 Biomin12 Freiberg, Germany:

Hoffmann R., Wochnik A., Heinzl C., Betzler S., Matich S., Young J., Schulz H., Kučera M., Griesshaber E., Scheu C. and Schmahl W. W.: The single crystalline character of coccolith elements of the abundant species *Emiliana huxleyi*

2013 Mechanic meets Energy I Symposium Düsseldorf, Germany:

Hoffmann R., Wochnik A., Heinzl C., Betzler S., Matich S., Griesshaber E., Young J., Schulz H., Kučera M., Schmahl W. W. and Scheu C.: Electron microscopy studies of *Emiliana huxleyi* coccolith plates

24.10.2012 NET-Symposium Tübingen, Germany:

Hoffmann R., Wochnik A., Heinzl C., Betzler S., Müller A., Venkatesan S., Matich S., Griesshaber E., Young J., Schulz H., Kučera M., Scheu C. and Schmahl W. W.: Electron microscopy studies of *Emiliana huxleyi* coccolith plates

12.-15.03.2012 DGK-Tagung München, Germany:

Hoffmann R., Wochnik A., Betzler S., Müller A., Venkatesan S., Matich S., Griesshaber E., Young J., Schulz H., Kučera M., Scheu C. and Schmahl W. W.: Crystallographic assembly of the coccolith elements of *Emiliana huxleyi* - an electron diffraction study

09.-13.05.2011 EMRS-Spring Meeting Nice, France:

Hoffmann R., Griesshaber E., Young J., Müller A., Wochnik A., Scheu C., Matich S., Schulz H., Kučera M. and Schmahl W. W.: The crystallographic structure of *Emiliana huxleyi* - a TEM study

12.3 Poster presentations

18.-19.11.2013 TMS-Meeting London, UK:

Hoffmann R., Wochnik A., Heinzl C., Betzler S., Matich S., Young J., Schulz H., Kučera M., Griesshaber E., Scheu C. and Schmahl W. W.: Nanostructure investigations of *Emiliana huxleyi* coccolith elements done by transmission electron microscopy techniques

16.09.-21.09.2012 EMC Manchester, UK:

Hoffmann R., Wochnik A., Betzler S., Matich S., Griesshaber E., Schulz H., Kučera M., Young J., Scheu C. and Schmahl W. W.: Investigation of the R- and V-unit in the abundant coccolithophore species *Emiliana huxleyi* - an electron diffraction study

28.08.-02.09.2011 MC Kiel, Germany:

Hoffmann R., Wochnik A., Matich S., Müller A., Griesshaber E., Young J., Schulz H., Kučera M., Scheu C. and Schmahl W. W. TEM investigations of the beam sensitive CaCO₃ shell of *Emiliana huxleyi*

19.09.-25.09.2010 NIM and CeNS Summer school Venice, Italy:

Hoffmann R., Griesshaber E., Young J., Scheu C., Müller A., Wochnik A., Matich S. and Schmahl W. W.: TEM Studies on the crystallographic structure of *E. huxleyi* Coccolith plates

04.-05.06.2009 TMS Spring Meeting Zürich, Switzerland:

Hoffmann R., Schulz H., Waniek J. and Kučera M.: A sediment trap investigation of coccolithophore and calcareous dinoflagellates and other fine particle flux at 3000 m water depth under the Azores Front (33°N 22°W)

15.-17.05.2008 TMS Spring Meeting Tübingen, Germany:

Hoffmann R., Schulz H., Waniek J., Kučera M.: Coccolithophore and calcareous dinoflagellate species fluxes in the vicinity of the Azores Front (33°N 22°W) during 2003/2004: a sediment trap investigation

Danksagung

Ich möchte mich bei Prof. Wolfgang W. Schmahl für die Betreuung und Unterstützung während meiner Promotion und die Aufnahme in seine Arbeitsgruppe bedanken. Durch seine Unterstützung konnte ich viele wertvolle Anregungen für meine Arbeit und einen Einblick in die Kristallographie gewinnen. Vielen Dank für die erfolgreiche Zusammenarbeit. Mein Dank gilt auch Erika Griesshaber für ihre Hilfe und Unterstützung, wodurch ich neue Ideen in meiner Arbeit umsetzen konnte. Ein besonderer Dank gilt auch Frau Barbara Jaeger für ihre freundliche und hilfsbereite Art und die immer währende Unterstützung bei den Verwaltungsangelegenheiten und den organisatorischen Dingen. Bei Stefan Männl möchte ich mich für die Zeit und Geduld bedanken, die er für das dreidimensionale Modell der Coccolith Segmente aufgebracht hat. Für die freundliche Aufnahme in die Arbeitsgruppe gilt mein Dank Fitriana Nindiyasari, Andreas Götz und Markus Öhlerich. I wanna thank Fitriana Nindiyasari for a nice time during our measurements at the PSI and during the last years while sharing an office. Bei meinem Mittagessenstrupp David Dönnig und Patrick Alexa bedanke ich mich recht herzlich für die Unterstützung. Vielen Dank, dass ihr immer ein offenes Ohr für mich hattet und mir stets mit Rat und Tat zu Seite standet.

Mein ganz besonderer Dank gilt Prof. Christina Scheu für die Betreuung meiner Arbeit. Mit ihrer immer freundlichen, offenen, verständnisvollen und positiven Art stand sie mir stets zu Seite und hat maßgeblich zur Entstehung meiner Doktorarbeit beigetragen. Ich möchte ihr danken für ihre immer offene Tür durch die man stets mit Problemen aller Art schreiten konnte, um ein offenes Ohr und eine Lösung zu finden. Danke für die Chance einen Einblick in das interessante Gebiet der Elektronenmikroskopie zu bekommen und die liebevolle Aufnahme in die Arbeitsgruppe. Bei Markus Döblinger möchte ich mich für die Zeit, Ruhe und Geduld bedanken die er mir bei der Erlernung der Mikroskopbedienung entgegengebracht hat. Danke für die zahlreichen Tipps beim Arbeiten mit strahlsensitiven Materialien. Ein Dank geht auch an Steffen Schmidt für viele wertvolle Tipps bei der Probenpräparation und für das Arbeiten am REM. Des Weiteren möchte ich mich bei Regina Huber für ihre freundliche und offene Art und ihre Hilfe bei allen bürokratischen Angelegenheiten bedanken. Ein weiteres Dankeschön geht an Frau Siebel, die sich immer sehr freundlich und schnell um die Arbeitsverträge gekümmert hat. Ein weiterer Dank geht an Frau Alessandra Wührer für die Unterstützung bei den formellen Angelegenheiten der Zulassung und Prüfungsanmeldung.

Des Weiteren möchte ich mich bei meinen Kollegen Teresa Dennenwaldt, Angela Wochnik, Andreas Wisnet, Christoph Heinzl, Sophia Betzler, Stefan Gleich, Alena Folger, Anna Frank, Katharina Hengge, Marina Sysoltseva, Alexander Müller und Sriram Venkatesan aus dem Ar-

beitskreis Scheu bedanken. Danke für den tollen Zusammenhalt, die Unterstützung, die stets offenen Türen und die fantastische Arbeitsatmosphäre. Meiner Grafikdesignerin und Motivationshilfe Sophia Betzler gilt ein ganz besonderer Dank! Danke für zahlreiche Stunden am REM, für deine unschätzbare Hilfe bei der Auswertung der Daten, für das Korrektur lesen und für die schönen Bilder. Teresa Dennenwaldt danke ich für die tolle Bürogemeinschaft, für zahlreiche Male Korrektur lesen, für ein offenes Ohr bei Problemen und Unterstützung nicht nur bei wissenschaftlichen Fragen. Ein Dankeschön geht auch an Angela Wochnik. Danke für deine Ruhe und Geduld mit meinen Coccolithen und für deine Hilfe am TEM. Ich konnte viel von dir lernen. Daneben möchte ich dir und Teresa für eine tolle Zeit auf verschiedenen Konferenzen danken. Bei Christoph Heinzl möchte ich mich für die Zeit, die er für mich am TEM verbracht hat bedanken. Meinen Bürokollegen Andreas Wisnet und Alexander Müller danke ich für eine äußerst angenehme Arbeitsatmosphäre. Katharina Hengge möchte ich für eine schöne Zeit am FIB Mikroskop danken, schade, dass wir nicht öfter zusammen arbeiten konnten. Ich möchte mich bei Marina Sysoltseva für zahlreiche Stunden am REM und viele EDX Messungen bedanken.

Ich möchte mich auch bei meinen Praktikanten, Bachelor Studenten und wissenschaftlichen Hilfskräften Alexander Müller, Sophia Betzler, Johannes Munding, Nicole Treichel, Marina Sysoltseva, Ines Erhardt und Phillip Ratza bedanken. Johannes Munding danke ich für seine unerschütterliche Geduld und Zuversicht bei der Querschnittsprobenpräparation. Auch wenn sie nicht zum Erfolg führte, habe ich viel dabei gelernt. Bei Nicole Treichel möchte ich mich für die Hilfe bei der Präparation der Muscheln bedanken. Danke für dein ruhiges Händchen. Ines Erhardt gilt mein Dank für die Ausdauer beim suchen der richtigen Präparationstechnik der Proben aus den CO₂ Experimenten. Ein Dankeschön geht auch an Tristan Harzer für die tolle Zusammenarbeit mit den Al₂O₃ Proben.

Bei Sonja Matich möchte ich mich für das Einlernen in die Lamellen Präparation am FIB Mikroskop bedanken, du bist eine tolle Lehrerin! Danke für die Kreativität, Geduld und Zuversicht die du mit den Coccolith Lamellen gezeigt hast. Unsere erste Lamelle wird mir immer in guter Erinnerung bleiben. Gerald Langer möchte ich meinen herzlichen Dank für die fantastischen *C. leptoporus* Proben aussprechen. Gerne hätte ich weitere Untersuchungen an diesen schönen Proben vorgenommen. Des Weiteren möchte ich mich für die *E. huxleyi* Proben und die fantastische Zusammenarbeit an unserem Manuskript und die vielen wertvollen Tipps während unserer Telefonate bedanken. Deine Unterstützung hat maßgeblich zum Erfolg dieses Manuskripts beigetragen. Bei Hartmut Schulz möchte ich mich für die Nord Atlantik und die Proben aus dem Roten Meer sowie für die tolle Zusammenarbeit an unserem Paper bedanken. Ebenso möchte ich Michal Kučera herzlich für die unkomplizierte und hilfsbereite Mitarbeit an unserem Paper danken. Vielen Dank für schnelle und wertvolle Tipps. I also wanna thank Jeremy Young for his uncomplicated, helpful character and as well for the fruitful discussions and the help with our paper and manuscript. Ein Dankeschön geht auch an Lothar Miersch für die *E. huxleyi* Kulturproben aus dem CO₂ Experiment.

Bei Monika Dieckmann möchte ich mich für ihre Hilfsbereitschaft und Unterstützung bedanken. Danke, dass du mir so oft den Rücken freigehalten und Jonathan schöne unbeschwerte

Stunden beschert hast. Meinen Mädels Steffi Mund, Solvejg Trillhose, Katharina Obst und Petra Finkenbein danke ich für ihre Ermutigung, ihre Zuversicht und Aufmunterung. Mein Dank gilt auch Karl Heinz und Heidrun Ködderitzsch für ihre Hilfe und Zuversicht. Besonders möchte ich mich bei meinen Eltern Peter und Gabriele Hoffmann, sowie bei meinem Bruder Christian Hoffmann für ihre Unterstützung, ihre Ermutigungen und ihren Glauben an mich nicht nur während meiner Promotion sondern auch während meines Studiums bedanken. Ein besonders großes Dankeschön geht auch an Diemo Ködderitzsch und an meine Kinder Jonathan und Charlotta, ich weiß dass ihr es in letzter Zeit nicht leicht mit mir hattet und ich danke euch für eure Geduld und Zuversicht.